EFFECTS OF MICRO- AND NANO-SCALE SURFACE GEOMETRY ON BEHAVIORS OF LIVE
CELLS AND LIQUID DROPLETS

BY

MICHAEL GRIGOLA

THESIS

Submitted in partial fulfillment of the requirements
for the degree of Master of Science in Mechanical Engineering
in the Graduate College of the
University of Illinois at Urbana-Champaign, 2014

Urbana, Illinois

Adviser:

Professor K. Jimmy Hsia

Abstract

As the scale of the surface texture responsible for superhydrophobicity becomes similar to the size of a droplet, simple models based on homogeneity assumptions begin to break down. In order to better understand these discrete phenomena, we first create a unique model with the finite element software, Surface Evolver, which simulates a droplet atop the individual features that comprise a superhydrophobic surface. We observe that the well-known Cassie-Baxter and spherical cap models give poor estimates of characteristics such as contact angle and wet area and also fail to capture the complex liquid surface geometry when features have discrete size. Further exploring this theme, we consider the influence of gravity on these theoretical models using analytical and simulation results, and we find that the impact of gravity on droplet shape becomes non-negligible as surfaces become very hydrophobic. Motion is also significantly affected by discrete features, for example increased hydrophobicity may actually hinder droplet motility due to pinning. In light of this, we analyze data collected with a novel method of measuring forces in moving droplets to better understand the dynamics of pinning. The results and methodology developed here will help other researchers better understand the relevant mechanics in micro-scale droplets.

In a different setting, surface geometry also affects biological cells by altering their mechanical environment. In the case of cell mechanics we generally lack even a flawed model for describing the observed behavior, so we seek to identify parameters that might simplify these cellular systems. One method that allows us to investigate the effects of mechanics on cells is to expose the cells to uniform, periodic patterns. We first describe a unique procedure for generating approximately sinusoidal patterns at multiple length scales using thin-film buckling. These patterns are applied to study cells, first with muscle cells at the nano- to micro-scale where the patterns help identify a trend of muscle alignment as a function of surface characteristics. In the process we discover that cell-cell interaction also plays a role in the alignment. Next we investigate the effects of geometry on epithelial cells where the wavy patterns are used to ascertain the cause of unexpected ductal formations in a hydrogel culture. The cause is apparently mechanical and a result of variation in stiffness due to the underlying geometry. A final section also illustrates some of the techniques that were developed and used to investigate these phenomena, and which may be used by other researchers to further study these topics. These studies help better our understanding of mechanics at the micro- and nano-scale, while the methods used herein may be applied to a number of similar systems.

TABLE OF CONTENTS

1. Micro-scale Droplets

The classical Cassie-Baxter model has long held as a reasonable simplification for understanding superhydrophobicity on rough surfaces. In short, this model assigns an equivalent contact angle to a composite surface by taking the average of the contributions from each material of the composite weighted by the area fraction encompassed by the material [1]. In the case that the surface is rough and composed partially of air (void of solid features) we may take the air portion to have a 180° contact angle. Thus we can correctly predict that very high contact angles are possible when a surface is mostly composed of air and the area fraction (understood to be the fraction of surface area where the solid is in contact with the droplet) is low. When coupled with the assumption that a small droplet takes on a perfectly spherical shape, or a spherical cap when wetting a flat surface, we can fully describe the system by simply knowing the relative surface free energies of each material and the area fraction of the surface. For many applications, the Cassie-Baxter and spherical cap models are sufficient and accurate. This is particularly true when the roughness is homogeneous and much smaller in scale than the droplet. For the purposes here, we assume the droplet remains sessile, resting on top of the surface features and not descending and wetting the bulk of the features.

Recently, the Cassie-Baxter model has come under closer scrutiny, and its efficacy has been hotly debated by a number of groups [2–6]. A key point of contention lies in the assumption that the composite surface is homogenous and infinitesimal. Several simple experiments show that when these assumptions are broken, the resultant droplet shape can be vastly different than the models predict [3]. Additionally, the Cassie-Baxter model, in assigning a single equilibrium contact angle, fails to capture the observed existence of advancing and receding contact angles, which bound the contact angle observed to within a range, not a single value [7,8].

The present study of liquid droplets on superhydrophobic surfaces aims to better understand the cases when the Cassie-Baxter does not accurately describe wetting behavior. Specifically, we look at surfaces where the composite is not homogenous, and the size of the roughness features is finite. Additionally, we consider the correctness of the spherical cap model, which also has built in assumptions regarding the size of the droplet. The limitations of the spherical cap are identified in terms of droplet size as well as hydrophobicity of the surface. Lastly, a study related to contact angle hysteresis and pinning, another aspect unaccounted for by the Cassie-Baxter model is addressed by looking at the resistance to motion in moving droplets. Each topic addresses the shortcomings of the generally accepted but simple models.

Figure 1.1 shows a typical contact surface at the interface between a pattern of pillars and a liquid droplet. The key parameters describing the geometry and listed in the image: droplet volume, V, area fraction (the fraction of a unit cell on the pillar surface that is solid), ϕ, the spacing between pillars, L, and the pillar diameter, d. Additionally, the contact angle, Θ, can be defined as a single value relating the surface interface energies of the three phases present in a liquid droplet on a solid surface – the apparent or effective contact angle can be defined as the observed angle between droplet and a real surface, which will generally be different than the energetic contact angle. For the simulation work presented here the pillars are always square and evenly spaced in a square grid, so V, ϕ, γ, Θ, and either L or d uniquely define the system.
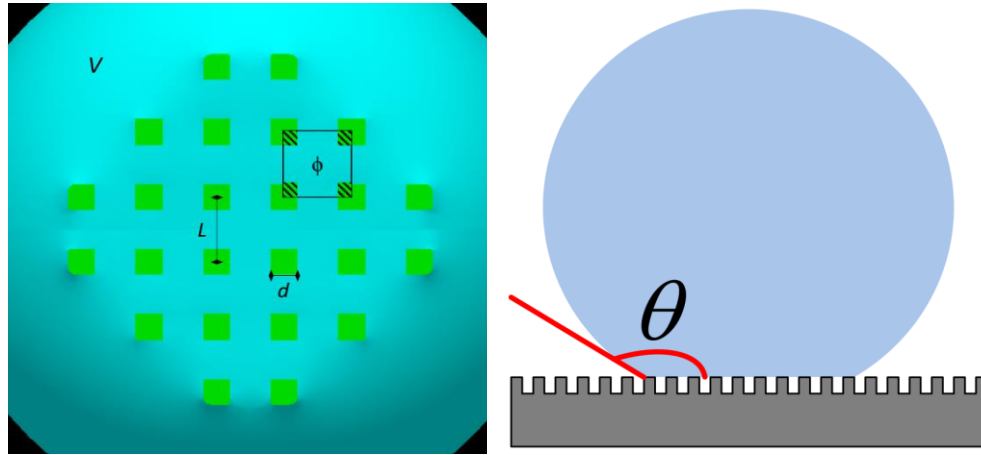

Figure 1.1: Droplet configuration and relevant parameters. V is the volume, ϕ is the area fraction of the surface, L is the pillar spacing, d is the pillar diameter, and Θ is the contact angle. The liquid-air surface energy will be designated γ.

1.1 Surface Evolver

Surface Evolver (SE) is a finite element software package for studying objects shaped primarily by surface tension. The program was written by Kenneth Brakke [9] and is freely available for general use. SE works by building a surface model with surface energy, body force energy, and user-defined energy functionals in arbitrary dimensional space and 'evolves' toward a lowest energy state via gradient descent. Surfaces are always defined as triangular patches with oriented edges and an outward normal, and bodies can be defined as the enclosure of multiple surfaces [10]. SE has been used in a number of scientific endeavors, notably including the determination of the shape of solder joints in electronics [11], the formation of soap bubbles [12], and, relevant to this work, the shape of liquid droplets.

The goal of the model presented here is to fully represent the 3D and discontinuous nature of a droplet resting atop discrete pillars. Developing such a model allows probing aspects of the droplet that are difficult or impossible to accomplish experimentally, such as the total energy, local curvature, local variation in the contact angle, and the effect of small changes to the shape or wetted pillars. The full model presented here is unique compared to a number of earlier models of droplets on pillars that either simplified the case to 2 dimensions [13] or modeled pillars as a single surface with continuously varying surface energy [14]. Similarly, several groups have modeled droplet evolution on a ridged pattern [15,16]. Each of these studies takes care to avoid discrete changes. Others have simplified the array of posts to study the dewetting of a single post in quasi-3D [17]; however only the space local to the pillar was considered, losing the complex interaction form neighboring pillars.

1.1.1 Model Development

While SE provides a powerful tool for simulating a model moving towards an ever-lower energy state, it does not provide tools to help design the model itself. The user must define the model using a text file listing the nodes (points in space), edges (directed connection between two nodes), facets (ordered collection of three edges), and constraints. This is often typed by hand, which is perhaps why most models are relatively simple. A common approach is to define the constraints and build a very basic surface, such as a cube, and then refine and evolve the model to until it more closely matches the desired geometry [10]. This same technique is applied here to some degree, although the numerous constraints and conditions preclude manually defining the model. Additionally, in order to investigate

effects of changing scale, the model must be easily changed by adjusting the parameters of interest –
this requires an automatically generated model.

The target model consists of a liquid droplet on an array of pillars where the droplet volume, pillar size,
pillar spacing, anisotropy ratio, and surface energy may all be adjusted. All results presented here are
for the PDMS-water-air interface where the liquid-gas surface energy is 0.072 J/m^2 and the
homogeneous contact angle is 114° as determined from experimental data. Gravity has been included
with a value 9.81m/s² except where otherwise indicated. The model simulates a droplet receding on
the pillars to determine its stable shape as discussed in detail below. It should be noted that the
resulting shape may not (and generally will not) be the absolute lowest energy configuration, but rather
the lowest local minimum in energy, i.e. the stable configuration reached such that total energy is
always decreasing during the simulation. This is similar to the case of droplet being roughly deposited
on the surface such that it reaches an equilibrium but does not continue receding to the 'optimal' shape
if the intermediate states present an energy barrier. We are interested in the final contact area as well
as the shape of the droplet, particularly close to the surface where it might be distorted from a spherical
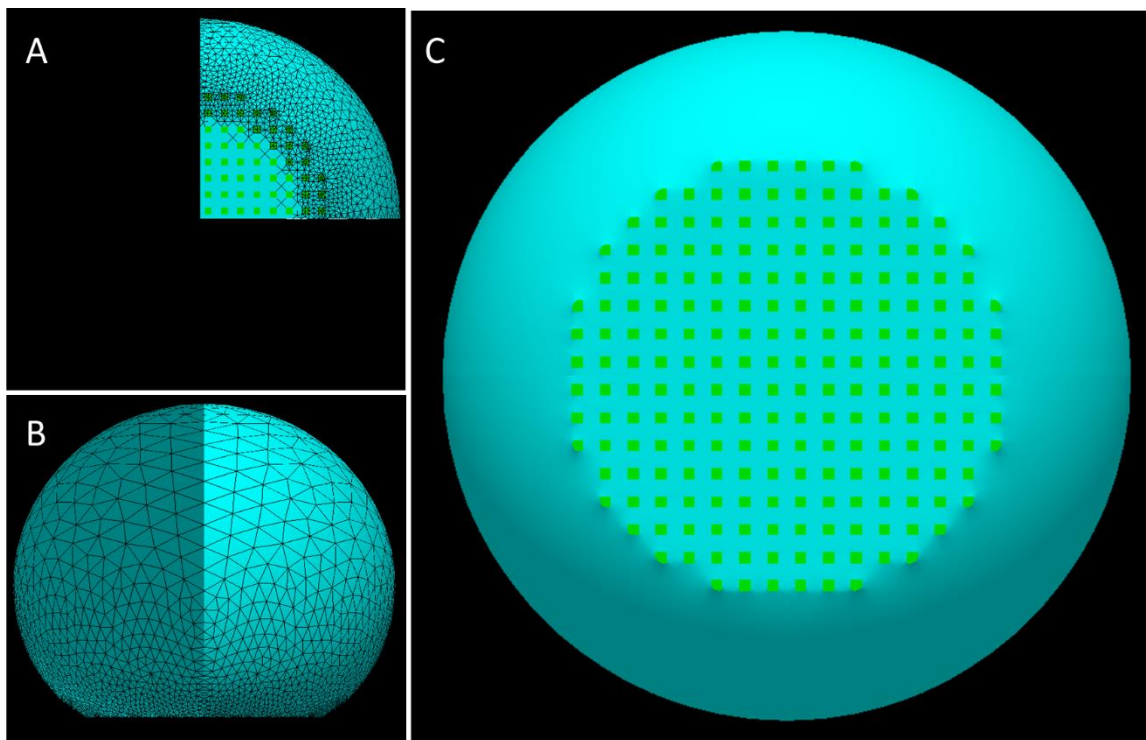cap.

Figure 1.2: Droplet model in SE. A) One quarter of the droplet is modeled. The mesh on the bottom of the
droplet eventually appears as in the image. B) Side view of the droplet and mesh. C) Rendered bottom view of
a droplet after reaching equilibrium.

The unique feature of this model is the discrete nature of the pillars. Each pillar is uniquely defined with individually named constraints. This allows an approximate modeling of pinning and individual dewetting events, which cannot be captured in a continuous model. To model the discrete pillars, two types of facts are defined: pillar facets and droplet facets. The droplet and pillars are defined as a single body where the pillar facets are incorporated into the bottom of the droplet but have different energy and constraints not applied to the droplet facets. The pillar facets are given an energy density equal to the liquid-surface interface energy while the free facets of the droplet are given the liquid-air interface energy. In practice, the pillar facet energy is implemented as a line integral applied to edges of all pillar facets as suggested by Ken Brakke [9]. Vertices of pillar facets are constrained such that their z-coordinate is 0, corresponding to the pillar surface. The x- and y- coordinates are constrained to lie within the boundary of the pillar – for square pillars this means 4 inequality (greater/less than) constraints are applied to all vertices on each pillar where the bounds are unique to each pillar. Droplet facets are unconstrained. The propagation of constraints during refinement is handled internally by SE.

Only one quarter of the droplet is modeled with symmetry conditions at the boundaries as seen in Figure 1.2A. For symmetry in a surface model, we need only apply an equality constraint to ensure boundary edges stay on the plane of the boundary. Choosing to model a fourth of the droplet rather than an eighth or half gives a balance between computational efficiency, difficulty of generating the model, and presence of asymmetric shapes. The quarter is mirrored about the center axis to produce the images of the full droplets in Figure 1.2B,C. Figure 1.2A also reveals the bare area near the center of the droplet which is not meshed. These unmeshed facets are not included in the energy functional for gradient descent (for computational efficiency because they do not change), although they still contribute a constant value when reporting the total energy of the system. The appropriate size of the bare area is estimated during model generation by a complex empirical function of all the system parameters. In general, at least one row of pillars is meshed between the bare area and the pillars on the contact line to ensure the simulation is not affected by leaving out the innermost pillars.

1.1.2 Dewetting

The model starts in a non-equilibrium state larger than the expected final size, including more wetted pillars than equilibrium as estimated by an empirical formula during model generation. During the course of simulation the contact line recedes, and facets on pillars that are energetically unfavorable to remain wet will reduce in area. To account for the discrete dewetting, the simulation periodically checks all pillars to see if they are nearly unwet, and if so, the pillar is irreversibly and fully set to become unwet. When this happens, all constraints imposed by the pillar are removed, the line integral is removed, the surface energy is changed to the liquid-gas surface energy, and the color of the facet is changed from green to blue to visually indicate the pillar has been unwet. Vertex averaging, removal of tiny edges ("t"), and equiangulation ("u") are performed after a pillar has been unwet to limit instabilities from a sudden change in constraints.
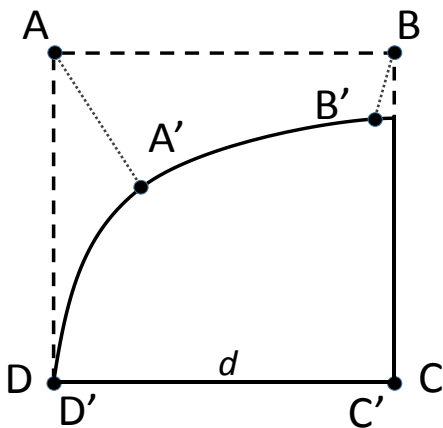

Figure 1.3: Method of determining dewetting. If ABCD are the corners of the wet pillar before simulation and A'B'C'D' are the same vertices some time later in the simulation, the pillar is considered unwet if any of the distances AA', BB', CC', or DD' is greater than a threshold defined as a multiplying factor (usually 0.75) times d, the diameter or side length of the pillar. I.e., if the maximum displacement of any vertex from its undeformed position is greater than .75d, the pillar is removed.

The method of determining if a pillar has been sufficiently unwet is to check if any corner of the pillar is displaced greater than a threshold distance from its original position, with the threshold defined as 0.75d. See Figure 1.3. This is admittedly imperfect but computationally efficient and easily applied to all pillars by measuring the displacement of the vertices that started at the corners. Results seem to match the intuitive sense of when a pillar should dewet – the outermost pillars are extremely unfavorable and condense to a point within a couple iterations before they are checked and freed. However, as the contact line approaches an equilibrium state, the determination of when a droplet should dewet becomes more ambiguous. Also, for a large droplet the energy contribution from small changes in wetted facets is nearly negligible compared to the rearrangement of larger facets higher up near the top

of the droplet. The exact dynamics of the dewetting process for a receding droplet need to be further studied to determine a more precise dewetting metric. Still, it is worth noting that while a multiplying factor of 0.75 was typically chosen, there seems to be a range of reasonable factors that yield the same contact area, and even larger changes in the threshold only lead to small changes in the contact area. This was not systematically tested.

1.1.3 Meshing and Convergence

Surface evolver is different from many finite element packages in that the mesh changes at every step. Convergence and the accuracy of the final solution can be difficult to determine. In this particular case, there is added difficulty due to the multiple length scales; the detail near the contact line is much finer than the detail near the top of the droplet and must be accounted for by maintaining a graded mesh as the shape of the droplet changes and contact line recedes. In practice, this is accounted for by starting with a coarse mesh and selectively refining facets combined with vertex averaging. In SE, any individual facet may be refined by issuing the "r" ("refine") command, which divides each of the facet's edges in half and creates 4 facets from the original. Vertex averaging, "V", redistributes all vertices so they are at the weighted centroid of their adjacent facets, making vertices more evenly spaced.

Facets are labeled during model generation in groups based on increasing distance from the origin so they can be selectively refined during the simulation – pillars just above the liquid-solid interface are refined first, and as more pillars dewet, the new facets closest to the interface are refined. This is simply done after a fixed number of simulation iterations empirically determined by the rate the droplet dewets/converges. The wetted facets are kept smaller (more refined) because they contain the most intricate detail in the model, so additional refinement is produced as the pillar facets are freed from their constraints and added to the main droplet surface. Vertex averaging is performed intermittently, which helps 'spread' the refinement near the surface towards the top of the droplet. These procedures result in a smooth gradient of refinement from the top of the droplet to the pillar-liquid interface.

The simulation process is not automated by surface evolver, so the sequence of simulation steps is inputted by the user, including iteration, refinement, vertex averaging, step size selection, and removal of unstable edges. During the model generation process, define the simulation sequence. This is a single, automated sequence of simulation steps, refinements, and selection of step sizes appropriate for

the level of refinement. The sequence first converges to the equilibrium shape, then if desired for information about shape or curvature, the model is globally refined and evolved to capture fine details. Automating the process as a single execution keeps the refinement process impartial and repeatable, which is necessary for parametric study. Some key time points in a typical simulation sequence are given in Figure 1.4. The entire simulation is also readily captured as a movie.
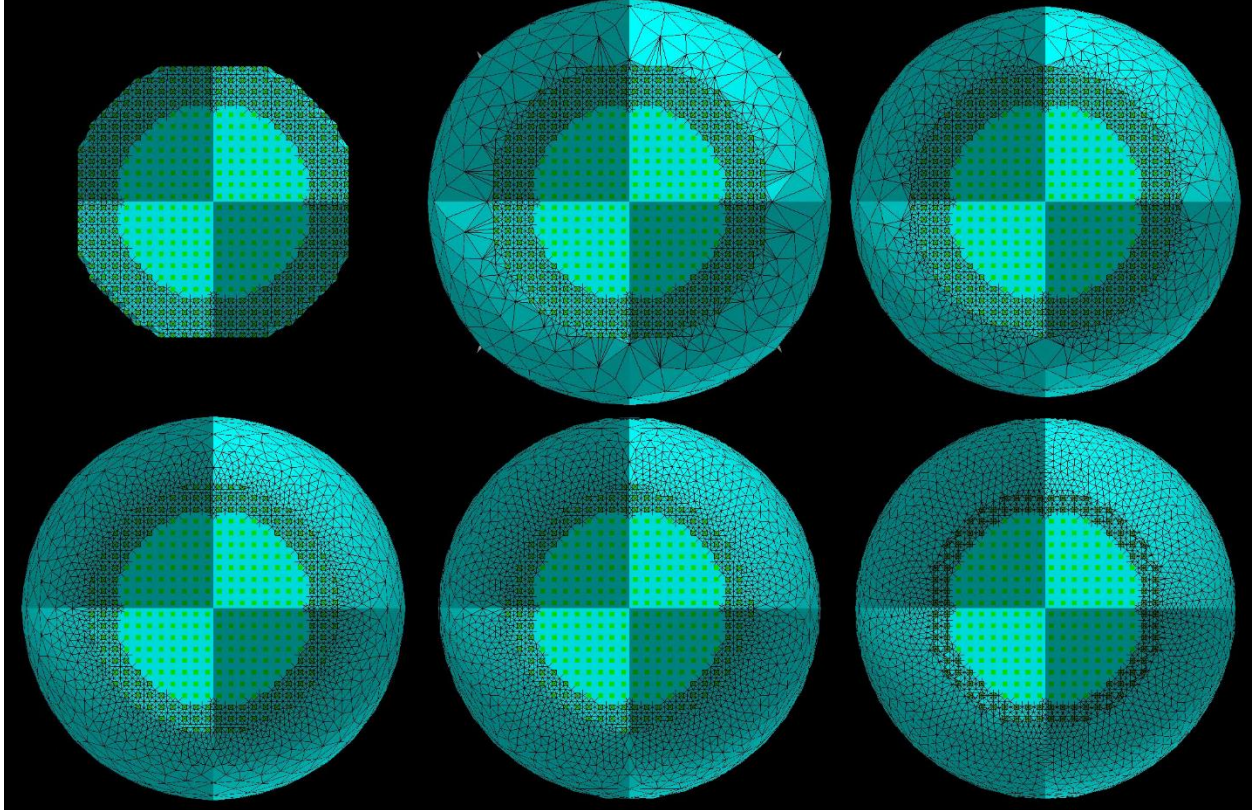

Figure 1.4: Key frames from a recording of a simulated droplet (7 µL, $\phi = 0.25$) evolving toward a minimum energy state. Several rows of the initial pillars dewet, and the mesh becomes progressively finer.

1.1.4 Contact Area

Numerous simulations were run for droplets in the ranges of V = 1-20µL, ϕ = 0.09-0.64, and L= 50-200µm.   Results were manually analyzed for contact area defined as the bounding polygon connecting the outmost edges of wet pillars via straight lines. One question that arose from looking at experimental drops regards the seemingly un-round, polygonal nature of the contact line for small droplets, and if this was indeed a minimum energy state. Given the finite number of ways a droplet can wet a surface given a certain volume, the droplet may be biased to hold an octagonal contact area rather than a smoother shape with higher edge count due to differing line energies of bridges between

8

wet pillars. Combining data from all the simulations yielded some 42 different contact line patterns that were observed for increasing droplet size. The result is displayed as one image in Figure 1.5, where each unique difference between successively larger droplets is given a separate color. The results seem to refute the idea that a more octagonal contact area is preferred, although it is possible the cause of the effect in experimental results is not captured by the SE model. Liquid imbibing a patterned surface is known to form such defined geometries [18,19].
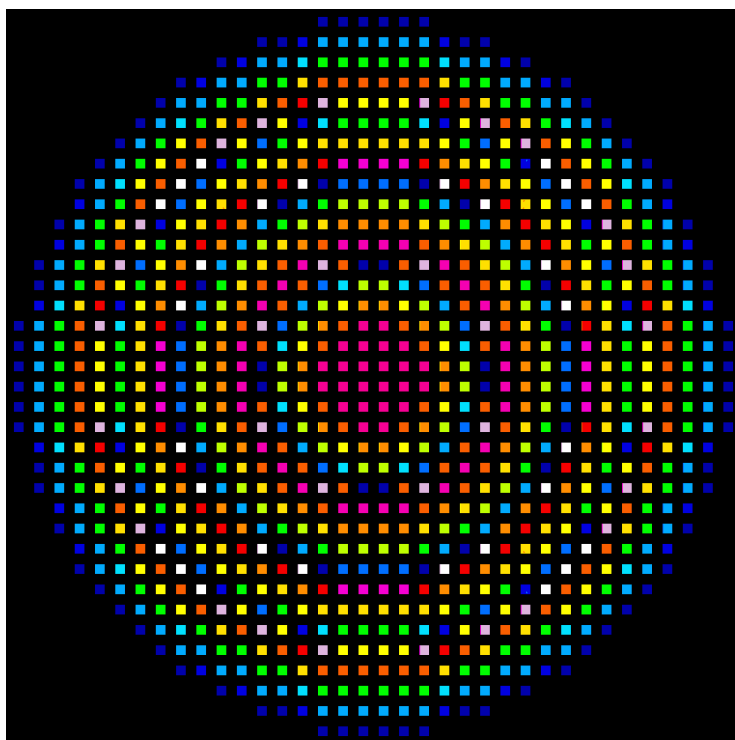

Figure 1.5: The different equilibrium configurations of the contact line compressed into one image. Each different color represents a unique shape of the contact line achieved as a result of running the simulation to completetion for increasing droplet volumes. For a given number of wet pillars, the equilibrium wetted pattern tends to be the same across different droplet volumes and pillar spacings.

1.1.5 Droplet Shape

More difficult to assess experimentally is the nuanced, 3D shape of the droplet near the contact surface. Goniometer measurements may allow measurement of an effective contact angle at multiple orientations, but they cannot give a precise shape or account for concavity if present. One experimental solution to getting precise 3D data on the droplet shape is to use SEM; however, this will generally not work for liquid as it will evaporate under vacuum. Some researchers have used curable polymers, such as PDMS, to freeze the droplet in place and view it [20]. The alternative is to directly simulate and view the full mesh with information on curvature and contact angle.

A simple method to extract information about the surface shape is to take section cuts along the longitude and latitude of the droplet. The built-in rendering engine from SE is used to smooth the sharp-edged facets and then cross-sections of the droplet surface (contours) are captured at fixed locations. The result is Figure 1.6. These images are taken from a 7μL droplet with ϕ = 0.25 and L = 100μm. In Figure 1.6, longitudinal slices are taken at 5° increments comprising the 10 unique angles at this spacing. The section view is near the interface with the surface, showing the very different contact angles observed at different locations. The cut through the nearest pillar to the edge is drawn in gray, which reveals that the local position of the pillar relative to the free surface has a significant impact. We can try to quantify these curves with a simple angle by looking for a limit of where the bulk shape should intersect the surface (similar to a goniometer reading) as plotted in Figure 1.7 for several different droplet sizes, but there is significantly more variation than is captured by the single number, which itself might vary over 5° for a given droplet.

Figure 1.6: Longitudinal slices through a droplet. For reference, the droplet is 7μL and approximately 2mm tall. A) The location of the slices at 5 degree increments, colorcoded to match the right. B) The slices. The grayed area is the cut through the outermost wet pillar.
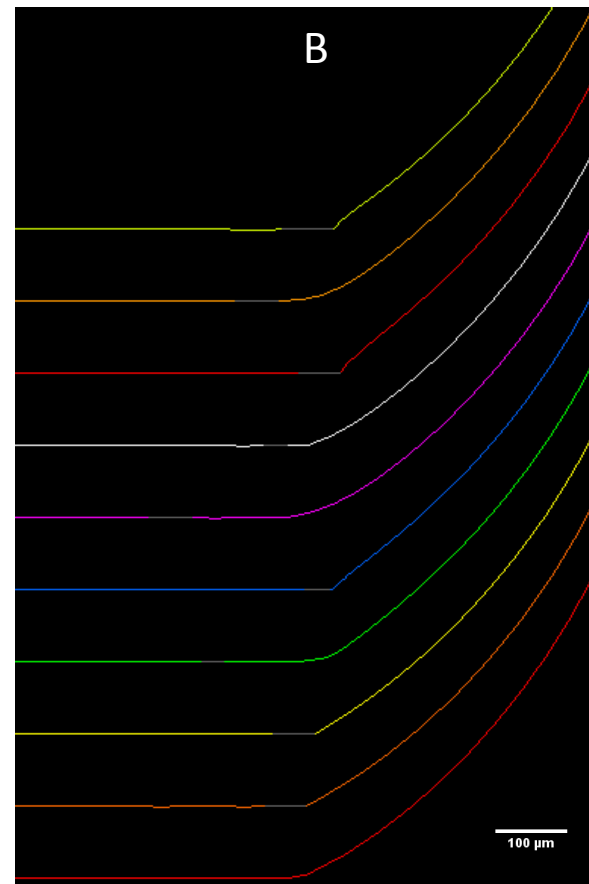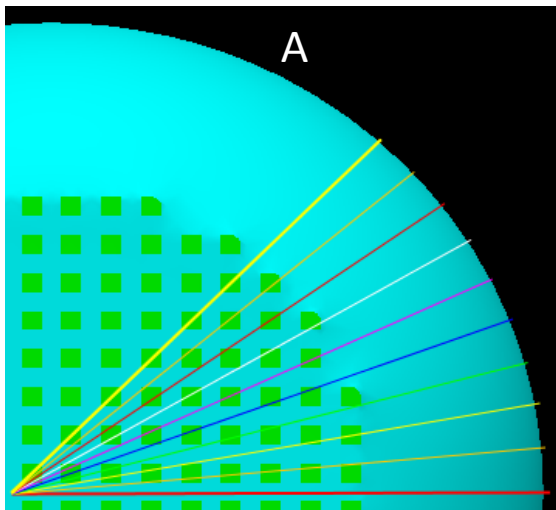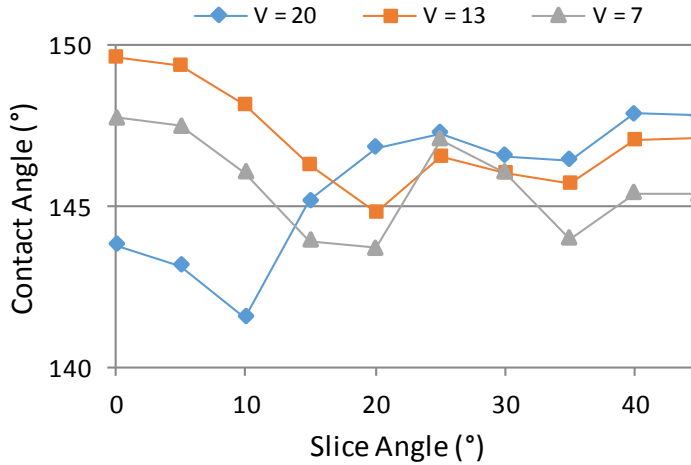
Figure 1.7: Plot of observed contact angle at 5° increments around the droplet. for different droplet volumes.

An in depth understanding of the behavior near the surface can be gained by looking at the curvature. The simple section cuts at increments of 10μm above the surface in Figure 1.8A show that there is significant distortion occurring near the liquid-surface interface, particularly near the pillars. Figure 1.8B gives a slightly finer view of a similar height map, emphasizing the surface height in the first 20μm above the pillars. Even more telling are the minimum and maximum principal curvatures in the same region as seen in Figure 1.9. These plots show that the apparently least stable regions are near the 'corner' pillars where curvature magnitude is large. The minimum curvature plot shows there is a large area of negative curvature (concavity) near the corner pillars. These minutia are very difficult to capture experimentally and perhaps represent the greatest value of the SE model.

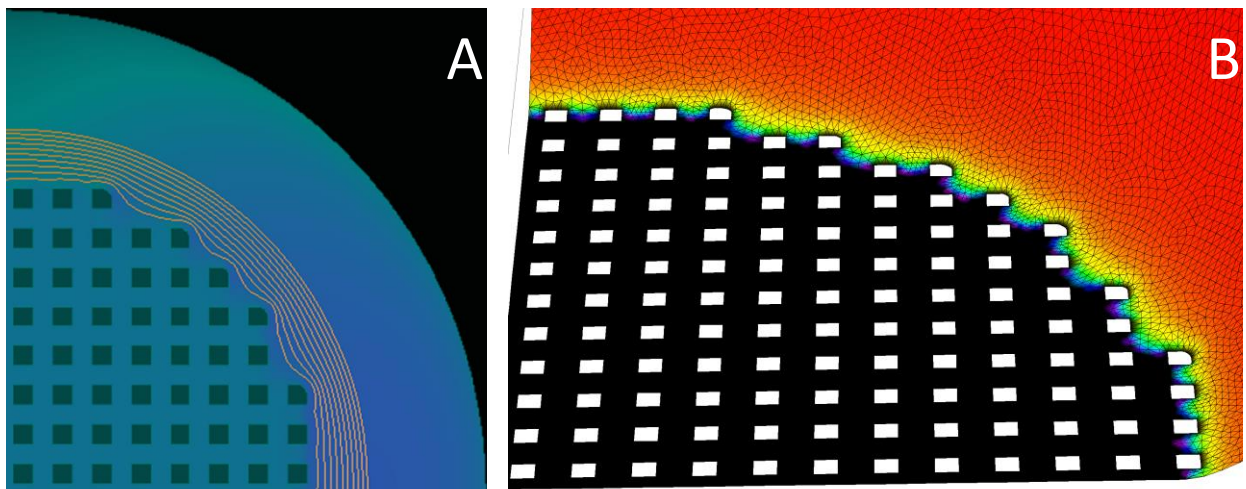Figure 1.8: Height maps of the droplet profile near the solid interface. A) Contours at 10μm increments starting at 10μm (7μL drop). B) Color is related to the height showing finer detail. Overlaid on the actual mesh.
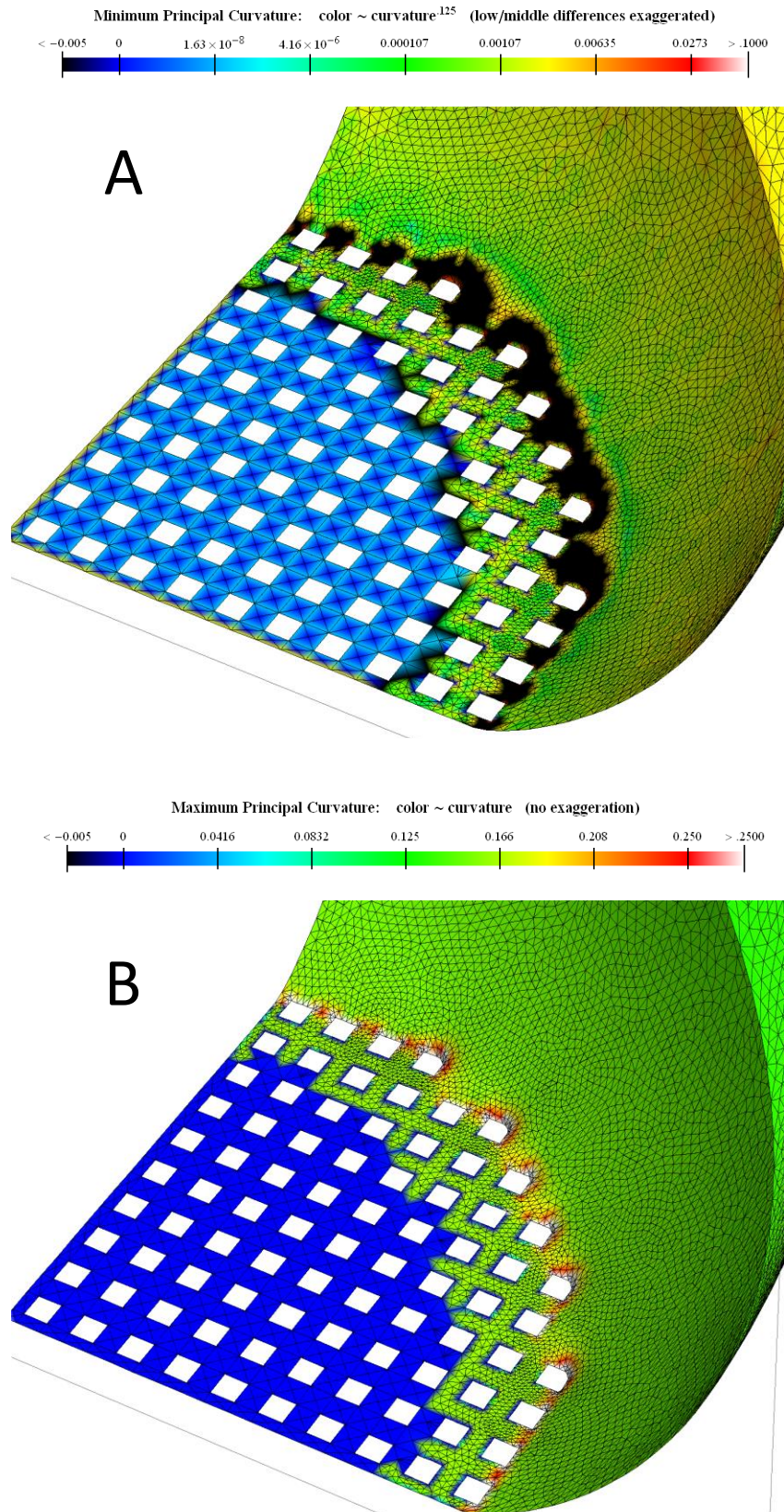
Figure 1.9: Plot of the refined mesh with color indicating the local curvature. A) Minimum curvature, black is negative (concave). B) Maximum curvature, largest near the 'corners' of the contact line.

1.2 Gravity

The capillary length defines a characteristic length scale for an interface between fluids subject to gravity.

$$Capillary\ Length = \sqrt{\frac{\gamma}{\rho g}}$$

Many researchers are quick to assert that the droplets in question are smaller than the capillary length in the typical case of ~10µL droplets, and thus gravity may be neglected and a spherical cap droplet shape can be assumed. Implicitly it is done whenever a spherical cap assumption is invoked. This is indeed generally accurate as the droplet radius for a spherical 10µL volume in air is 1.3mm, which is less than the capillary length, which is 2.7mm for water in air. In fact, the contact angle of a sessile drop is known to be invariant to the gravitational field, as one might expect. This gives further reason to ignore the effect of gravity when defining theoretical model in order to simplify a model.

However a more rigorous assessment is in order because the capillary length is at least on the same order of magnitude as the droplet size. We also wish to quantify the impact of gravity and acceleration in general so we may determine if is truly negligible and at what point it ceases to be negligible. While such things have been extensively studied before, for example finding the shape of a pendant drop, the topic has not been addressed in the context of superhydrophobic droplets and how gravity might affect modeling these systems. With the introduction of equations dependent on the contact area of a droplet, which might be exceedingly small for superhydrophobic surfaces, we must be sure we are not introducing unnecessary error into our models. This study seeks to quantify the impact of gravity on superhydrophobic droplets

1.2.1 Energy and Non-dimensional Value

As a first approach to the problem, consider a homogeneous solid surface and a spherical cap droplet. We may directly calculate the total potential energy of the body and to keep things simple, ignore the solid-liquid interaction. The ratio between the two components of energy as a function of droplet volume is:

$$\frac{E_{Gravity}}{E_{Surface}} = \frac{\rho g}{3\gamma} \left(\frac{3V}{4\pi}\right)^{2/3}$$

This demonstrates how the ratio varies with volume, but the assumed configuration is essentially a droplet floating above the surface with a 180° contact angle. A more complex ratio would include a finite contact angle and account for the actual center of mass of the droplet and the contribution from the liquid-solid interaction. Interestingly, this can be done by completely factoring the liquid-solid interface energy and the height of the mass center as functions purely of the contact angle. The terms can be lumped together as a pre-factor to the above equation to separate the contributions:

$$f(\theta) = \frac{(3+\cos\theta)(\sin\frac{\theta}{2})^{1/3}}{2\,(2+\cos\theta)^{5/3}}$$

Where Θ is the effective contact angle, independent of any assumption as to how the contact angle is achieved. Thus the complete ratio consists of a portion related to the volume multiplied by the portion related to the contact angle. The pre-factor is plotted over the range of hydrophobic contact angles in Figure 1.10A, and the volume is also included in the 3D plot in figure 1.10B. The key feature of this curve is that it is monotonic and increases with the contact angle, thus we may conclude that the effect of gravity on the energy of the system becomes more important for highly hydrophobic surfaces.
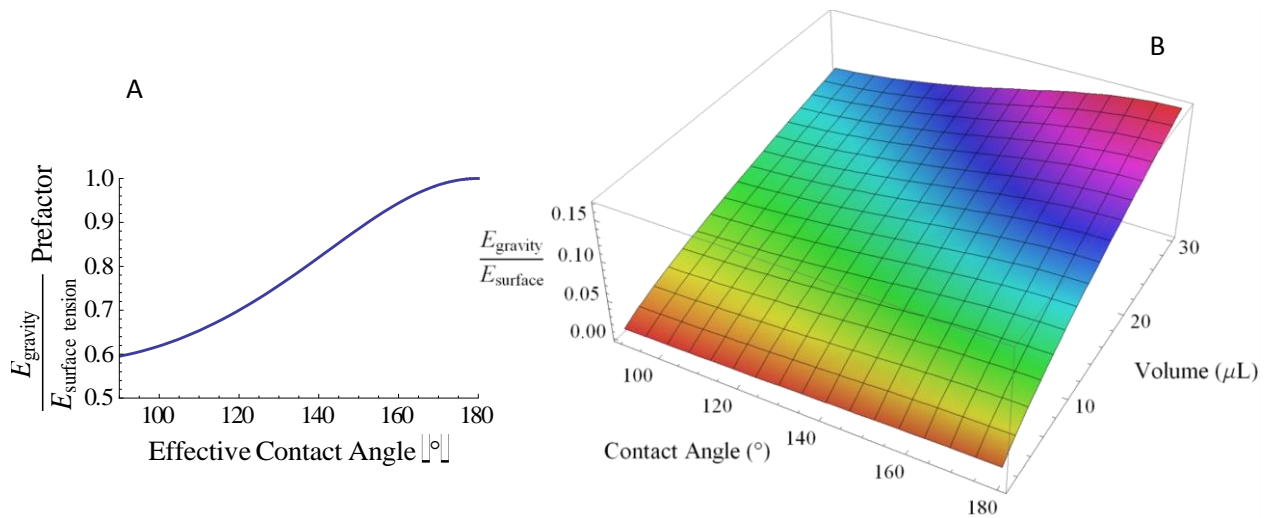

Figure 1.10: Comparison of gravitational and surface energy potential. A) Pre-factor contribution from the contact angle alone. B) Accounting for volume and contact angle.

1.2.2 Numerical Solution

The differential equation governing the shape of a liquid droplet due to surface tension is well known as the Laplace-Young equation. Numerical solutions to this equation in the case of a liquid droplet on a solid surface have been available for over a century. There are several ways to approach this problem using different forms of the Laplace-Young equation and different starting conditions. In this case where contact angle and volume are known, the simplest method to numerically solve for the shape of the droplet is borrowed from [21], where the relevant differential equation takes the form:

$$\frac{r''}{(1+r'^2)^{3/2}} + \frac{1}{r(1+r'^2)^{1/2}} = \frac{-\rho g z}{\gamma}$$

Where r, the radius, is solved for as a function of z, the height above the solid surface. The mass density and surface tension are ρ and γ, respectively. This form is simple as there are no discontinuities in the solution, and we can mirror the result around $r = 0$.

Figure 1.11: Numerical solution to Laplace-Young equation with gravity.
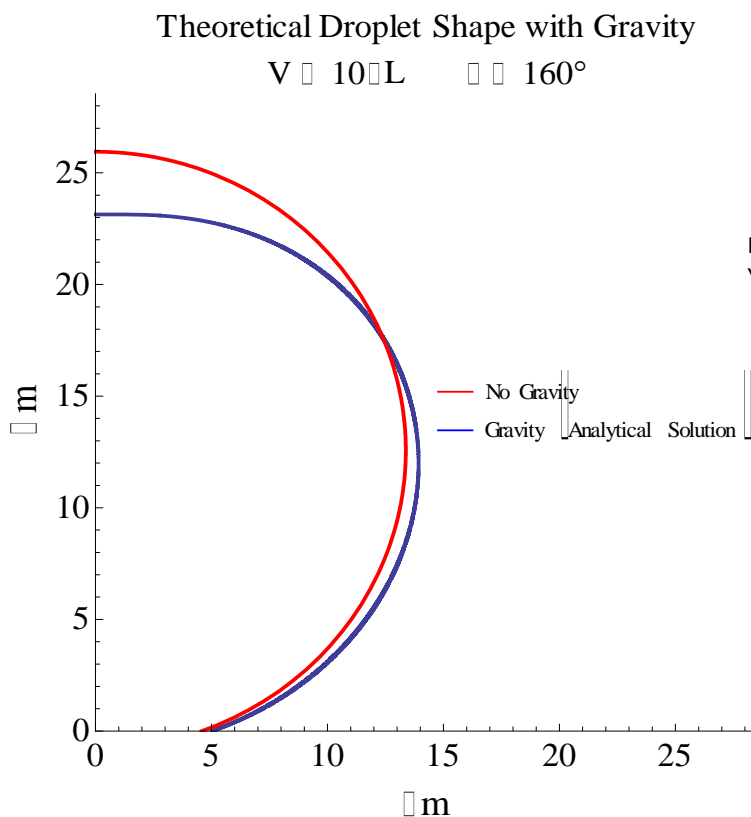
The ODE is solved using a shooting method where the contact angle is prescribed and the contact radius is guessed. The system is then solved, yielding a volume, which is compared to the target volume. If the actual volume is within a tolerance (.001%) of the target volume, the solution is found, otherwise the initial guess of the radius is improved and procedure repeated. The linear ODE was solved at each iteration using a 4th order Runge-Kutta scheme, and convergence was generally achieved in < 5 iterations. The result for one such droplet with volume 10µL and contact angle of 160° is given in Figure 1.11. Qualitatively, the droplet is noticeably distorted, although the exact impact on contact area is subtle.

To elucidate how the contact area changes as volume and contact angle increase, the numerical solution was obtained for a number of droplets in the same range as the energy ratio plot from Figure 1.10B. The plot in Figure 1.12 shows the ratio of contact area of a droplet distorted by normal gravity and a droplet free from gravity. Here it is quite clear that gravity indeed affects the contact area significantly for some droplets. For highly hydrophobic surfaces and droplets of 30µL volume, the true contact area is 60% larger than one would assume with a naïve spherical cap model. Even in less extreme cases that researchers might use to study wetting, the contact angle could be off by 20-30% if gravity is neglected.
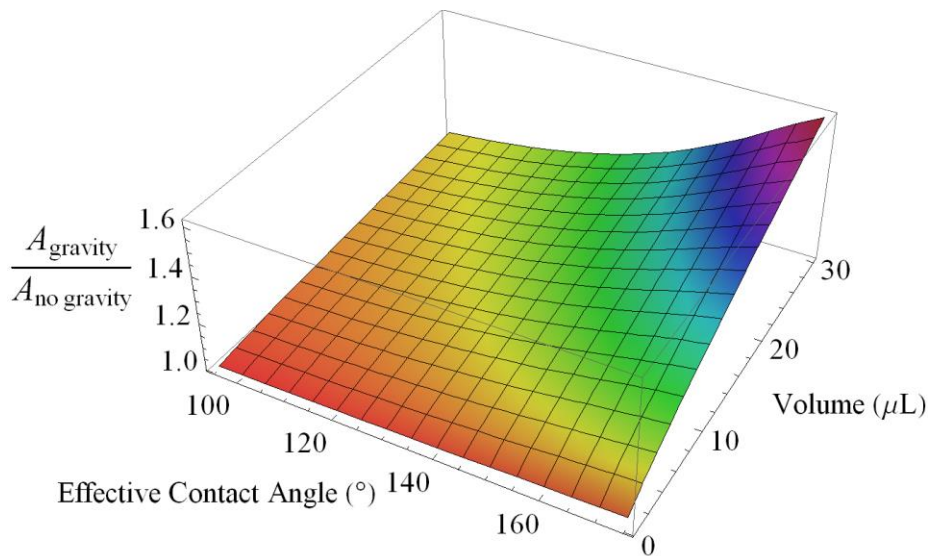

Figure 1.12: Comparison of contact area with and without gravity from numerical solution to the Young-Laplace Equation.

1.2.3 Surface Evolver Results

The above results all rely on straightforward numerical analysis requiring a continuous and homogeneous wetted surface. The SE model allows more realistic scenarios to be investigated in which the surface is discrete. Previous results from the SE model all included normal 9.81m/s² gravity to compare to experimental results. Now the gravity is removed and the results from equivalent models with and without gravity are compared. The trends predicted by the numerical solution are confirmed in that the discrepancy between gravity and no gravity increases as droplet volume and contact angle (related to the area fraction) are increased. Contact angle is also found to be relatively unaffected by gravity. Interestingly, the effect in the discrete model is even larger than that predicted by the numerical solution. Two examples of output from typical, large (20µL) droplets are displayed in Figure 1.13.
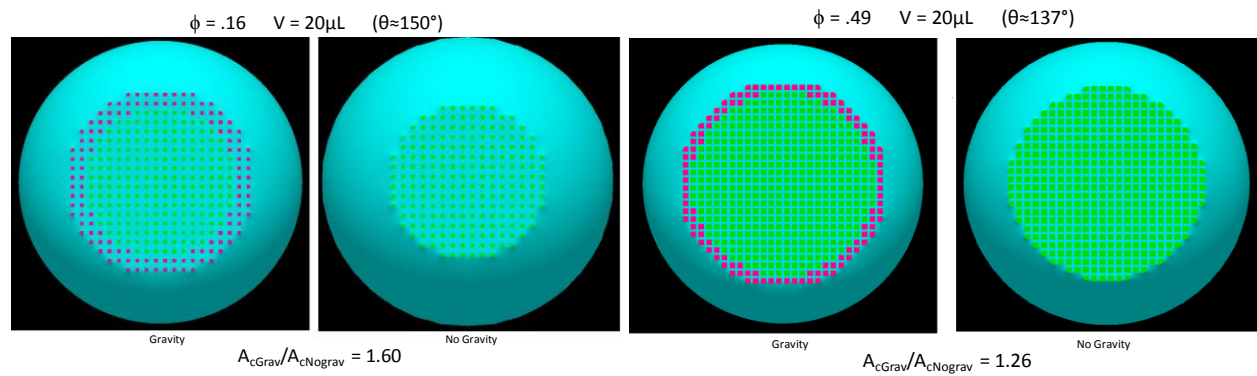
Figure 1.13: SE simulations with and without gravity. The pillars highlighted in pink are wet when gravity is included, but not when gravity is neglected.

The trend of greater increase in contact area for the discrete model is consistent, although it is not clear why it occurs. The effect could be physical, due to additional factors introduced by the discrete pillars, or possibly computational, due to the added component in the energy functional hindering convergence or the ability of the droplet to overcome small energy barriers to reach a lower energy state. In any case, the influence of gravity for a pillared surface is at least as great as for a continuous surface, if not more so. Researchers should keep this in mind during experiments and modeling if the contact area is to play a significant role.

1.3 Dynamic Droplets

In addition to the static shape of a liquid droplet, the dynamics of moving droplets on superhydrophobic surfaces present a rich opportunity to study wetting and pinning on a discrete surface. Dynamic droplet studies allow determining not just how hydrophobic a surface is, but how readily it wicks away fluids. This is more closely related to contact angle hysteresis than the hydrophobicity itself. In fact, a highly hydrophobic surface may actually be 'stickier' than the same surface with higher area fraction due to pinning and contact angle hysteresis [22].   A common way to study moving droplets and contact angle hysteresis in the past has been to use an inclined plane and gravity to identify the leading and trailing angles at which droplets become unpinned [23–25].

Here a novel experiment has been designed as described previously [26] allowing continuous monitoring of a droplet sliding along a superhydrophobic surface while also recording the force applied to keep it in constant velocity motion and the contact area. Briefly, a fluorescein salt is dissolved in water to allow high-speed imaging of the droplet contact area with an inverted microscope when the droplet is exposed to laser light. A PDMS sphere is attached to a high-sensitivity force sensor, which is 'adhered' to the droplet by surface tension to allow pulling the droplet while recording the force. See [26] for additional details. The focus here is analyzing the data from the experiment in order to extract information about the droplet's resistance to motion on the pattern, and to try and relate this to the behavior of the contact line.

1.3.1 Force Data Analysis

Initial experimental analysis addresses only the force portion of the data. The data is highly smoothed to analyze the simple, saw-toothed variation in the force and ignore higher frequency details. The force curve after the moving droplet reaches a steady state can then be roughly described as a periodic combination of two linear portions: first a gradual increase in force as the droplet is displaced, then a sharp decrease as the droplet depins and advances a row of pillars. Considering the displacement portion of the force curve, there are two characteristics that have been theoretically investigated before [27] but can be more closely scrutinized with this experiment. These are the effective spring constant of the droplet being displaced from an equilibrium pillar configuration, and the energy stored by the effective spring before jumping to the next equilibrium configuration (depinning). On the force curve,

18

these are the slope and the area under the curve, respectively, from the time the droplet settles after depinning until the next depinning event.

Algorithms were developed to extract this slope and area from the noisy saw-tooth data. In both cases the data was highly smoothed with a moving average kernel approximately $1/10^{th}$ the length of a cycle. The confounding factors involved were the high amount of noise and the irregular pattern of the force curve, which is not a perfect saw-tooth. There are many pillars at the leading and trailing edge that may not all depin at the same time, or the depinning sequence might change between cycles. This manifests as multiple smaller teeth superimposed on the overall saw-tooth pattern. From observation, the slope might be similar for all these smaller teeth, so we can collect those smaller linear regions if they can be identified as separate from the larger tooth they reside in. To find slopes, groups of data points were fitted with a linear regression, and if the quality of the fit was above a threshold, subsequent data points were added to the regression until the quality decreased by more than a second threshold due to adding the next point. If enough points were gathered in this manner, the segment was recorded along with the slope of the regression. Short segments and negative-sloped segments were discarded. This extracted data can be weighted for averaging using the number of points included in the segment.

Assuming this approximately saw-toothed curve, the same technique can be used to identify area under the curve for a single period. In this case there is a higher threshold on the number of points to be included in a segment, and a lower threshold on the regression quality. There is also the additional requirement that the starting point for the regression be a local minimum. Once the period is identified, the slope of the regression is ignored and Simpson's rule is used to integrate the actual data. Finding 'clean' segments for measuring energy is more restrictive as the full period should be linear. The results of this analysis and the slope analysis for one typical data set are given in Figure 1.14 where the width of a white bar indicate a region identified for measurement and its height is the magnitude of the measurement.
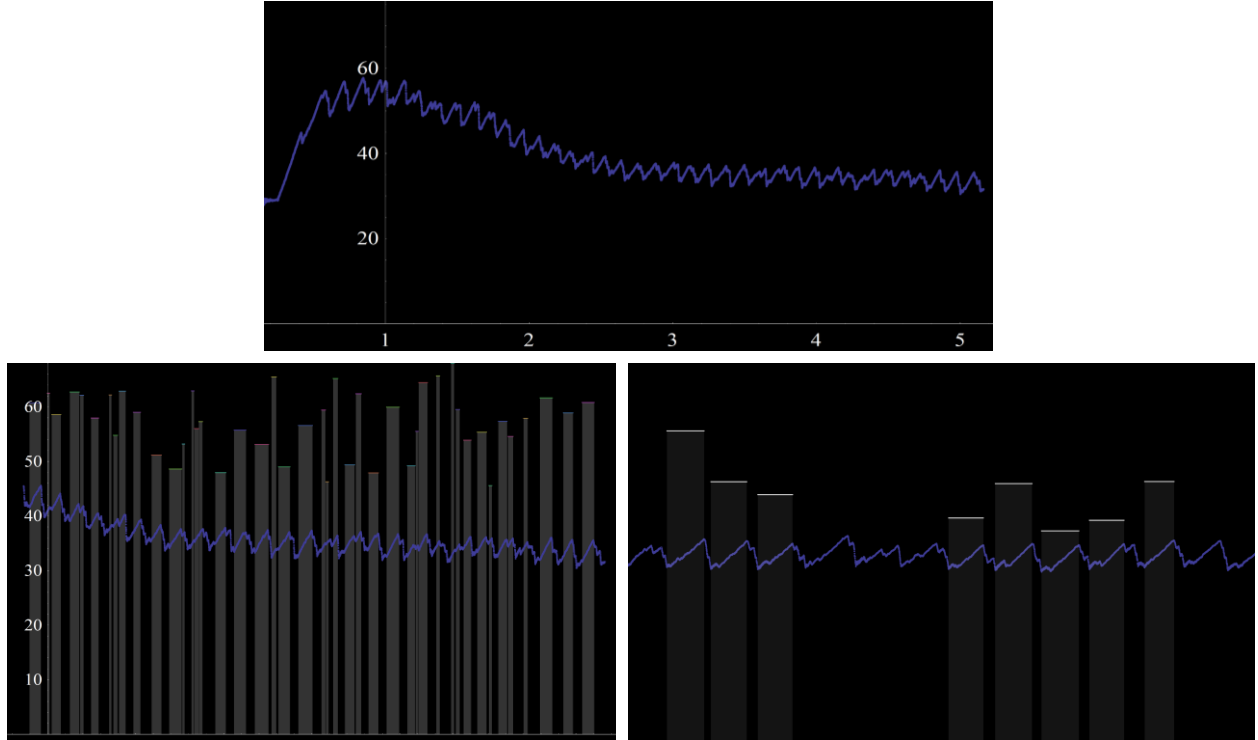
Figure 1.14: Extraction of spring constant (slope) and energy stored (integral) for a force data set. The width of the translucent bands indicate the region of the measurement and the band height is the value. Top image is the entire force curve for the test. Left are the extracted slopes from every interval where it remains consistent and positive. Right image shows a closer view of the area considered as part of the stored energy.

Regardless of the arrangement of the pillars, the slope of the force increases as area fraction *decreases*. This is interesting in that it might be opposite what we expect since lower area fraction is associated with a more hydrophobic droplet in this situation. Such an observation is not in agreement with prior work addressing pinning on dilute pillar surfaces where such a spring constant is found to decrease as the spacing of pillars increases or the size of pillars decreases [27]. However, the slope of the force is less well defined for high densities of pillars as there is less space between adjacent pillar edges. The average force for experiments on dilute pillars is still much lower than on high density pillars, but the fluctuations are more significant when area fraction is low. Relatively dense pillar arrays here may also void the dilute pillar assumption in [27]. The capability of measuring the forces during the entire process of droplet deformation and advancement is unique to this experimental platform. The topic is further discussed in [26], and the work is ongoing. It would be interesting to suppress the higher frequencies in the force curve so the force curve can be more precisely analyzed without the need for a large smoothing kernel.

1.3.2 Identifying Pillars

Correlating changes in the contact line to trends in the force curve requires identifying the contact line over numerous frames in the video. This is especially challenging because there are generally 5,000-10,000 frames from high speed video in a given experiment – too many frames to analyze by hand. A fast, automated method is needed to process all these frames while maintaining perfect contact line detection accuracy so a correlation may be performed. The task is complicated by the low signal to noise ratio of the wetted pillar tops, distortion produced by lensing from the curved droplet, and light flickering causing the image contrast to change each frame. The successful process flow was to apply a Kalman stack filter to mitigate flickering effects, then run a frequency band pass filter for a band ± a factor of 2 around the repeat spacing of the pillars to enhance the pillars. Finding the exact contact line is not possible manually or via image processing, but identifying the outermost wet pillars can be done. To identify wet pillars, the exact location of all pillars must be known. A subroutine accepts either automatically detected or manually selected pillar locations on the raw image and finds all centers to sub-pixel resolution assuming consistent spacing between pillars. This is done by optimizing an affine transformation from the integer pillar spacing to the image pixel spacing using iterative least-squares to minimize error while allowing for minute distortion and rotation of the pillar grid. Once the exact pillar locations are known in the image, an average is calculated about each pillar, and the image is resampled from the average so that each pixel corresponds to the average intensity in the neighborhood of a single pillar.

The processing described above greatly enhances the appearance of wet pillars, but additional logic must be applied to identify the exact contact line. Simply applying filters and a threshold is not sufficient to detect the wet pillars. The best method to extract the full contact line with few mistakes was to 'walk' around the edge of the droplet, following the pixel intensity gradient produced at the boundary between wet and unwet pillars. Starting from the clearest pillar at the trailing edge, the algorithm steps to one of the 8 adjacent pillars (cardinal and ordinal directions) that is most likely to be the next pillar along the contact line based on pixel intensities/gradients, contact lines in previous frames, and the current position relative to the whole droplet (maintaining convexity and approximate circularity). The stepping continues until the contact line arrives back at the first pillar. Each step to an adjacent pillar corresponds to a discrete edge in the contact line that can be used to characterize it.
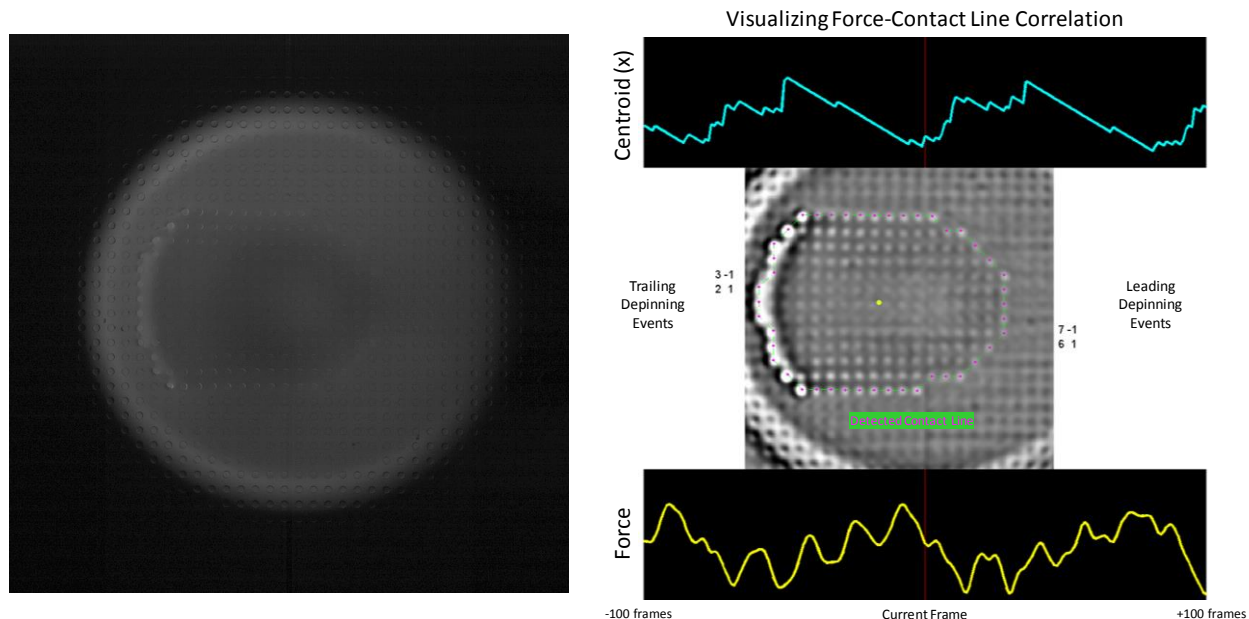
Figure 1.15: Left: One frame from the raw high-speed video. Right: The processed frame and visual output from the pillar identification.

The information gathered from identifying the contact line includes a list of every edge at the boundary, the center of mass, and the wet pillars comprising the leading and trailing edges as two separate vectors. This information can be visually rendered in a video along with the force for frame-by-frame comparison; one frame of such a video is given in Figure 1.15. Viewed alone, there is a very apparent dominant frequency in the video, and the force falls after a majority of the trailing edge depins in near synchrony. One intuitively expects this behavior to hold for smaller depinning events with corresponding small decreases in force. However, given the full analysis of the contact line, this does not appear to be the case. Evidence supporting the poor correlation between depinning events and force decrease is given in Figure 1.16. Notice that the major decreases in force correspond well to the major advancement of the center of mass (indicating depinning and advancement at the trailing edge of the droplet), and also correlation to a second, smaller decrease in force shortly afterward. Even so, multiple oscillations occur after the major depinning events that cannot be explained by the contact line alone. The flat areas in the center of mass curve in Figure 1.16 indicate no change in contact line and yet the force oscillates strongly during this period. There is certainly some relation between changes in

22

the contact line and changes in the force, but the situation is more complex than can be captured with linear correlation.
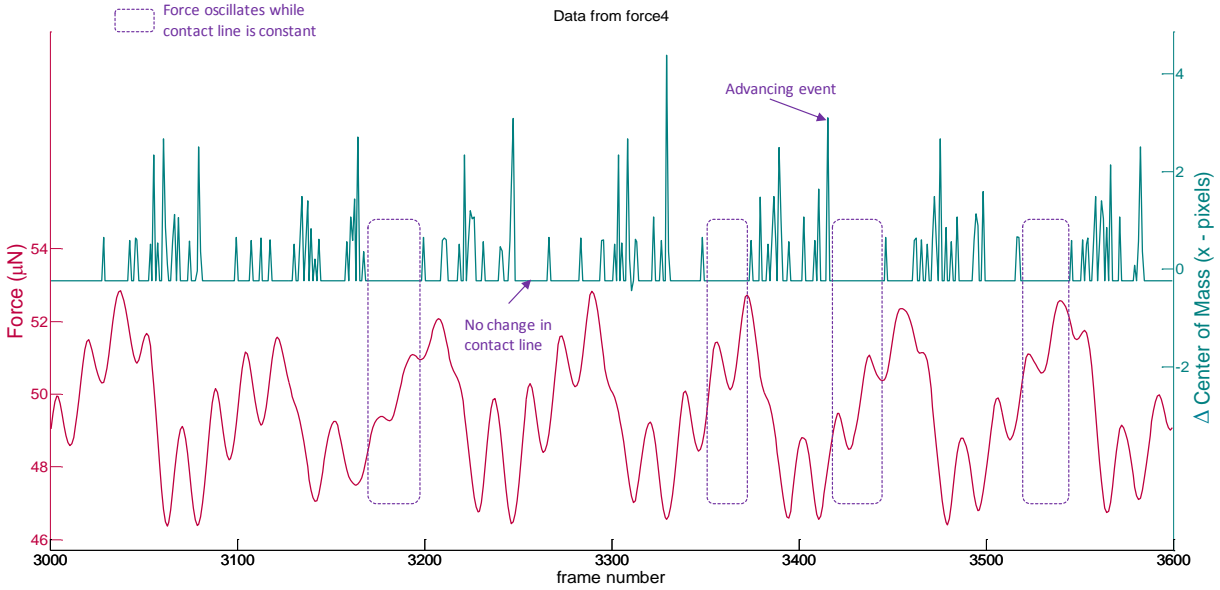
Figure 1.16: Plot of the change in contact area centroid above the smoothed force curve as a function of the frame number. Spikes in the centroid curve indicate depinning events. The circled purple areas are times when the contact line remains constant, but force still oscillates.

1.3.3 Anomalous Frequency and Droplet Oscillations

The particular plot in Figure 1.16 makes it apparent that there is a higher frequency mode in addition to the main mode associated with the droplet advancing one pillar. This is generally not as clear in other portions of the force data. A more precise analysis is performed by obtaining the discrete Fourier transform of the data series. The spectral data is plotted as a period plot in Figure 1.17, where the period and amplitude are rescaled so the dominant frequency lies at (1, 1). The plot confirms that there is unexpected spectral energy near 1/5th the primary frequency, which matches the apparent trend in the smoothed force curve.
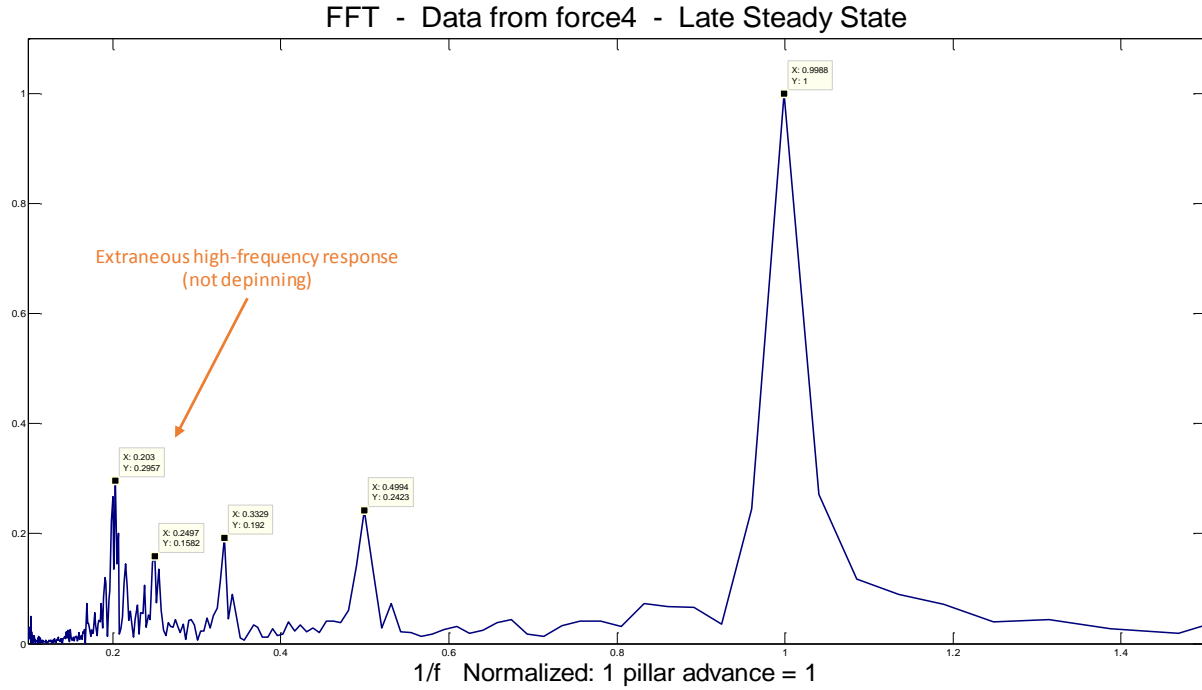
Figure 1.17: Period plot of the spectral data from a force-time data set rescaled so the primary frequency is unity. The large noise near 1/5th the primary period is too large and distributed to be a harmonic of the primary response, indicating that an extraneous frequency is present during the experiment.

This phenomenon cannot be directly explained by any feature of the contact line. Close inspection of raw video frames suggest the droplet may be oscillating or vibrating upon recoiling from advancing a row of pillars. This may be inherent to the experiment or the result of resonance from the measurement apparatus, or it may arise due to an unfortunate choice of stage motion speed. Further work will aim to improve the experimental design to remove these anomalous frequencies; it might allow a fuller understanding of how individual depinning events affect the dragging force exerted by the droplet.

1.4   Concluding Remarks

Work on the micro-scale droplets is still progressing on both the simulation and experimental fronts. For simulation of droplets with SE, a method for analyzing a receding droplet has been developed, but there is no analog for an expanding droplet. In order to better understand contact angle hysteresis, we must be able to compare the geometry of a droplet at equilibrium after expanding as well as after receding. In this case the model is somewhat more complex as the droplet must grow, adding facets and constraints when new pillars are wet. Such a model has been demonstrated for several specific cases, but a parametric version capable of automatically handling variety of geometries may be needed for a thorough comparison to the receding model. Additionally, this expanding droplet model, combined with the receding method may allow simulating quasi-static droplets in motion, comparable to the dynamic droplet experimental work. Modelling a moving droplet may help understand the changes in shape and energy occurring as the contact line of the droplet makes a discrete jump to new pillars.

For the experimental work, more data is needed to better understand the pinning and depinning processes. The anomalous forces must be fully understood and either accounted for or eliminated before a reliable correlation between individual depinning events and changes in the force curve can be made. Changing the speed at which the droplet is pulled and minimizing the impact of the pulling apparatus may help isolate forces not originating from the contact line. If a direct correlation between the contact line and measure forces is not possible, we still gain a better understanding of the droplet dynamics by identifying that the entire 3D nature of the droplet contributes to the forces resisting motion. In this case, there may still be conclusions to make about the global shape of the force curve that relate to large-scale changes in the droplet shape.

2. Wavy Patterns

Up until the late 1990's buckling generally was considered a mode of failure that might occur in a beam or cause delamination in films [28]. However, it was recently noticed that fascinating patterns arise when a thin film is compressed on a soft substrate [29], and that these patterns might be useful. Since then, a number of researchers have looked to make use of these wavy patterns. The results have had applications from cell biology [30], to optics [31], to stretchable electronics [32]. In each case, the theory and basic technique is the same: a relatively thin, hard film bonded to a softer, thicker substrate will buckle if it is sufficiently compressed. The buckling relieves the excess strain energy and results in a nearly sinusoidal topography where the wavelength is proportional to the film thickness but may vary significantly with the applied strain and mismatch in stiffness [33].

The buckling is initiated by the compressive strain mismatch between the film and the substrate, with the requirement that the film is more compressed than the substrate. A variety of methods have been used to apply this compressive strain, with popular methods being heating [34], differential swelling [35], and applying mechanical pre-strain to the substrate [36]. Different types of surface patterns may be achieved by modulating the direction of the strain – a quasi-1D sinusoid is formed under uniaxial strain while a 'herring-bone' pattern occurs when strain is biaxial or uniform [37]. Patterning the surface to relieve strain or add an underlying component to the wavy topography also has been done to create more complex patterns [34].

This portion of the text addresses the fabrication and characterization of these buckled patterns primarily intended for use in studying cell biology. The method for compressing the film is primarily uniaxial pre-strain of the substrate before depositing a film. Several variations of this technique are described for generating patterns with pitch or wavelength in the range of 100's of nanometers to several millimeters. The theory that allows the structure of the waves to be tuned is addressed, as well as practical methods that allow such tuning. The wide range of length scales also results in a number of techniques to measure the waves. One additional topic that is rarely discussed in the context of buckled wavy patterns is the quality of the pattern, which may vary significantly depending on the technique and processing conditions. Thus attention is given to improving the quality of these buckled patterns.

2.1 Theory

The equations governing the buckling of a thin rigid film on a compliant substrate can be solved
analytically. If the substrate is assumed infinitely thick, this is a classical mechanics problem.
Considering the context of the buckling we are working with here, one of the earliest formulations is
given in [36] where strain is assumed to be small. In fact, most of the samples used for buckling herein
have polydimethylsiloxane (PDMS, Sylgard 184) as the substrate, which is a highly stretchable elastomer.
Thus, a more accurate set of equations has been derived for large strains in [38]. It should be noted that
the only difference in the finite deformation model is the addition of the terms containing γ, which are
derived from equations for the shape of accordion bellows. The factor, γ, tends to 0 for small strains.
The values we are most concerned with are the critical strain above which buckling occurs, the
wavelength, and the amplitude. These are given in the following set of equations:

$$\text{Ratio of Plain Strain Moduli: } Q = \frac{E_f(1 - v_f{}^2)}{E_s(1 - v_s{}^2)}$$

$$\text{Finite Strain Factor: } \gamma = \frac{5\varepsilon(1 + \varepsilon)}{32}$$

$$\text{Critical Strain: } \varepsilon_c = \frac{1}{4}\left(\frac{1}{3Q}\right)^{2/3}$$

$$\text{Wavelength: } \lambda = \frac{2\pi h(3Q)^{1/3}}{(1 + \varepsilon)(1 + \gamma)}$$

$$\text{Amplitude: } A = \frac{h\sqrt{\frac{\varepsilon}{\varepsilon_c} - 1}}{\sqrt{1 + \varepsilon}\,(1 + \gamma)^{1/3}}$$

In these equations, the f subscript is referring to the film and the s subscript refers to the substrate. The
mismatch in strain between the film and the substrate (the film must be more strained) is given by ε,
and the thickness of the film is given by h. These equations give us all the information needed to
understand how to design a system with a desired wavelength and amplitude. Several observations
should be made regarding these equations: first, only the ratio of plain strain moduli is relevant, not the
modulus of either material alone. Second, both wavelength and amplitude are linearly proportional to
the thickness of the film. Third, the wavelength will increase as the film becomes harder relative to the

27

substrate, but only slowly with the cube root of the ratio. Fourth, the amplitude is somewhat independent of the ratio of moduli. This last point is important for understanding how to decouple the wavelength and amplitude to some degree. Although the two are strongly coupled by the film thickness, we may adjust the strain to change the aspect ratio. This is plotted in Figure 2.1 where the ratio of moduli is scaled logarithmically.
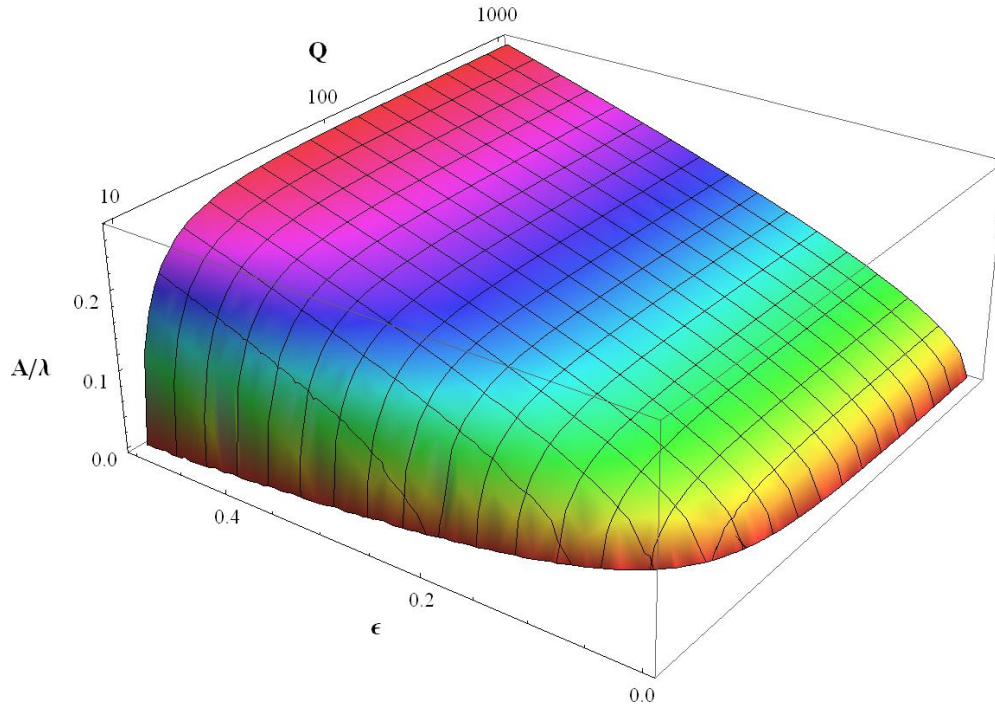
Figure 2.1: Theoretical aspect ratio of buckled patterns as a function of the stiffness ratio and strain on the thin film. High strain relative to the stiffness ratio yields sharper peaks.

2.1.1 Tuning Elastic Properties of PDMS

These properties can be exploited using PDMS. Sylgard 184 PDMS comes as a 2-part kit of base and crosslinking agent. While the standard mixing ratio is 10:1 base:crosslinker, the ratio can be varied to adjust the stiffness of the cured elastomer. Increasing the proportion of crosslinker leads to a stiffer material while decreasing the proportion makes the PDMS softer. For the standard mixture, the elastic modulus is roughly 1.8MPa and Poisson's ratio is 0.45 [39]. As discussed in the following sections, the elastic modulus can be varied over approximately two orders of magnitude. PDMS is also known to be linear elastic up to 40% strain [40], which makes it ideal for reaching any point on the surface in Figure 2.1.

28

2.2 Techniques

Numerous methods are available for producing a thin, hard film on a softer substrate. One of the allures of the fabrication method is that it does not require a clean room to produce micron-scale patterns; in fact much smaller patterns can be made that would usually require special equipment with conventional fabrication methods. The buckling technique also offers a way of producing surfaces without sharp edges at length scales where this could be very difficult or impossible. Three different techniques are covered here for how to generate waves at different length scales using PDMS as the stretchable substrate. Plasma-oxidation of PDMS has been used to reliably make wavelengths from 300nm up to 5μm. Sputter-coating metal onto PDMS can theoretically be used to generate waves from <1μm up to 100s of μm. Varying the base:crosslinker ratio to create PDMS with different stiffnesses has been used to make patterns of wavelength 150μm up to 1.5mm. Together, these different techniques should be able to cover the entire spectrum from very small to very large patterns using only PDMS as the substrate.

For all the fabrication techniques described below, the primary strain is applied with a uniaxial straining device. The straining device simply clamps two ends of a sample and stretches the sample by separating the two clamps. The device is shown in Figure 2.2. Two methods of clamping samples were built into the device, both of which work by compressing the sample under the rectangular compression plates. Figure 2.2A shows the bolt compression design while Figure 2.2B,C show the latching design, which is meant to minimize stresses during loading and unloading samples. Separation motion is produced by turning the knob attached to a 3/8" diameter, 1/8" pitch, ACME threaded rod. The clamp in the middle of the device has a corresponding nut to travel along the rod. Images from the CAD model for the design are available in the Appendix, Figure 6.1.
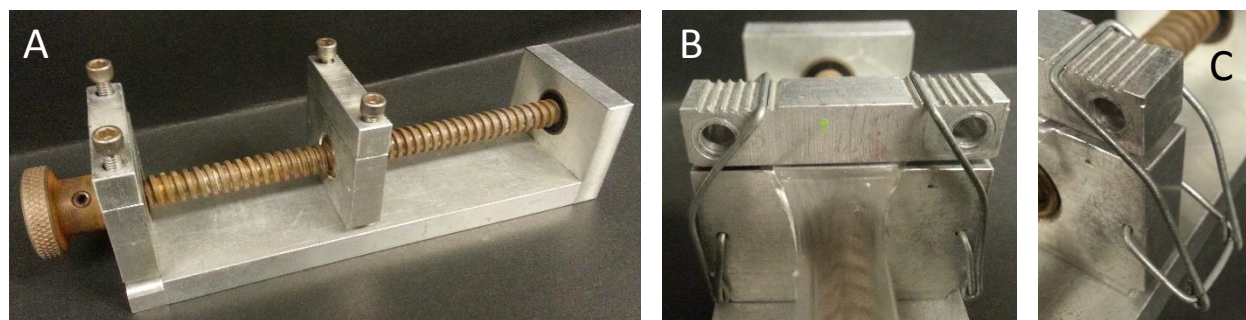
Figure 2.2: A) Full view of the strainer with bolts used to apply force to the compression plates. B) Close up of one clamping mechanism. The compression plate (with the two holes) can be turned sideways to switch between the bolt clamping and latch clamping. C) The latching mechanism allows quick loading and release while minimizing strain due to uneven clamping. The arm locks into a notch at the bottom of the image like the lock on a suitcase or tool chest.

2.2.1 Plasma Oxidation

Plasma oxidation is a process where a material is exposed to high energy electrons in the presence of pure oxygen at low pressure. The electron energies in the plasma may reach 20,000-30,000°C while the bulk of the sample remains close to the ambient temperature, inducing a variety of oxidation reactions that would not chemically occur, such as the cleavage of methyl groups attached to the silicon atoms in PDMS and replacement with oxygen [41]. This is a very common procedure applied to PDMS, and a number of researchers have exploited the thin oxide layer, not only as the thin film in this buckling process, but also to increase wettability and functionalize the surface in other contexts [42]. Conflicting reports exist for the exact properties of the oxide layer, which are difficult to directly measure. The oxide layer has been reported to be from 6nm – 500nm thick [43] with an elastic modulus anywhere from that of silicon oxide, 70GPa [41], down to about an order of magnitude greater than bare PDMS, 12MPa [44]. Realistically, the oxide layer is a diffused gradient near the surface that may additionally change over time due to the well-known hydrophobic recovery of oxidized PDMS [45,46].

Plasma oxidation of PDMS to produce a buckled pattern is carried out by first cutting out a strip of PDMS, then stretching it on the straining device. The sample surface is kept clean by using the PDMS immediately after it finishes curing, and then blowing nitrogen over the sample to remove dust before oxidizing. The PDMS is oxidized in a Diener plasma oxidizer with a maximum power of 200W, with the power common set between 100W and 200W for most experiments. For all experiments, the oxidation chamber is pumped down to 1mbar with oxygen flowing at a rate of 50sccm. The oxidation time is varied from 12 seconds to 20 minutes depending on the desired thickness of the oxide layer with 1-5 minutes usually giving the best results. After oxidation, the sample is removed from the chamber and allowed to rest for 10 minutes before releasing strain. Best results are achieved when strain is released very slowly and carefully by gently turning the knob on the strainer by hand in a smooth and controlled manner. A differential interference contrast (DIC) image of a typical buckled surface is given in Figure 2.3, and an atomic force microscopy (AFM) scan of a particularly nice section is given in Figure 2.4.
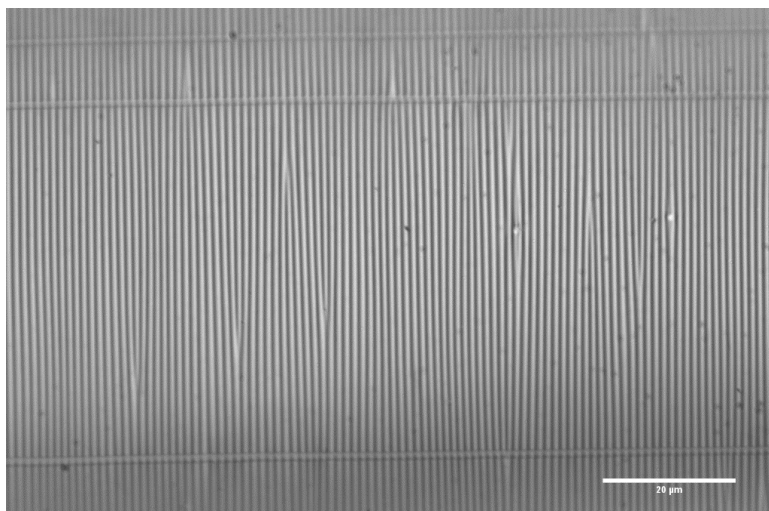
Figure 2.3: Optical (DIC) image of buckling pattern produced by plasma oxidizing PDMS.

Figure 2.4: AFM image of a buckled patterned produced by plasma oxidation. This is a particularly nice section, confirmed by the thinness of the side view in the lower portion of the figure, which indicated low roughness and high uniformity.

Name:N6-1   Wavelength:0.79031   Amplitude:98.0172   Accuracy:0.99679
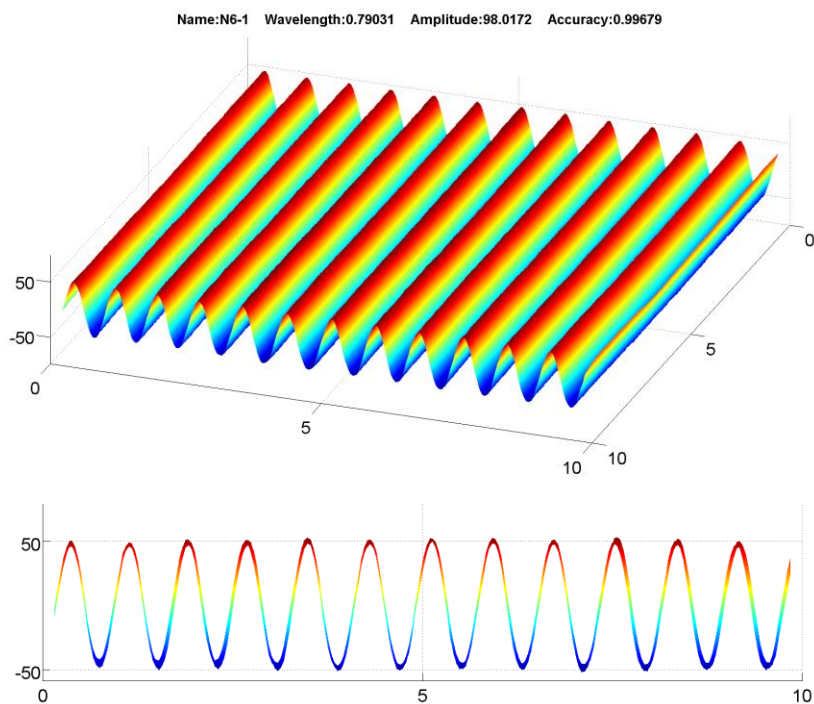
The parameters affecting the dimensions of the wavy patterns are the oxidation time, the oxidation power, the ratio of base:crosslinker of the PDMS substrate, the curing conditions, and the pre-strain. Additionally, the distance of the sample surface from the electrode during oxidation has a significant impact on the degree of surface oxidation, and thus the pattern. The parameter space can be narrowed by considering the theoretical equation: increasing the oxidation via time, power, or distance will increase the thickness and hardness of the film layer while changing the substrate properties affects the Q value. Section 2.3.1 addresses the variation of stiffness by altering the PDMS properties.

A number of different cases were studied with each of the described parameters varied. To simplify the results, data is only displayed from samples cured at room temperature for 36 hours where wavelength and amplitude were both measured using AFM. This data is listed in Table 6.1 in the Appendix as a list of results and process conditions. In practice, one can use the knowledge of the underlying mechanics as discussed in the theory section in order to predict the results of making small changes to one of the previously tested processes. There is variability between tests with similar conditions, so any prediction of wavy pattern properties will be an estimate.

It should be apparent from the image in Figure 2.4 that the quality of the buckled pattern can be very good, although there is significant variation at a larger scale, apparent in Figure 2.3. This behavior is typical for the technique. There are primarily two types of defects in the samples. The first defect type is the 'dislocation defect' similar to the phenomenon in a crystal lattice with the same name. The ridge of one wave ends and neighboring ridges displace around it. A single line scan from AFM data of a buckled pattern near a dislocation defect is given in Figure 2.5. This shows that the pattern is very close to a perfect sine wave in many regions, but also that the sine wave is distorted near the defects. The other major defects are the cracks running axially that form due to lateral strains induced by the Poisson effect. These defects are mentioned later in the section.

Red = Sin Fit
Blue = Connected Data Points
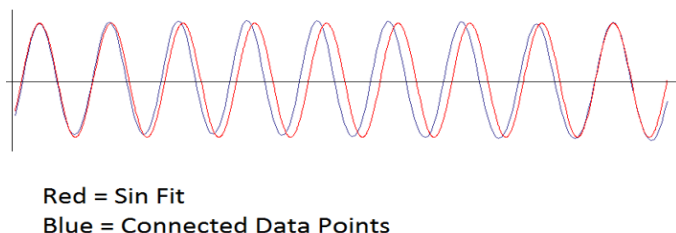
Figure 2.5: Line scan of buckled pattern (blue) compared to an ideal sine wave (red) near a dislocation defect. The overall match is quite good, but there is distortion near the center.

2.2.2 PDMS-on-PDMS

Larger patterns can be made by using PDMS for both the film and substrate. The film is made harder by either increasing the base:crosslinker ratio and/or increasing the curing temperature as discussed in section 2.3.1. Care must be taken to ensure that Q is sufficiently large to cause buckling as the stiffness ratio between different formulations of PDMS may be relatively small. The critical strain is solely a function of Q as given in theory section above, so this strain should be calculated and exceeded during

fabrication by a reasonable margin of error. The necessary strain to induce buckling may be on the order of 10-50%.

The PDMS film component of this buckling system must be made much thinner than the substrate. If the film is not sufficiently thinner than the substrate, global buckling will occur rather than the local, wavy buckling desired [47]. The PDMS film is made thin by spin coating. To do this, a silicon wafer or square glass slide must be coated with a fluorinated silane to make it non-stick (see 2.2.5 for treatment details). Here, the silane may be rubbed directly onto the glass or silicon, and the reaction will occur faster than for PDMS (<30 minutes). To spin coat, uncured PDMS is poured to evenly cover the wafer or slide before mounting a spin coater (the spin coater used here is Specialty Coating Systems P6700 Spin Coater). The spinning speed will control the thickness of the film. Figure 2.6 details the relation between spin speed and film thickness. The data is compiled from previous students and the current work using the standard 10:1 mixture of PDMS – note that increasing the proportion of base, which is more viscous than the crosslinker, will result in a thicker film than predicted. The film thickness is well fit by a power law, and is relatively independent of the spinning time [48]. The spin time used here and suggested for future studies is 5 minutes, which ensures an even coat across the surface.

PDMS Spincoating

$$\text{Thickness} = 39845\text{rpm}^{-0.912}$$
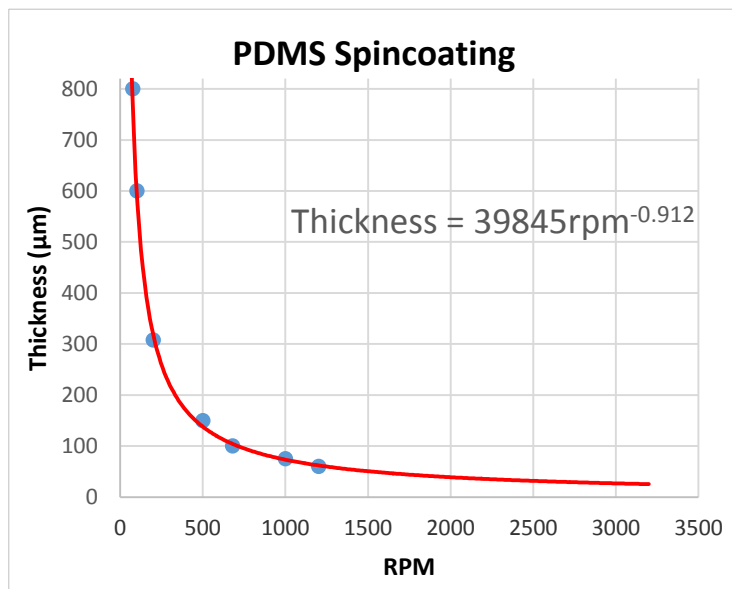
Figure 2.6: Spin coating and thickness of PDMS film. The curve relates the spin speed to the film thickness. Samples are 10:1 PDMS spun for 5 minutes at the indicated spin speeds.

Once cured, the PDMS film is manually peeled away from the wafer or glass slide surface and wrapped around the outside of a scintillation vial. This will allow the film to be rolled onto the substrate surface

during bonding. Figure 2.7 illustrates this process. To bond the PDMS film to the PDMS substrate, both

sides of the interface are plasma oxidized in the same oxidizer used to generate smaller wavy patterns.

The substrate is pre-strained, and then both the scintillation vial/film and substrate are oxidized using

the conditions previously described. The oxidation time can be very short, such as 15 seconds at 100W.

When the oxidation is complete, the film and substrate must be removed quickly from the oxidizer and

bonded. As seen in Figure 2.7, the film is aligned with the substrate and then slowly rolled to make

smooth contact along the length of the film. The film should be allowed to form a strong bond to the

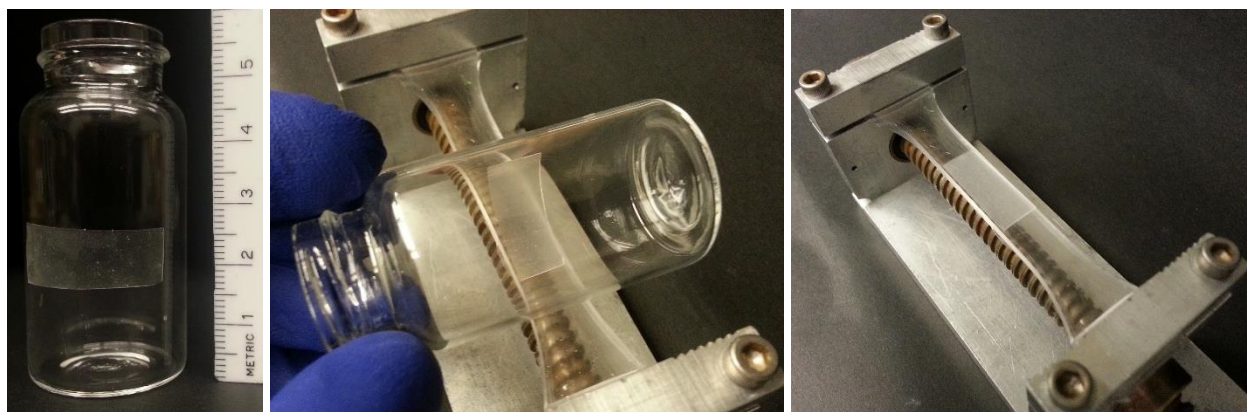substrate for at least an hour before releasing the strain.

Figure 2.7: PDMS film to PDMS substrate transfer procedure. From left to right: the film is wrapped around a scintillation vial. The substrate and film are then oxidized. The film is then aligned with the substrate and rolled onto the surface to ensure even and strain-free film transfer. The film should look like the right-most image – smooth and not extending over the edges of the substrate.

Patterns produced by this method can be well-predicted by the equations in the theory section if the

elastic moduli and film thickness are known ahead of time. Wavy patterns with wavelengths as low as

180μm have been produced with this method. There is no physical reason the patterns can't be made

smaller than this. The practical limitation imposed here is due to the method of manually peeling the

film off of the wafer and placing it on the scintillation vial – films thinner than 50μm or so are very

difficult to manipulate by hand. The films themselves can be made much thinner (on the order of

microns) by increasing the spin speed or mixing the PDMS with a suitable solvent before spinning [49,50].

For future work, the film could be spun onto a flexible material than would allow handling to oxidize and

transfer it to the substrate. Brief tests with a few readily available flexible materials, such as plastic

transparency film, either didn't yield an even film or did not properly transfer to the substrate. These

problems could be solved with better materials.

2.2.3 Sputtering

An alternative method of making a thin film on a PDMS substrate is to directly deposit it via sputtering. This method is somewhat more involved than the other two methods discussed in that it requires fairly specialized equipment. A similar effect can be produced by depositing metal in the vapor phase [29], although we have not attempted this ourselves. Sputtering has the advantage over the other techniques by being the most versatile in the dimensions of the waves. The thickness of the deposited layer can be modulated from as little as 5nm to over a μm if the sputter time is significantly extended. Exceptionally small waves, however, are not practical with PDMS as the metal will be significantly harder than the substrate. Known suitable metals for sputtering onto PDMS are chromium and titanium, which are often used as an intermediate layer for depositing other types of metal on PDMS. Unfortunately, these metals are particularly hard (280GPa, 115GPa) and brittle, a problem discussed in the later sections. Aluminum is softer (70GPa) and more ductile than chromium. It may be a more suitable material for future experiments, although its effectiveness is not known.

The method of performing the sputter coating is similar to the previous methods where the uniaxial strainer is used to stretch a strip of PDMS. The strainer cannot be directly fit in most sputtering machines, so custom-made plates were machined to replace the standard sputtering plates (3" diameter, ¼" thick) while holding a pre-strained sample. The sample is strained, clamped onto the plate, and then cut to hold the strain during sputtering as seen in Figure 2.8. The sample is suspended between the camped points without contacting the disk to allow for expansion and contraction. The machine used for the results presented below is the Cooke Dual-Gun Sputter system. The chamber is pumped down to 2.0 E-6 torr before flowing argon into the chamber and applying a 100W DC current to initiate the sputtering. This sputterer also has a heating feature which might be used for future experiments.
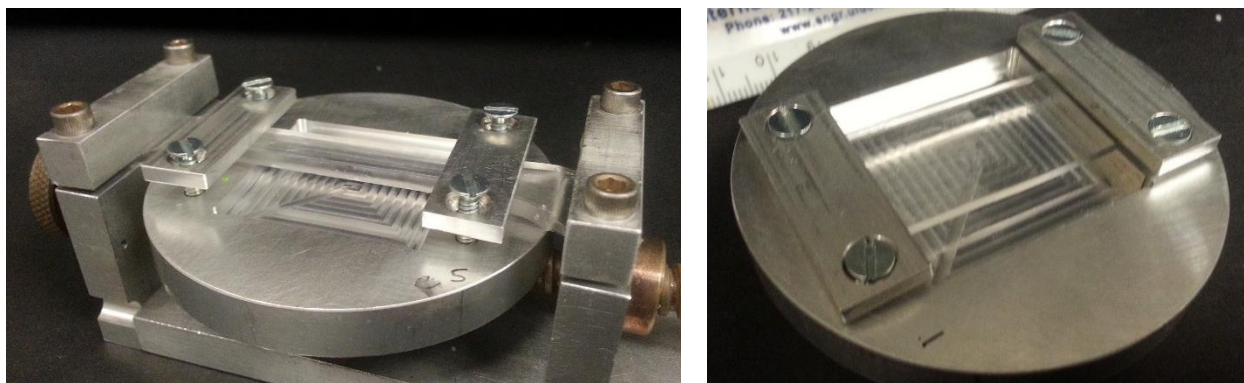
Figure 2.8: Custom disk used for sputtering on strained samples. Right: disk holding a strained sample before sputtering. Left: illustration of the straining and loading process. The sample is strained and the disk slides between the threaded rod of the strainer and the bottom of the sample. The plates are then screwed down and the excess sample is cut away.

Results from sputter-coating chromium to a thickness of ~10nm with 5% pre-strain are given in Figures 2.9 and 2.10. The qualitative appearance of the pattern is very similar to oxidative buckling on PDMS. Chromium is very brittle, and the compliant nature of PDMS makes it very easy to bend the substrate and apply destructive stress to the film. The chromium film cracks readily as in Figure 2.9, where the diagonal direction of most cracks indicate that these cracks formed in part due handling after the pattern had formed. This cracking was common in optical images and perhaps due to loading the sample on the microscope.
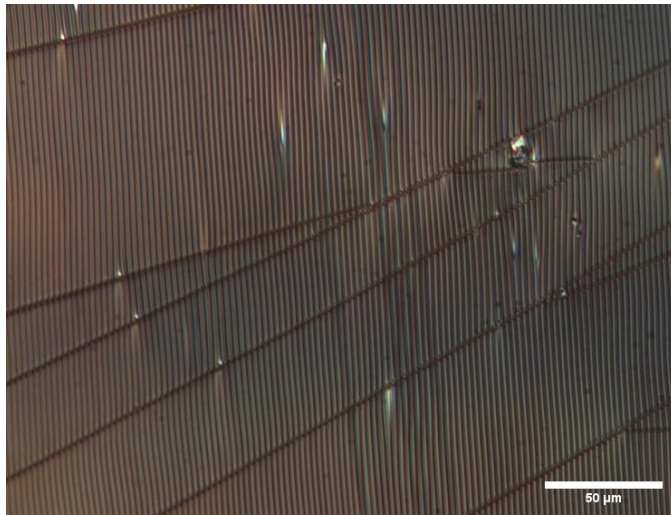
Figure 2.9: Optical (DIC) image of buckled pattern produced by sputter-coating chromium onto PDMS.

Figure 2.10: AFM image of the same sputtered chromium pattern as in the figure above.

Name:CR1-1   Wavelength:2.1373   Amplitude:281.3639   Accuracy:0.98523
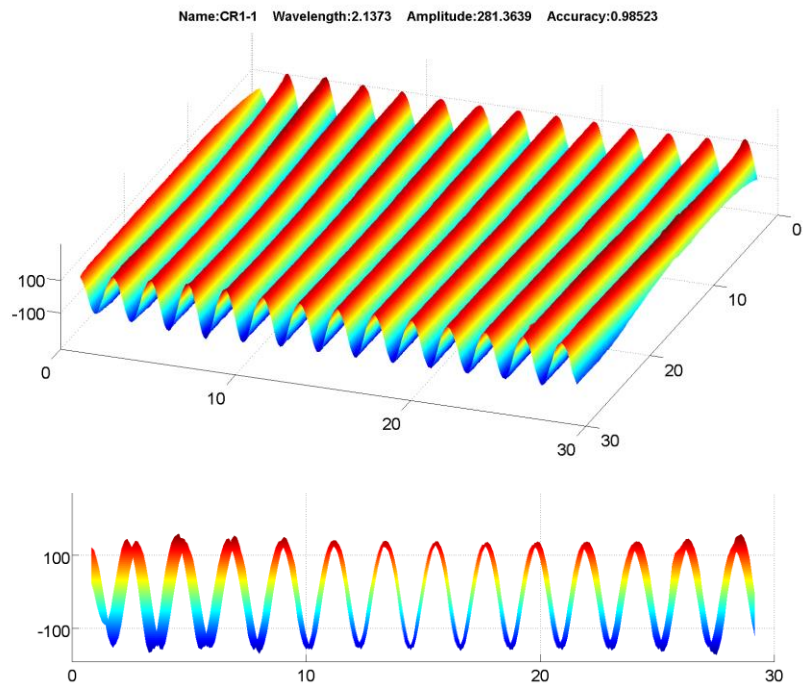
2.2.4 Diffraction Gratings

Using commercial holographic diffraction gratings for their surface pattern has not been reported previously to the best of our knowledge. This is the quickest and the easiest method of producing a wavy patterns with <2µm wavelength. Holographic diffraction gratings are typically used in optics to separate different wavelengths of light, and thus have a very tightly controlled quality. The surface is approximately sinusoidal and very uniform over larger areas. Diffraction gratings are made with a laser

holography process similar to a groove fabrication method previously described [51,52]. Standardized gratings are made with pitches in the range of 200nm – 2µm wavelength, a range relevant for inducing cell alignment [53]. Although the patterns come with a predetermined groove depth, the surface is fragile and tends to wear down over time. The wearing reduces the amplitude but leaves the wavelength unchanged, which allowed us to generate several different aspect ratios using a few master molds.

Figure 2.11: Fused silica diffraction gratings from Edmund Optics. The apparent color is due to white light diffracting off the surface and being separated into its component wavelengths.
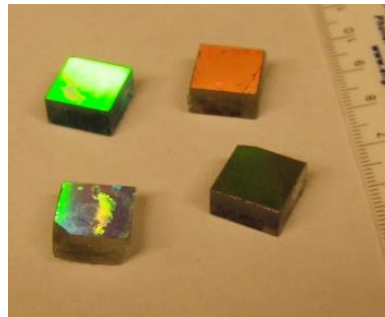
Holographic patterns used for cell biology experiments were purchased from Thor Labs and Edmund Optics. A picture of some of the gratings used to make patterns in PDMS is given in Figure 2.11. The patterns are sold by the number of lines per millimeter with the available line counts generally being 600, 1200, 1800, 2400, and 3600 lines/mm where 600 lines/mm is 1.667µm wavelength and 3600 lines/mm is 278nm wavelength. Information about the exact surface profile and depth are not available, but gratings are typically sold with separate versions available for use in the visible light spectrum and the UV spectrum. The depth of the visible spectrum patterns is larger than those for the UV patterns, presumably due to the shorter wavelength in the UV spectrum. Although most of the patterns used for quantitative cell experiments were of a high quality fused silica design, diffraction gratings are also sold in bulk as a plastic sheet. The plastic is not only cheaper, but disposable and easier to work with. The patterns have been observed to be slightly rougher, but they are equal or better than the fused silica variety for inducing cell alignment. Sheets of plastic grating are available commercially in 1000 and 2000 lines/mm.

Name:1000A-1   Wavelength:0.99448   Amplitude:185.3433   Accuracy:0.97713
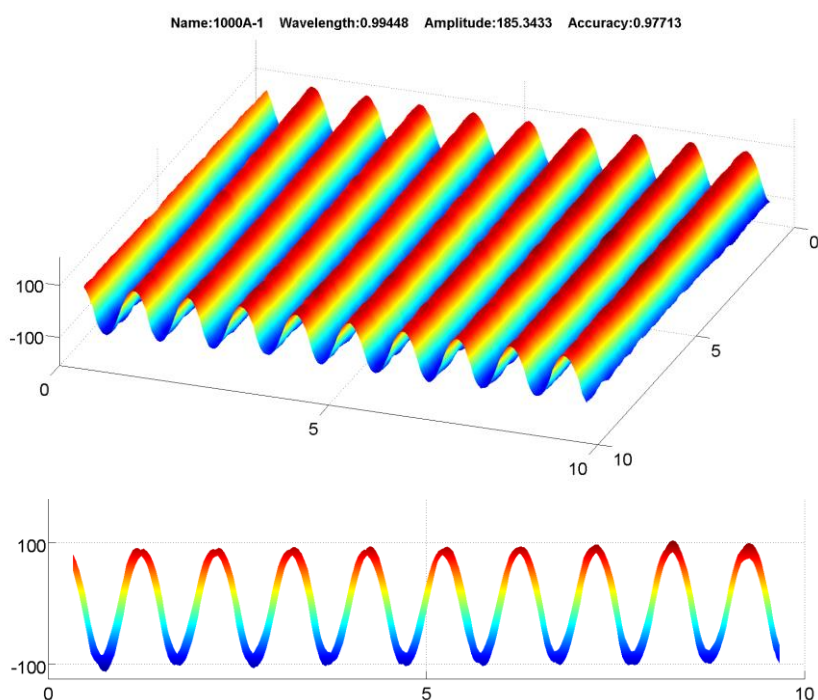
Figure 2.12: AFM scan of a 1000 lines/mm plastic diffraction grating that has been replicated with PDMS. The thicker appearance of the side view (lower part of image) indicates that the surface is rougher than the buckled patterns.

2.2.5 Replication and Use for Biology

The pattern generated by any of the above methods may be transferred to an epoxy mold rather than directly creating a stamp in order to make a reusable master pattern. Most epoxies will not stick to silicone, although there are exceptions – one tested epoxy that works for this purpose is the "Standard" formulation of Loctite 5-Minute Epoxy, which reproducibly molds wavy patterns down to 300nm wavelength. Regardless of the buckling method, if the surface of the pattern is hydrophilic, the pattern should be 'fluorosilanized' to make it non-stick. To do this, tetrahydrooctyl(1,1,2,2)-tridecafluoro-dimethylchlorosiloxane (TDFS, Gelest Labs) is applied in a fume hood. If the surface is oxidized PDMS, the TDFS (a liquid as purchased) need not be placed directly on the surface and can instead be placed inside a sealed container with the pattern. Some of the TDFS will vaporize and react with the oxide layer as a gas, forming a monolayer of fluorinated carbon chains at the oxide surface. This might be useful if there is any concern about swelling due to absorption of the silane by PDMS, i.e. for very small patterns. In other cases, the TDFS can be placed directly on the surface being modified, and it will yield a similarly non-stick surface. In either case, 50µL of TDFS is sufficient to treat all the material in a standard 100mm culture dish, and the reaction should be carried out for >1 hour for oxidized PDMS or >24 hours in all

39

other cases. The volume may be adjusted from this reference to containers of different sizes. Excess TDFS should be rinsed away with methanol and dried with flowing nitrogen to prevent exposure to harmful vapors. If the patterned surface is not hydrophilic (non-oxidized PDMS), then it won't adhere to the epoxy and need not be treated.

The epoxy is prepared as instructed being very careful to not introduce bubbles during mixing. A thin layer of epoxy is applied to the PDMS-on-PDMS wavy pattern and also on a glass slide that will hold the epoxy replica. The two epoxy surfaces are then pressed together, again being careful not to introduce bubbles into the epoxy. To cure, the mold should be placed with glass slide facing up and buckled PDMS side down so air bubbles will rise away from the patterned surface. Light pressure should then be applied by placing a weight on top of the glass slide, which will ensure and even surface. After at least an hour (if using 5-minute epoxy), the PDMS pattern can be peeled away, and the epoxy should be further cured in an oven at 60-80°C for >8 hours. After curing, it is recommended to use hot glue to create a barrier around the boundary of the pattern such that PDMS poured on top of the epoxy will remain within the barrier, allowing regulation of the thickness of the copy. This mold should now be reusable indefinitely for making PDMS copies. This mold with hot glue applied should look like Figure 2.13.
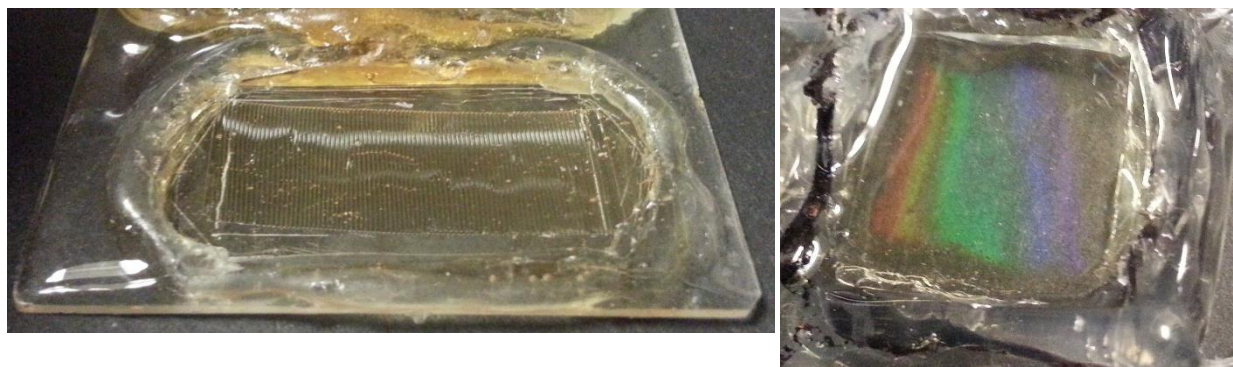
Figure 2.13: Epoxy copies of buckled patterns with surrounding barrier of hot glue to contain PDMS on the pattern during replication. Left: 330μm wavelength buckled pattern copy. Right: 1.6μm commercial diffraction grating copy.

To prepare the pattern for culture, more PDMS is used to make a copy of the epoxy mold. The PDMS should be degassed until no bubbles remain and then poured on the epoxy mold (or pour first and then degas). Allow the uncured PDMS to evenly spread and begin to solidify by leaving it on a flat surface at room temperature for >12 hours. Afterward, the mold can be cured in an over at 60-80°C for >2 hours.

The pattern can then be removed from the mold and cut out into the desired shape for use in culture. After cutting to size, apply TDFS to the patterned PDMS and allow to sit in a fume hood >12 hours. Rinse with methanol and dry to remove excess TDFS. The pattern should now be non-stick and unreactive, so it may be used to imprint the surface pattern onto other material. The suggested use is to pour PDMS into the desired culture container, then drop the nonstick pattern on top, degas, and allow to cure. After removing the nonstick PDMS, the pattern remaining may be coated with ECM proteins or gel and used in place. It may be necessary to briefly oxidize the surface for 30 seconds in order to allow the gel or protein to wet and adhere to the surface. The final product before adding protein or gel should look like Figure 2.14.
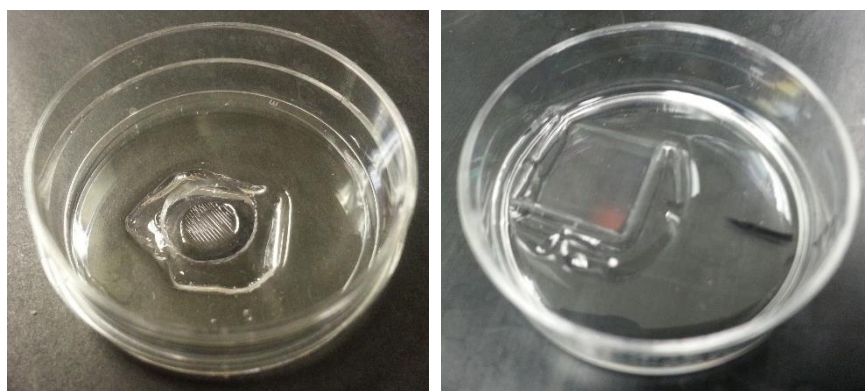
Figure 2.14: Patterns in 35mm dishes ready for culturing cells. Left: 330µm buckled pattern copy. Right: 1.6µm commercial diffraction grating copy.

An alternative replication method particularly useful for PDMS-on-PDMS buckled patterns where the pattern is stable in the strained state, is to produce a stamp that can be immersed and replicated in culture dishes. This is done by bonding the buckled pattern to a glass slide so that the glass slide rests on the lip of a culture dish and the pattern extends into the dish. The dish is then filled with the replication material – PDMS as described here, but a hydrogel could also be directly printed patterned.

Depending on the desired thickness of the replica in the culture dish, a layer of PDMS could be built up on top of the glass slide so the stamp will extend the necessary distance into the culture container. This can be done by cutting out several slabs of PDMS in the shape of the buckled pattern and then bonding them to each other and to the glass slide. The bonding can be done via plasma oxidizing both faces for 30 seconds at 100W or by using 100% silicone adhesive/sealant (Dow Corning). Either way, the bonded parts should be left in an oven at 60°C for 24 hours after bonding. The edges of the stack of PDMS strips will likely be rough and irregular at this point, so they must be cut into a tapered shape like a pyramid.

Starting at the top (the patterned face) with a razor blade, cut down to the base of the stamp (the glass slide) tapered slightly so that the stamp is wider near the glass slide than it is at the buckled face. Repeat the cutting for each side of the stamp. Once the pyramid-shaped stamp is cut and each side is tapered, one may wish to apply another layer of silicone sealant or PDMS if the edges are not smooth and flat. Apply TDFS to the finished stamp as described above to make it nonstick. Figure 2.15 shows a picture of a completed stamp.
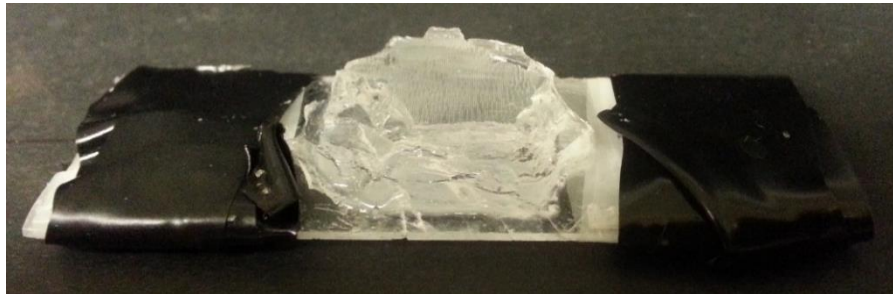
Figure 2.15: PDMS/Silicone sealant stamp mounted on a 3" x 1" glass slide with some additional black electrical tape. The pattern is inverted and the taped area is placed on the rim of a 35mm culture dish. PDMS is added to submerge the patterned top of the stamp

To make a pattern at the bottom of a divot, pour PDMS into a 35mm culture dish and then place the stamp, inverted, so that the glass slide rests on the lip of the 35mm culture dish and the patterned top of the stamp is slightly submerged in the uncured PDMS. It is important to submerge the patterned side of the stamp at an angle as if peeling from the surface in reverse so air is not trapped at the pattern surface. Degas the PDMS, and the construct can be immediately cured at 60°C for >4 hours. An X-acto knife will be required to gently separate the stamp and the printed pattern without damaging the stamp. The final product should look like Figure 2.16.
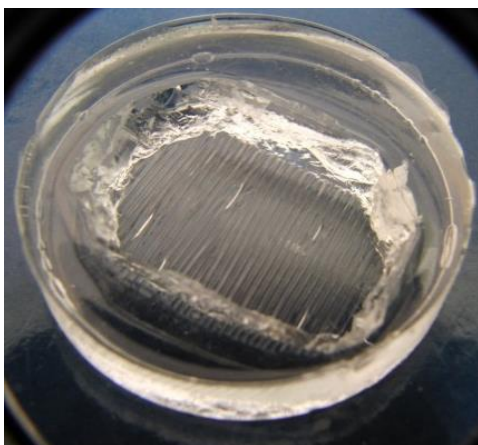
Figure 2.16: Result of copying the stamp in the figure above. The embossed pattern is convenient for filling with hydrogels.

Patterns may also be replicated as and used as thin films. This is particularly relevant for submicron wavelength patterns because they may be viewed with high numerical aperture objectives. The focal length of such an objective can be <200µm. This short distance can be accommodated by mounting the pattern directly on a piece of cover glass. Following the same procedures outlined above, the final step is replaced by printing the PDMS directly onto this cover slip with weight applied on top of the mold to keep the pattern thin and flat. To use this pattern in culture, a hole is drilled in the bottom of a culture dish with a drill press. This is a convenient method for ensuring good optical properties of the sample with longer-focal-length objectives as well. The process and outcome is illustrated below in Figure 2.17.
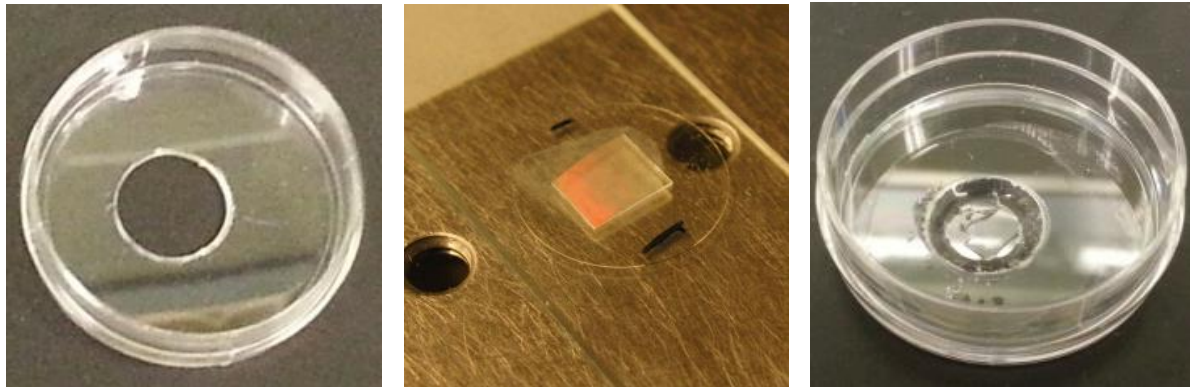
Figure 2.17: Process of making a very thin PDMS pattern for cell culture. From left to right: first a hole is drilled in the bottom of a 35mm culture dish. Then the pattern is compressed against and cured on a #1 glass cover slip. Lastly the cover slip is glued to the bottom of the culture dish with PDMS, replacing the drilled hole.

2.3   Measurements

2.3.1   Tensile Testing

Sylgard 184 PDMS is a very commonly used material, and a great deal of literature is available on its various physical properties [39,40]. However, less publicly available information is available on how the modulus of the PDMS varies with different curing conditions. Not only does the ratio of base to crosslinker affect the modulus of the cured product, the temperature and time of curing also play a nearly equally significant role. The influence of the temperature on the modulus is not well documented, and a naïve researcher viewing the manufacturer's recommendations might assume any of the documented curing methods (48 hours at room temperature, 10 minutes at 150°C, 20 minutes at 125°C, 35 minutes at 100°C) will result in the same mechanical properties. This is not quite the case, and extending the curing time beyond this has significant effects. This section documents a simple method of performing tensile tests with PDMS specimens with varied cure time and compiles the results.
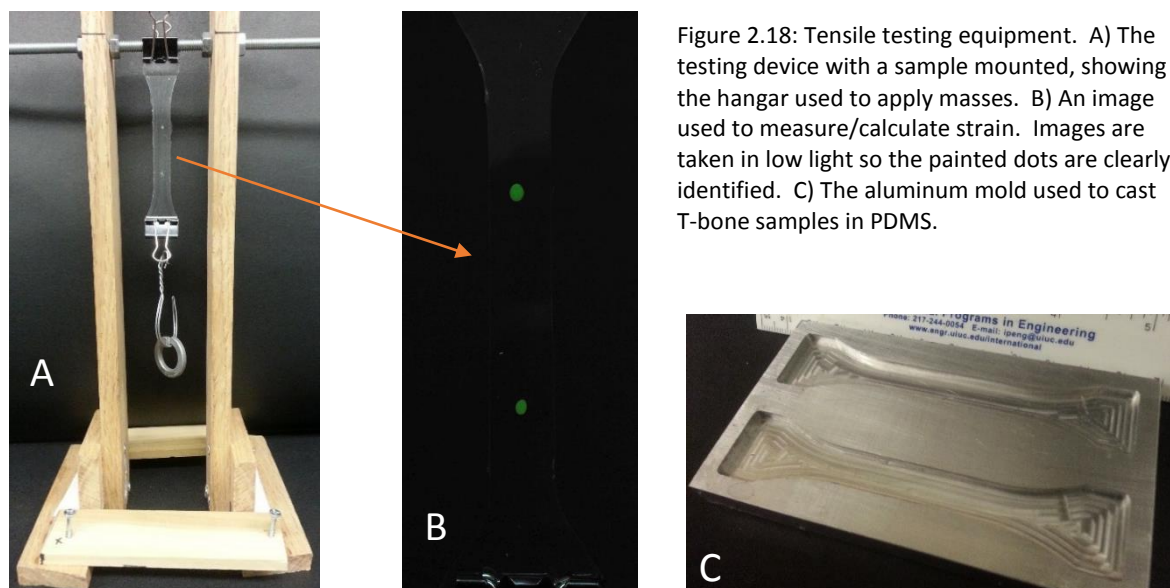
Figure 2.18: Tensile testing equipment. A) The testing device with a sample mounted, showing the hangar used to apply masses. B) An image used to measure/calculate strain. Images are taken in low light so the painted dots are clearly identified. C) The aluminum mold used to cast T-bone samples in PDMS.

Stress-strain curves for PDMS samples were produced using a custom built straining device and an optical method of measuring strain. The tensile testing device is simply a stand to allow unhindered application of weights to the specimen. The device can be seen in Figure 2.18A. The weights are labelled with a precise measure of their actual masses, and stresses are calculated by dividing the mass

by the measured cross-sectional area. Samples used were fabricated in a "T-bone" shape using the aluminum mold in Figure 2.18C. This shape ensures a consistent cross-section and no nonlinear effects from the sample geometry. Strains were measured in the necked regions.

Data points are collected by adding weights to the hangar clamped to the bottom of the specimen and then using a camera mounted on a tripod and fitted with a macro lens to take a picture of the equilibrium displacement. An example image of the strained specimen is given in Figure 2.18B. Colored dots are painted on the surface of the specimen and serve as markers allowing determination of strain. PDMS is linear elastic over a large range of strains, so the applied strain can be very large such that it is easily optically visible. Images are processed in ImageJ by isolating the color channel corresponding to the color of the painted dots, which are easily detected by applying the "Find Maxima" function in ImageJ. The separation of the centroids of the dots is calculated for each image, giving the strain when divided by the original length. Calibration is not necessary – all length can be measured in pixels. The accuracy of this method can be confirmed by inspecting the stress-strain plots, such as the typical plot in Figure 2.19. The curve is highly linear, as expected, with a good fit quality. Further confirmation can be obtained by painting multiple dots along the length of the neck region and checking if the strain is consistent throughout the necked region, which it is.

Figure 2.19: Typical stress-strain curve produced by this tensile testing method. Usually ~15 data points are used to calculate the elastic modulus. The slope of the fitting function gives the modulus, 2.366MPa for this sample.
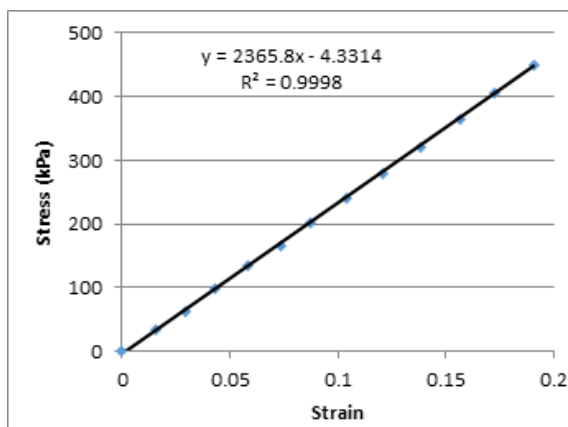
Samples were fabricated with base:crosslinker ratio in the range of 8-40; curing time in the range of 0-48 hours; and curing temperature in the range of 60-150°C. The results can be summarized by the two plots in Figure 2.20. We can look at the impact of each parameter in isolation. Increasing curing time will increase the stiffness up to a point, and then no more. For samples cured at 60°C (a common temperature to use because it is the maximum polystyrene can withstand) maximum stiffness is reached

after ~36 hours with negligible gain thereafter. The maximum stiffness time at higher temperatures appears to be shorter, although this wasn't explicitly tested. The plateau in stiffness with time seems to indicate that the crosslinking reaction has gone to completion. Temperature has a more significant impact than the curing time. Samples cured for an hour at 150°C are significantly stiffer than samples cured for 48 hours at 60°C. PDMS begins to thermally degrade around 200-250°C [54], so it is feasible that harder samples could be produced by further increasing the temperature.
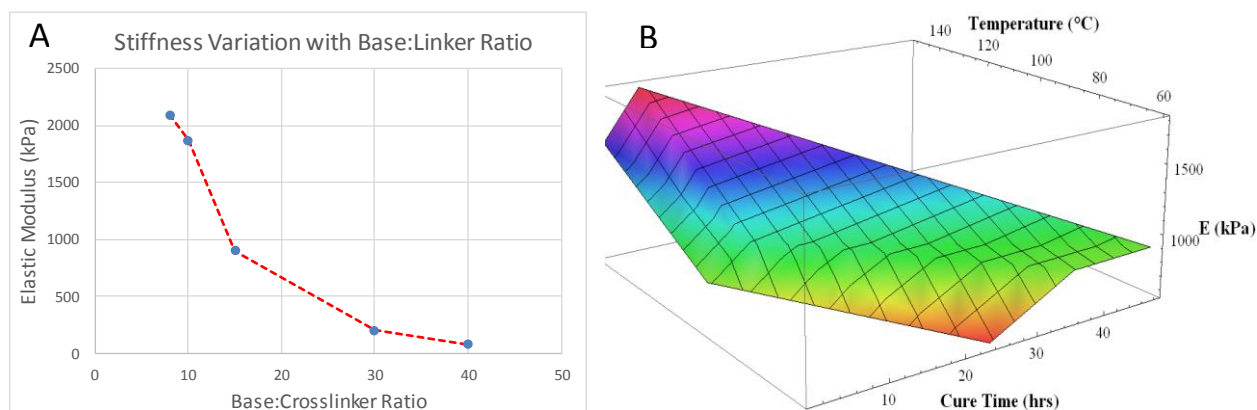
Figure 2.20: Tensile testing results. A) Elastic modulus of samples cured for 36 hours at 60°C with varying ratios of base:crosslinker. B) Elastic modulus of samples with varying curing conditions and fixed base:crosslinker ratio of 15.

The ratio of base to crosslinker has a more complex effect on the stiffness. The plot in Figure 2.20 shows variation for samples cured for 36 hours at 60°C. Increasing the amount of crosslinker generally increases the stiffness of the PDMS, but there are limits. Very low concentrations of the crosslinker yield sticky, semi-solid substrates that are not easily workable. A sample with 50:1 base to crosslinker lacked the integrity to be properly tensile tested. On the other end of the spectrum, very high concentrations of crosslinker yield exceedingly brittle samples. Ratios of 5:1 or below may fracture rather than stretch. Adding additional crosslinker beyond the suggested 10:1 also yields diminishing increases in the stiffness, especially when heating. The maximum tested elastic modulus was 3.1MPa for 8:1 PDMS cured for 6 hours at 150C, which was not much more than the 10:1 PDMS cured the same time with 3.0MPa modulus. At the lower end, the softest PDMS tested was 80kPa, giving a sizable range to work with.

2.3.2 Wavelength and Amplitude

The wavelength of the patterns can be easily measured using optical microscopy. One may directly measure the length per wave, typically averaged over several waves. A slightly more accurate method, averaging over the entire image, is to apply a Fourier transform and pick out the dominant frequency. This is preferred because the wavy patterns tend to have numerous 'dislocation defects' where one buckled wave merges into another. Any imperfection or non-uniformity in the strain field will result in local variations in the wavelength, so this value is best characterized by averaging over a large area. The fast Fourier transform (FFT) over a reasonable area tends to be consistent across the entire sample for uniaxially buckled samples.

An interesting application of this same concept is to perform the frequency transform optically, i.e. with laser light. The buckled pattern forms a diffraction grating, and the average wavelength can be directly calculated from the spacing between maxima in the diffraction pattern.

$$d \sin \theta = m\lambda$$

Where d is the wavelength of the pattern, λ is the wavelength of the light, and Θ is the spread angle from the pattern to the mth maximum in the diffraction pattern. This measurement technique allows fast determination of the wavelength and orientation of a pattern down to the wavelength of the laser source. Handheld blue (405nm) laser pointers are particularly useful for quick measurements and determining the orientation of patterns.

For the amplitude, AFM is perhaps the best way to measure micron-scale wavy patterns. The topography was characterized using an Asylum MFP-3D AFM in tapping mode. The AFM tips used were single beam, silicon cantilevers with resonant frequency of 325 kHz, and force constant of 40 N/m. The tip radius was 10 nm with a tip cone angle of 40 degrees (MikroMasch). Samples were scanned over an area of approximately 10 x 10 wavelengths squared, varying with the scale of the pattern, using 256x256 points. Two methods were used for extracting the amplitude from the AFM data. For copies of diffraction gratings, we can generally assume a consistent, sinusoidal pattern, so we may fit a function to the surface of the form:

$$z = A \sin\left(\frac{2\pi x}{\lambda_x} + \frac{2\pi y}{\lambda_y} + \phi\right)$$

There are 4 unknowns: A, λ_x, λ_y, ϕ. These are the amplitude, wavelength in x, wavelength in y, and phase. Wavelengths in both x and y are necessary because the sample is generally not perfectly aligned with the axes. Amplitude is then extracted directly. We can also accurately measure the pattern wavelength, which is $\sqrt{\lambda_x^2 + \lambda_y^2}$ due to the potential rotation of the pattern.

For buckled patterns, the sinusoidal fit is typically not reliable. The buckled pattern may have cracks, defects, variations in the wavelength, and distortions. Even if these are minor, it will ruin the fit with a sine wave. To account for this variation, a more generalized approach using an FFT is taken. Wavelength and wave orientation are readily calculated by finding the maximum in the FFT magnitude in both directions. The data is then rotated using bilinear interpolation so the waves are aligned with the axes of the image – this is also performed for display and presentation purposes. Outliers must be removed or the various imperfections described above could interfere with the amplitude measurement. Outliers are detected by generating an error image which is the difference between the original data and the filtered data after applying a frequency bandpass centered at the pattern wavelength. Data where the error exceeds twice the standard deviation of the error image is not used when calculating the amplitude. The amplitude is then calculated by finding the root-mean-square (RMS) and the mean absolute value (MAV) of the data and determining the amplitude of the sine wave that would give these values.

The difference between the amplitude calculated with RMS and the amplitude calculated with MAV (0 for a perfect sinusoid) gives an indication of the quality of the wave, reported in the pictures above as "accuracy". For good patterns, the difference will be <1% of the total amplitude, indicating a very close fit to a sine wave. We can also inspect pattern quality visually by looking at the side views in the AFM data displayed earlier in this section, which is a view of the surface looking along the axis of the wave. This view would ideally be a thin line, as the side projection of the sinusoidal pattern would be one-dimensional. The finite thickness indicates roughness, variation in the phase, or variation in amplitude.

2.4   Concluding Remarks

The process of producing wavy patterns with wavelengths <10μm and >150μm has been fairly well optimized; however, this leaves the region in between less well-covered. Wavy patterns in this intermediate range can be produced via sputtering, but the technique has been performed only several times and requires fine-tuning. Another method of expanding the range of wavy pattern scales would be to use other materials. PDMS is a very convenient material – well understood and readily available, but other, stiffer elastomers could be used for the substrate, such as latex rubber. Other materials can also be used to deposit a film aside from metal. Polystyrene has been used as the film layer (E ≈ 3GPa), deposited as a solution, to generate patterns with wavelengths below 100μm [55]. It is certainly possible to produce wavelengths at nearly any scale using this buckling technique, it is only a matter of acquiring the proper materials and making suitable devices to apply the strain.

Another area to explore is the mitigation of defects in the pattern. Researchers typically don't comment on the uniformity or quality of the buckled surface, although it is clear from our results that the pattern quality could be improved. The cracks forming along the axis of uniaxially strained specimens are due to the lateral contraction of the substrate from the Poisson effect. Subsequent release of strain puts the film under tension and causes fracture. This could be prevented by applying biaxial strain to counteract the lateral contraction during pre-strain. One way this can be done is to heat the sample during pre-strain or film deposition. PDMS has a very high thermal expansion coefficient, so lateral strains exceeding 5% can be negated by heating the sample within the working temperature range of the material. Efforts to accomplish this so far have been unsuccessful, but a renewed effort may prove fruitful. Eliminating the lateral stresses in the film may also help decrease dislocation defects and variation in the wavelength throughout the buckled surface.

3. Cell Response to Physical Features

Tissues in biological systems are formed by complex but highly organized cells. Extra-cellular cues that cause cells to organize themselves is a topic of tremendous importance. Among other factors, the *in vivo* environment of a cell includes a wide variety of mechanical signals, which may originate from the extracellular matrix or other cells. It is well known that cells respond to these mechanical signals by potentially altering many aspects of their behavior. This response is termed mechanotransduction. A better understanding of mechanotransduction will have an impact in fields ranging from developmental biology to tissue engineering.

A variety of techniques have been used to study mechanotransduction, one of which is to observe cellular responses to topographic features. Researchers have observed that cells will align when grown on grooved patterns spanning a wide range of sizes, but we still do not fully understand this phenomenon. For example, there is no accepted way to predict if a certain pattern will cause cells to align. A common observation is that either increasing the depth or decreasing the spacing of a grooved pattern will lead to better alignment, although this has generally not been formalized quantitatively. At least one attempt has been made to formulate an equation to predict alignment on grooved features by using automatic control theory [56], which led to the conclusion that the strength of the alignment signal is proportional to the square of the pattern aspect ratio, depth divided by pitch. This formulation is qualitatively in agreement with many observations, but it is not clear if it is generally applicable. In the context of very small patterns, other parameters such as the 'barrier size', defined as the square root of the product of pitch and width, are used to define a threshold for eliciting contact guidance [57]. Others have also observed effects deviating from a pure aspect ratio dependence for small features [58].

Compared to the great deal of data addressing alignment on sharp-edged grooves, there is very little data for edgeless features. Early studies of cells aligning on single fibers showed that curvature may have a direct effect on alignment, and these observations have been extended to ridge-like features by considering the bending of actin fibers in the lamellipodium [59]. A study comparing wavy and grooved features found that there was little difference in the response [60], although only two geometries were compared. Recently it has been shown that progressively rounding the edges of grooved features led to decreased stretching ratios compared to sharp-edged grooves of the same dimensions [61]. Cells are also known to respond to in-plane curvature, and it is believed the response is dependent on contractility [62]. It is still unclear how and to what extent substrate curvature affects cell alignment.
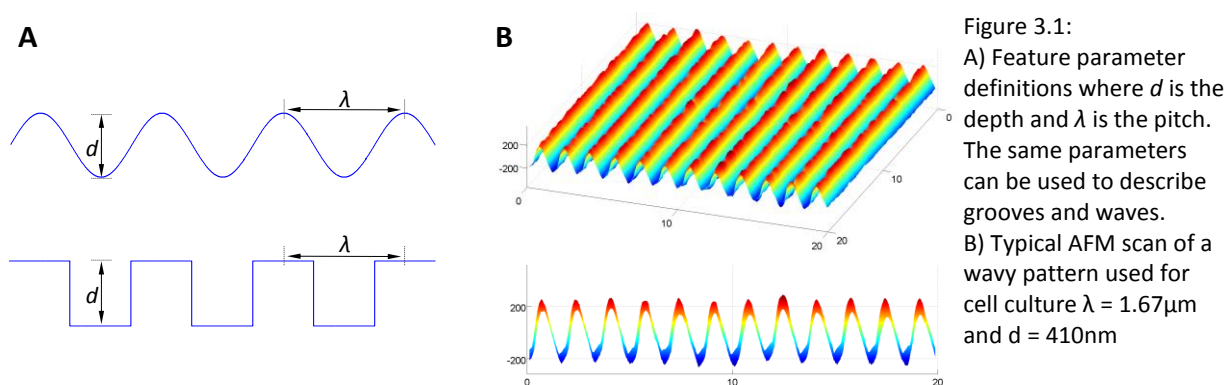
3.1   Reaction to Micro-scale Wavy Features

The non-lithographic techniques described in chapter 2 are employed to make approximately sinusoidal patterns with pitches in the micron and submicron range. The patterns are used to gain some additional insight into the general parameters that cells are sensitive to when aligning with anisotropic substrates. Time lapse imaging, along with a novel image processing technique, are used to quantitatively analyze both dense and sparse cell cultures. The quantitative characterization of cell alignment at different confluence levels helps establish the role of cell-cell interaction in the cell response to wavy patterns. We find a phenomenological parameter approximating a pattern's aligning potential that applies over a large range of length scales, for both grooved and wavy patterns. The data presented here also fill a gap in results for patterns without sharp edges that previously contained little comprehensive data from a single source.

3.1.1 Pattern Preparation

Samples were fabricated by replicating commercially available, holographic diffraction gratings (Edmund Optics) with a biocompatible material. We used Polydimethylsiloxane (PDMS) to produce the biocompatible replicas. Sylgard 184 PDMS was mixed at the standard base:crosslinker ratio of 10:1, poured on the grating surface, and degassed under vacuum for 30 minutes. The grating was then placed pattern-side-down on another, pre-cured slab of PDMS and cured at 60°C for 4 hours to bond the replica to the slab. The replica was then gently peeled away with the rest of the slab with minimum damage to the fragile diffraction grating.

To make samples of high optical quality, we performed an additional copying step to obtain the pattern as a thin film on cover glass. To do this, we silanized the PDMS replica by treating it with oxygen plasma (Diener Electronics) for 30 seconds at 100W and placing the replica in a sealed chamber containing tetrahydrooctyl(1,1,2,2)-tridecafluoro-dimethylchlorosiloxane (Gelest Labs) for at least 1 hour [60]. The silanization prevents PDMS from bonding to the replica. The replicating procedure described above was then repeated using a 25mm diameter coverslip. The silanized replica was easily peeled away from the coverslip, leaving an approximately 100μm thick layer of PDMS with a patterned surface on the coverslip. The coverslip was glued to the bottom of a culture dish before cell culture.

Wavy surface topography was characterized using an Asylum MFP-3D atomic force microscope (AFM) in tapping mode. The AFM tips used were single beam, silicon cantilevers with resonant frequency of 325 kHz, and force constant of 40 N/m. The tip radius was 10 nm with a tip cone angle of 40 degrees (MikroMasch). Samples were scanned over an area of approximately $100\mu m^2$ with 256x256 points. Two randomly chosen regions on the sample surface were scanned for each pattern, and the reported dimensions are the average of the two measurements. Pitch and depth were determined by fitting the data to a sinusoidal function. The pattern was compared to an ideal sinusoid and found to match well, except for some small scale roughness. The defining parameters of the patterns are taken to be pitch λ and depth d as shown in Figure 3.1A, and a typical AFM scan is given in Figure 3.1B.

Figure 3.1:
A) Feature parameter definitions where d is the depth and λ is the pitch. The same parameters can be used to describe grooves and waves.
B) Typical AFM scan of a wavy pattern used for cell culture λ = 1.67μm and d = 410nm

3.1.2 Cell Culture

To prepare the patterned PDMS for cell culture, the sample surface was treated with oxygen plasma for 30 seconds at 100W and then coated with an excess of 50μg/mL human fibronectin (BD Biosciences). This treatment was found to be the most effective surface modification for cell adhesion [63]. Patterns were allowed to incubate at room temperature for 1 hour, then rinsed 3 times with PBS and used immediately. C2C12 cells (ATCC) were cultured using Dulbecco's Modified Eagle Medium (DMEM, Life Technology) supplemented with 10% Fetal Bovine Serum (FBS, Hyclone) and 1% penicillin/streptomycin (BD Biosciences). Media was changed every 1-3 days as needed. C2C12 cells between passage 5 and 15 were used. Experiments consisted of seeding cells on the wavy patterns at a density of 1.0×10^4 cells/cm^2 and allowing them to grow to confluence (generally 2-4 days). For observation, cells were either kept in an incubator and imaged daily or grown in an environment-controlled chamber (37°C, 5% CO$_2$) on a phase contrast microscope (Olympus IX-51) for time lapse recording.

3.1.3 Image Analysis

To characterize cell responses two parameters, the confluence and the cell alignment, were measured quantitatively by analyzing still images and video frames taken during the experiments.

The confluence was measured as the percentage of the surface area covered by cells. The algorithm to measure confluence utilized a Sobel filter to find edges, roughly outlining cells, and then applied morphological dilation and erosion to recover the interior area of the cells. A local threshold was applied to binarize the image, and the reported confluence is the percentage of white pixels in the resulting binarized image. Confluence was found to be consistent between images obtained using the same microscope and magnification, which was the case for successive pictures in our time lapse sequences. This method is similar to the methods used by several other groups [64,65]. However, we have simplified the technique, foregoing an attempt to identify individual cells.

In order to quantify alignment as cells grow, we require an alignment metric that is consistent at different cell densities and can be applied to phase contrast images of live, unstained cells. Standard techniques to measure cell orientation involve fixing and staining cells so the shape of the cell [66,67], the nucleus [68,69] or the polarity of the Golgi apparatus [62,70] can be readily identified for individual cells. Alternatively, some researchers have identified cell major axes manually [52,63,71] or semi-automatically by converting images to binary [72,73] from phase-contrast images, which generally requires cells to be separate and easily distinguished from one another. In each case, statistical data is gathered by sampling many individual cells in the population. These methods are not feasible for our data because our cells are unfixed and unstained, and the cells are in close contact with each other. Additionally, any manual technique is subject to bias and human error.
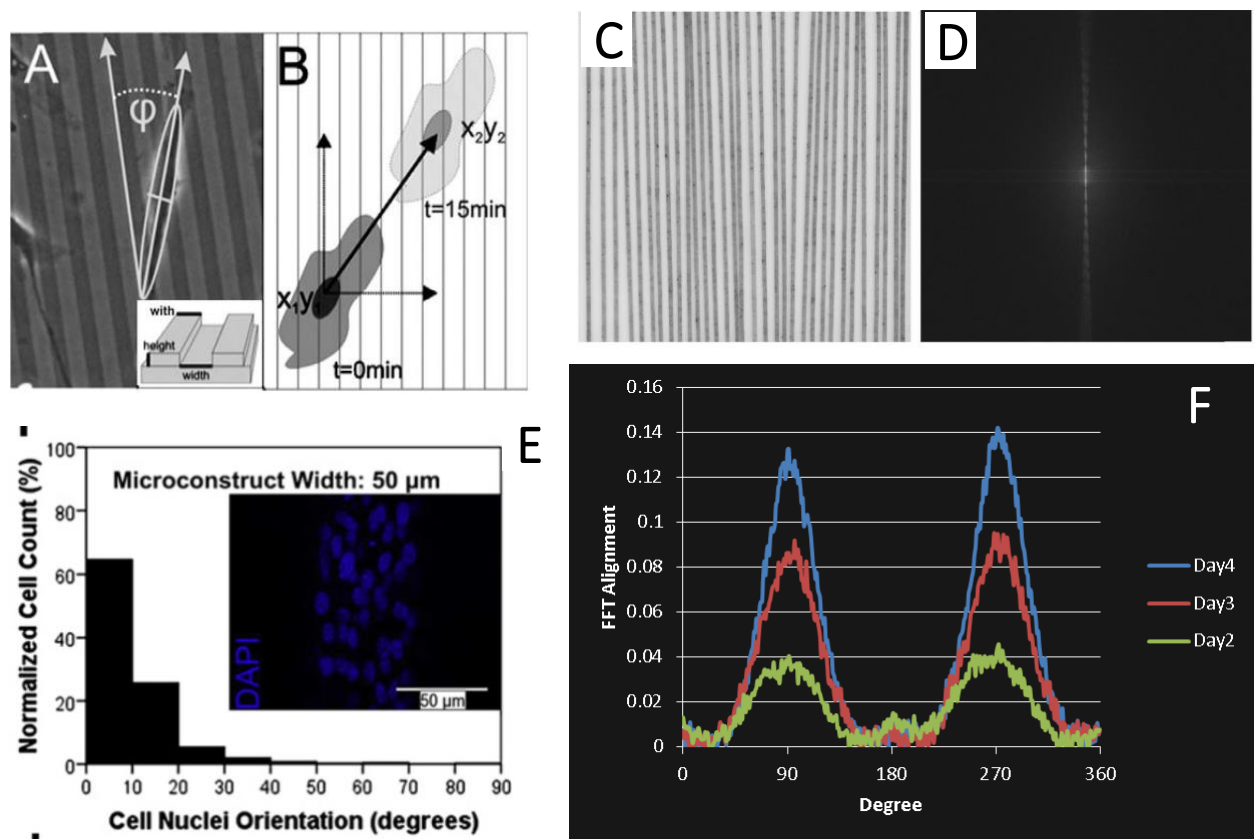
Figure 3.2: Alignment metrics. A,B) Manual selection of an ellipse bounding the cell. C,D) FFT with original image in C and transformed image in D. Intensity is summed along radial slices passing through the center of the image. E) DAPI stains the nucleus so the image is easily thresholded and an ellipse is automatically fit. F) Results from FFT method in C,D showing that the peaks increase with increasing confluence even though cell alignment is constant.

Frequency-based approaches have also been used to measure alignment, for example in fibrous samples. One example is a tutorial on how to quantify alignment by summing radial slices of a Fourier transformed image along different angles [74]. The method has been successfully applied for measuring alignment in dense cell cultures [75]. However, this approach is not consistent for different cell population densities, which we observe by noting that the peaks in the frequency spectrum increase as cells become confluent. Additional problems for frequency methods may arise when the pattern itself is visible. More flexible Gabor filters have been used to identify the local orientation in confluent cultures [76], but this approach does not specify how to quantify alignment of the whole culture. Figure 3.2 depicts how some of these alignment measurements work.

In order to render a single scalar parameter to characterize alignment for a wide range of cell densities, the images were analyzed using a robust, local frequency-based method, which calculated the image "energy" in a number of discrete directions summed over the entire image. Specifically, to measure cell alignment between 0 and 180°, we used 8 directions at increments of 22.5°. Every image was captured with the ridges of the wavy pattern running vertically, so the energy in the 0° direction could be used as an indication of alignment. The procedure was performed using the first three levels of the Gaussian image pyramid to account for potential changes in magnification or cell size. Normalization can be done in a number of ways. We chose to subtract the mean histogram value from the value in the vertical direction and divide by the peak value for a series of vertical lines. This gives an alignment value of 0 for random orientation and 1 for perfect alignment.

Figure 3.3: Example visual output from alignment and confluence algorithms. A,C,E) Sparse, unaligned cells, their area coverage in white (confluence), and the orientation energy histogram, respectively. The cells are found to be 44% confluent with alignment of 0.09. B,D,F) The same cells that have grown to confluence, their area coverage, and the orientation energy histogram, respectively. The cells are now 97% confluent with alignment of 0.61
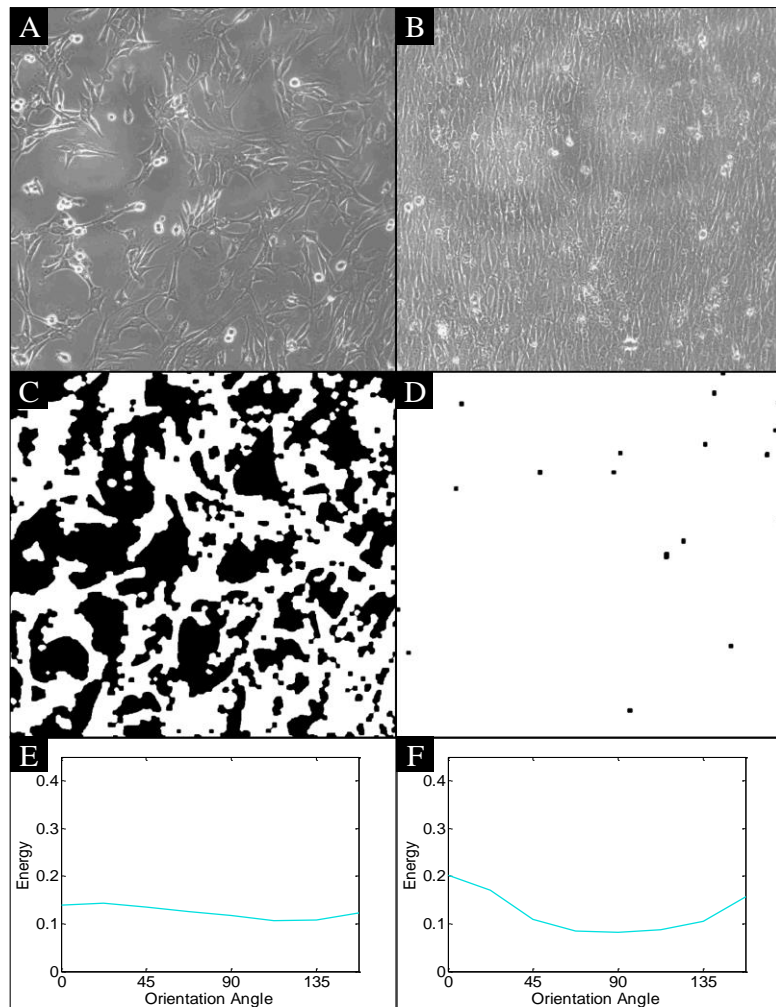
Figure 3.3 shows the visual output from the confluence and alignment algorithms for two example images with low and high confluence cells. The binarized images show the area covered by the cells and the plots show the spectral energy histogram from the alignment measurement. This demonstrates that the method described here provides a consistent measurement of cell alignment for a wide range of cell distributions. Additional characterization of the alignment algorithm demonstrating the invariance to changes in cell density and contrast is given in Figure 3.4 where a number of test images have been generated with varying contrast, spacing, and alignment. The Matlab script performing the confluence and alignment measurements is available in the Appendix Figure 6.3 along with additional example images showing the measured values in Appendix Figure 6.4.
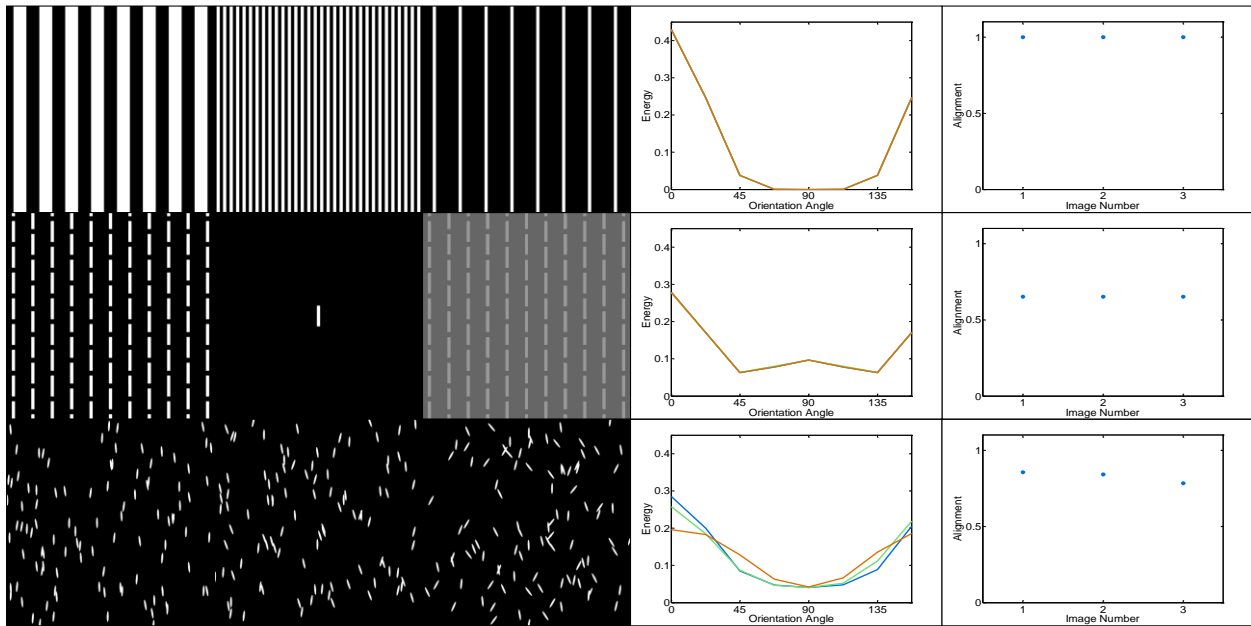
Figure 3.4: Verification of alignment algorithm. Each row contains three images that were analyzed, then the histogram of energy by orientation (one curve per image), and then the average alignment (one value per image). The first row demonstrates invariance to scale and frequency. The second row demonstrates invariance to number of objects and contrast. The third row demonstrates that reduced alignment in a simulated population reduces the output value of the algorithm.

3.1.4 Response to Feature Size

We conducted a systematic study of cell responses to patterned surfaces by culturing C2C12 cells on surfaces with a range of different pattern sizes. Three distinct responses were observed. (i) On the large patterns tested, cells immediately and strongly align with the wavy pattern. Frames from the time lapse video M1 in the Appendix Figure 6.5 show cell behavior on a wavy surface with $\lambda = 1670$ nm and $d = 410$

nm over 42 hours. A high degree of cell alignment in this video is clearly visible and confirmed by the values measured with our alignment algorithm. Such cell behavior is in agreement with observations by other researchers for features of similar size and geometry [71,73,77]. (ii) On the very small patterns tested, cells do not show any global alignment, and cell behavior is indistinguishable from that of cells grown on flat, control surfaces. This is shown in frames from video M2 in Figure 3.5, an experiment on a wavy surface with λ = 420nm and d = 24nm over 72 hours. This result is also in agreement with previous studies defining a limit for sensitivity to patterns [53,67]. (iii) Within a range of intermediate pattern sizes, the cells are initially randomly oriented, but undergo a transition to alignment as the cell population becomes confluent. This phenomena is discussed in detail in the following section.

Figure 3.5: Select frames from a time lapse sequence on a pattern with λ = 830nm and d = 100nm. Alignment increases as cell density increases. Cells were seeded at an initial density of 1.0×10^4 cells/cm^2 and imaged over the course of 4 days. Grooves run vertically in all images. Scale bare is 200µm
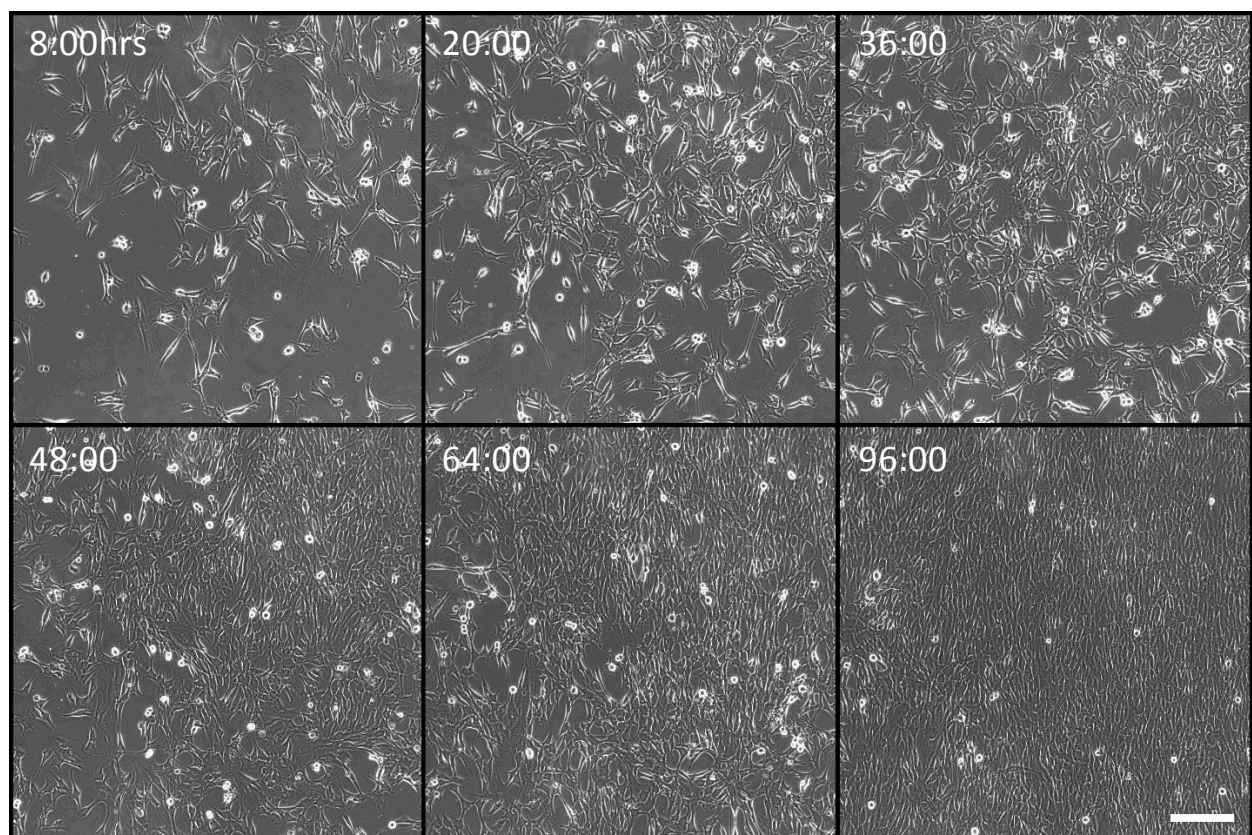
3.1.5 Response to Confluence and Cell-Cell Interaction

For patterns of intermediate size that do not immediately align, we observe an interesting dependence of alignment on the confluence of the cell population. For certain patterns, cells that do not align as sparsely-seeded individuals may begin to align as the population increases and cells interact with one another. The phenomenon is most striking when viewed in a time lapse movie, for example Figure 3.5 shows select frames in a time lapse sequence for a pattern with 420nm pitch and 52nm depth, demonstrating the typical alignment on an intermediate-sized pattern. The trend can be captured quantitatively by using the previously discussed image analysis algorithms to measure alignment and confluence. Alignment data from three time lapse recordings showing three distinct types of alignment behavior are given in Figure 3.6 as a function of time and confluence. Immediately aligning and non-aligning cells show nearly constant alignment values as the culture grows from very sparse (<15% confluent) to very dense (nearly 100% confluent), while the cell cultures exhibiting delayed alignment tend to show a relatively sharp transition from low to high alignment at high confluence. From the data and visual observations, it is clear the effect of confluence on alignment is non-linear, and the transition

Figure 3.6: Normalized alignment and confluence data from three separate time lapse video sequences. Each sequence shows a distinct trend. Blue squares: very small pattern, no alignment. Red circles: Large pattern, alignment is immediate and mostly constant. Green triangles: Medium pattern, alignment increases sharply as cells become confluent.
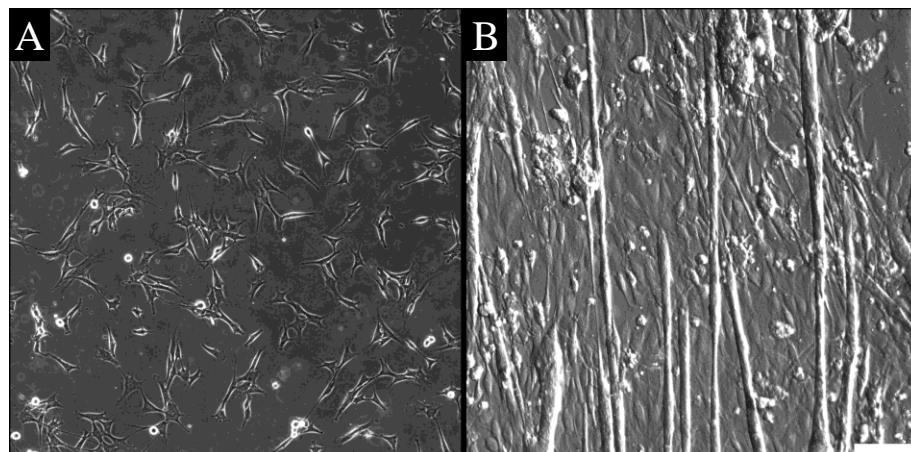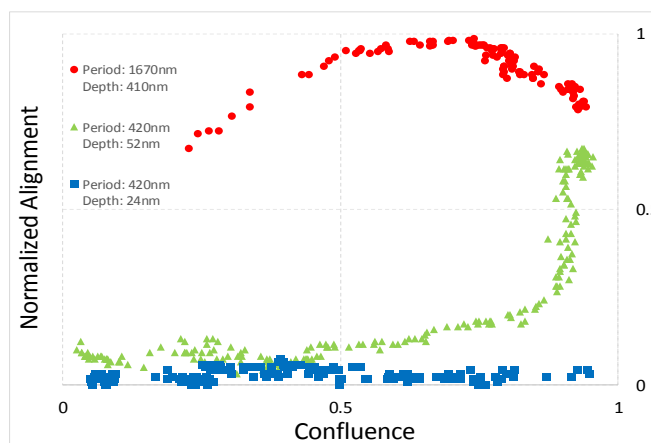

Figure 3.7: A) Unaligned cells after 1 day on a pattern with λ = 420nm and d = 52nm. B) The same cells after growing to confluence and culturing in differentiation media for 7 days. The resulting myotubes align even though the individual myoblasts do not align until they become confluent. Scale bar is 200μm.

in alignment appears to be most dramatic after cells have reached approximately 70% confluence. Interestingly, cultures that exhibit delayed alignment are nearly indistinguishable from cultures that immediately align once both are confluent. Either pathway to alignment will also lead to well-aligned myotubes after differentiation is induced in cultures of C2C12 myoblasts, Figure 3.7.

The dimensions of all patterns examined in this study are given in Table 3.1 along with a summary of the alignment results from the various patterns. We observe a distinct cutoff at an alignment value of 0.3 that separates cultures that do not visibly align from cultures that do align to some degree. Using this cutoff, cultures were categorized in a binary fashion as either aligned or unaligned in Table 3.1 by bolding the alignment value for aligned cells. Table 3.1 also includes several geometric parameters that have or could be used to quantitatively characterize the patterns. Each parameter is defined in terms of the pitch and depth of the pattern, where size is λd, aspect ratio is d/λ, and effective curvature is d/λ^2. The effective curvature is proportional to the maximum curvature of a sinusoidal wave. Additionally, a parameter of our own definition, Φ, is listed, which we refer to as the sensitivity parameter. The relation of these parameters to cell alignment and the merit of the sensitivity parameter are addressed in the following sections.

As shown in Figure 3.6, when the surface waviness is very large, sparsely distributed cells align with the patterns immediately upon seeding, whereas when the waviness is very small, cells do not align with patterns at all. For patterns within a range of intermediate dimensions, cells align with the patterns as they become confluent, an emergent phenomenon of high density cell populations. Although alignment increases with time as well as confluence, we find that confluence is the determining factor based on the observation that alignment on a single pattern varies within a culture in relation to the local cell density. This phenomenon can be seen in the individual frames of the time lapse sequence in Figure 3.5, and has been indicated on the two images in Figure 3.8. These observations agree with prior work indicating that C2C12 and 3T3 fibroblasts tend to reach maximal alignment within 24 hours [66]. Our time lapse data typically span several days, which suggests that delayed cell alignment is not a consequence of increasing exposure time on the patterns.
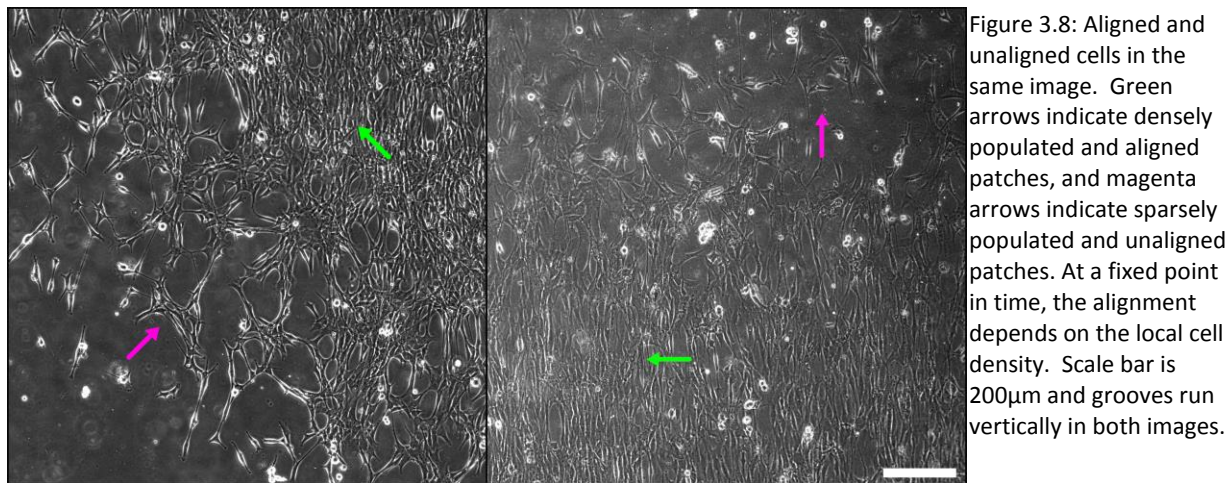
Alignment Data Summary

λ (nm)	d (nm)	Size (nm^2)	Aspect Ratio	Effective Curvature (nm^{-1})	Individual Alignment	Confluent Alignment	φ
280	8	2.24E+03	2.86E-02	1.02E-04	0.00	0.01	6.78E-04
420	24	1.01E+04	5.71E-02	1.36E-04	0.09	0.02	1.49E-03
560	24	1.34E+04	4.29E-02	7.65E-05	0.10	**0.48**	1.59E-03
420	33	1.39E+04	7.86E-02	1.87E-04	0.11	**0.49**	1.80E-03
560	40	2.24E+04	7.14E-02	1.28E-04	0.23	**0.53**	2.21E-03
420	52	2.18E+04	1.24E-01	2.95E-04	0.04	**0.71**	2.33E-03
830	62	5.15E+04	7.47E-02	9.00E-05	0.08	**0.36**	3.19E-03
560	91	5.10E+04	1.63E-01	2.90E-04	0.00	**0.35**	3.56E-03
830	85	7.06E+04	1.02E-01	1.23E-04	**0.30**	**0.76**	3.90E-03
830	100	8.30E+04	1.20E-01	1.45E-04	0.00	**0.56**	4.31E-03
830	200	1.66E+05	2.41E-01	2.90E-04	0.11	**0.70**	6.42E-03
1000	190	1.90E+05	1.90E-01	1.90E-04	**0.44**	**0.94**	6.68E-03
1670	220	3.67E+05	1.32E-01	7.89E-05	**0.37**	**0.62**	8.34E-03
2000	240	4.80E+05	1.20E-01	6.00E-05	**0.31**	**0.94**	9.04E-03
1670	410	6.85E+05	2.46E-01	1.47E-04	**0.41**	**0.93**	1.24E-02
1670	440	7.35E+05	2.63E-01	1.58E-04	**0.98**	**0.99**	1.29E-02
2000	450	9.00E+05	2.25E-01	1.13E-04	**0.80**	**0.82**	1.38E-02

Table 3.1: List of each sample tested with several different parameters describing each pattern. The threshold for alignment is taken to be 0.3 using our normalized alignment measure, and values above this threshold have been bolded. The column φ is the parameter we propose to describe the sensitivity of cells to periodic pattern. The list is sorted by φ, which shows there is a clear alignment threshold at 0.006 for individual cells, and at 0.002 for confluent groups.

What distinguishes confluent and sparsely distributed cell populations is the presence of cell-cell interaction. Cell-cell interaction has been shown to have a strong effect on cell behavior that may even override signaling from the ECM [78]. Cell-cell interaction has also been shown to play a role in cell alignment. It is well known that polarized cells tend to locally align with one another when in contact, and it has been suggested that the mechanism causing this mutual alignment is contact inhibition occurring when the lamellipodia touch [79]. The interaction of mutually aligning objects has also been studied using integro-differential equations [76,80,81]. This mathematical approach lends some insight into how global alignment may arise from local interactions. The critical parameters determining the stability of local or global alignment were found to be the rate at which cells move in culture, their rate

of mutual alignment, and the likelihood that neighbors will mutually align [76]. Mathematical analysis of global alignment in the presence of a patterned bias is lacking, however, and experimental results are not in agreement. In some cases, cells have been found to lose their alignment as they become confluent [52], including myoblasts [73]. Other reports show that adherent cells become more aligned as they interact. For example, fibroblasts have been shown to become more sensitive to patterned substrates when they become confluent [71]. Our data strongly support this latter case and the mathematical models showing that cell-cell interaction will enhance alignment of high density cell populations on surface patterns.

Figure 3.8: Aligned and unaligned cells in the same image. Green arrows indicate densely populated and aligned patches, and magenta arrows indicate sparsely populated and unaligned patches. At a fixed point in time, the alignment depends on the local cell density. Scale bar is 200μm and grooves run vertically in both images.

3.1.6 Sensitivity Parameter

Several efforts have been made to identify the cues controlling cell alignment. Researchers have suggested that the aligning potential of a periodic pattern can be described as proportional to the groove depth [82] or inversely proportional to the periodicity [77]. Other groups have suggested parameters combining periodicity and depth such as the aspect ratio [56], barrier size [57], or fitting regressions [72,83]. Attempts have also been made to relate possible mechanisms for alignment to a parameter of the pattern. A geometric model based on the assumption of a solid nucleus and maximizing contact area was used to correctly predict how cells would align on patterns of posts [84]. Early work on fibroblast alignment led to a hypothesis that alignment is the result of the high bending stiffness of actin filaments, which was observed when cells failed to cross a slanted ridge when it was sharper than a critical angle [59]. The effect of actin bending stiffness might also be related to the curvature of the pattern. Most

research to date has focused on patterns with sharp edges and features fabricated with lithography, so the influence of curvature cannot be accounted for. Recently, it was shown that the curvature of the edges of periodic grooves can indeed affect alignment within a certain range of dimensions [61].
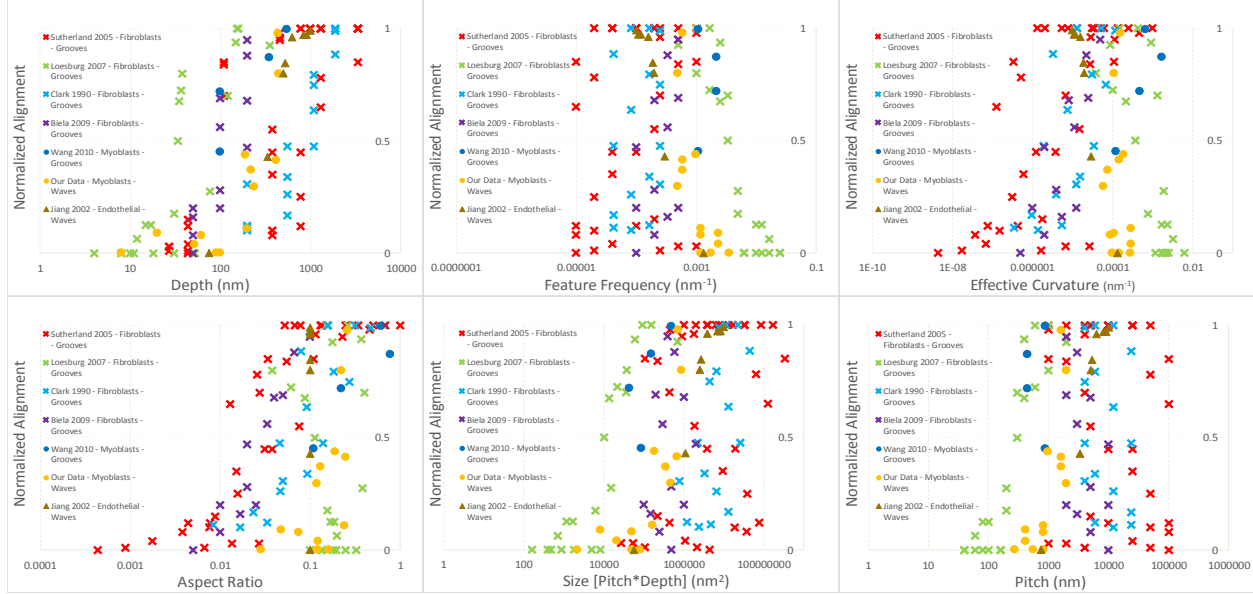

Figure 3.9: Alignment data from a number of different groups and cell types [60,67,71,77,82,83] plotted against various parameters characterizing periodic features. Data was collected from tables and figures from prior work characterizing alignment on periodic features, and original alignment measures were linearly rescaled between 0 and 1. A valid phenomenological pattern should capture all the data as a single curve, and alignment should increase monotonically as the parameter increases. Such a trend is not observed for these parameters.

None of these models, however, has been rigorously verified, and the assumptions for each model are not alike. In order to check if any previously defined parameter could generally describe alignment over a large range of length scales, we plotted our data along with data from several other research groups against these parameters. Figure 3.9 compares normalized alignment data from several groups against a number of parameters. It is clear that no obvious pattern is observed when the normalized alignment is plotted against any of these parameters. We expect a successful generalized parameter to represent all the alignment data as a single, sigmoidal curve where low values give no alignment and high values give maximal alignment. The results clearly show that none of these parameters can accurately capture the experimental trend in such a way.

Thus we attempt to define a phenomenological parameter to describe cell behavior on generalized anisotropic patterns for a variety of cell types. Based on our results in Table 3.1, we find that cells tend to align more readily with surface features when d and λ are large. If either of these parameters is very small, cells tend not to respond to the features. Additionally, we expect that when the pitch is very large

relative to the depth, the cells will not sense the features. This can be described by the curvature of the substrate, or more specifically, an effective curvature which we take to be proportional to the maximum curvature for sinusoidal patterns. The relevance of such a term may relate to the bending stiffness of actin filaments as previously described.

To maintain generality, all of these dimensional features should be compared to a length scale relevant to the dimension of a cell, *L*, which is on the order of tens of microns. With these asymptotic conditions in mind and considering that cells may respond to any or all of pitch, depth and curvature, we propose the following non-dimensional parameter, *Φ*, to characterize the sensitivity of cells to a periodic, anisotropic pattern:

$$\phi = \frac{\sqrt{\lambda\,d}}{L+\kappa^{-1}}$$

The numerator is related to the previously described barrier size and increases as either pitch or depth increase. The denominator is related to the inverse of the relevant curvature, κ, of the substrate, or the effective radius of curvature, compared to the length of the cell. For a fixed *d*, as λ becomes increasingly large, the curvature term in the denominator begins to dominate, which reflects the fact that the surface appears locally flat to an individual cell when curvature is low.

3.1.7 Parameter Application

 Figure 3.10 shows the normalized alignment plotted against the sensitivity parameter ϕ from measurements by us and several other groups on a few different cell types. In Figure 3.10A a single cell length dimension *L* = 60µm is used to non-dimensionalize the feature lengths for all data obtained by different groups. Unlike the poor correlations between cell alignment and other feature parameters shown in Figure 3.9, Figure 3.10 shows a clear transition where cell behavior changes from non-alignment to alignment as the values of ϕ increase over a range of a decade (note the log scale for the horizontal axis). It may be further argued that, since each experiment uses a different cell line with different culture conditions and measurements, the behavior should be characterized using a different *L* for each experiment. The result given by varying *L* is shown in Figure 3.10B, which shows that the

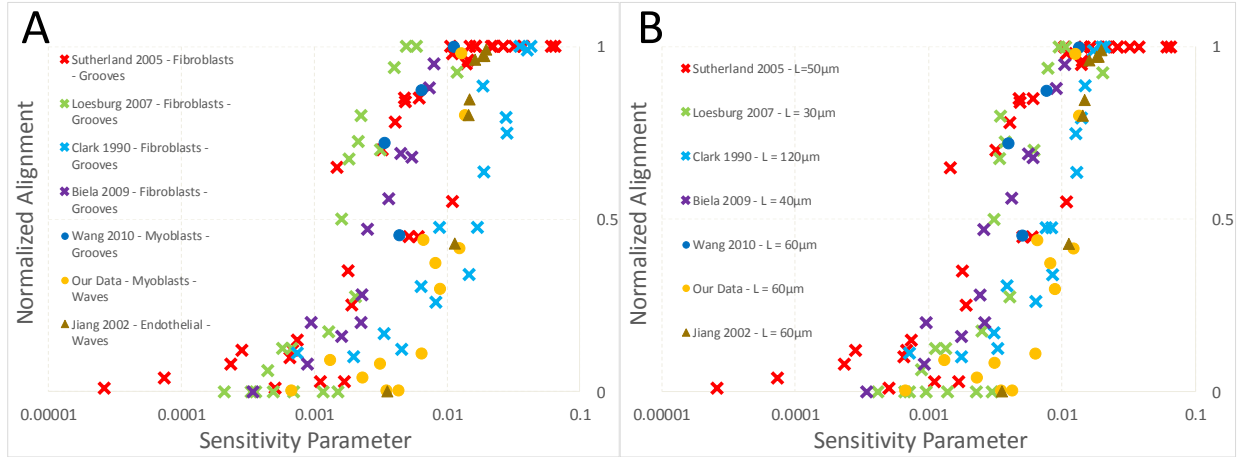transition behaviors of cell alignment from many prior studies collapse onto a single sigmoidal shape when plotted against ϕ.

Figure 3.10: Alignment data from a number of different groups and cell types [60,67,71,77,82,83] plotted against ϕ. Data was collected from tables and figures from prior work characterizing alignment on periodic features, and original alignment measures were linearly rescaled between 0 and 1. A) Plot with the normalizing length scale fixed at 60μm. Individual data sets tend to follow a sigmoidal trend. B) Allowing the normalizing length to vary between different data sets leads to collapse of the data towards a single curve. Some variability is present due to differing conditions and alignment metrics.

Using our experimental results for sparsely distributed and confluent cells, the correlation between cell behavior and the sensitivity parameter reveals additional features. Figure 3.11 compares our data for many experiments plotting individual and confluent cell alignment against ϕ. The blue triangles represent the alignment measurement for sparsely distributed cells, whereas the red circles at the same value of ϕ represent the corresponding alignment measurements for confluent cells. The figure demonstrates that two critical values of the sensitivity parameter exist, ϕ_{c1} and ϕ_{c2}. For surface patterns with a sensitivity parameter smaller than ϕ_{c1}, cells do not align with the patterns regardless of the confluence. For a sensitivity parameter larger than ϕ_{c2}, even sparsely distributed individual cells align with the patterns. For surfaces between ϕ_{c1} and ϕ_{c2}, individual cells do not align with the patterns, but confluent cells do. This trend is also clear in Table I, where the data are arranged in ascending order of the value of the sensitivity parameter. Taking L to be 60μm, the thresholds are approximately 0.0015 and 0.0065, respectively.

The current results are particularly relevant in the context of muscle tissue engineering. It has been shown that myoblast alignment is a critical step in the formation of functional muscle [85], and myoblasts

are typically grown to or near confluence before differentiating into myotubes. However, most studies on myoblast alignment specifically look at individual cells that are not in contact with other cells, and there is relatively little quantitative data on how anisotropic geometry and cell-cell interaction together influence myoblast alignment. Some research has partially addressed this issue by looking at cell seeding density as a variable in muscle formation protocol [30]. Yet a deeper understanding of how cell-cell interaction can affect and improve myoblast alignment is lacking. Our observation that confluent cultures align with smaller patterns than individual cells means that researchers can use smaller patterns to achieve useful muscle alignment. This could be useful in applications where micro-scale mechanics are important, such as the building of cellular machines [86].
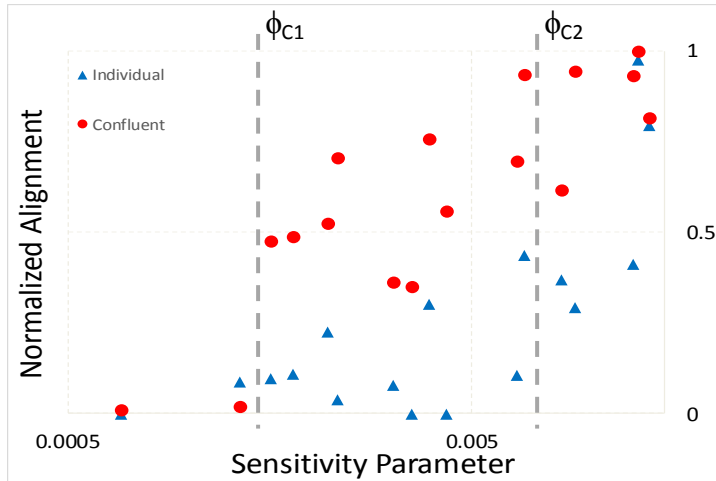
Figure 3.11: Our data comparing individual and group alignment where individual alignment is assessed at <25% confluence and confluent alignment is assessed at >90% confluence for the same pattern. ϕ_{C1} is the threshold at which confluent cells will align ($\approx$.002), and ϕ_{C2} is the threshold at which individual cells will align ($\approx$.006). The normalizing length scale is 60μm

3.1.8 Conclusion

Despite a large body of research, questions remain regarding the fundamental mechanics of such responses. Our results suggest that cells are sensitive to pitch, depth, and curvature of periodic, anisotropic patterns at the micron scale, and we propose a non-dimensional parameter that may predict the tendency for cells to align on a pattern based on these sensitivities. We identify thresholds for the parameter that separate patterns that will align cells from patterns that will not for individual and confluent cells. Additionally, between these thresholds we observe that confluence significantly affects alignment, and we conclude that cell-cell interaction may enhance alignment in the presence of weak topographic cues. We still do not fully understand the mechanisms by which cells respond to their mechanical environment. Further work may be done to better explain why cells respond to the pattern features investigated here, and how cell-cell interaction can lead to changes in cell alignment.

3.2   Cells in Gels and 3D Geometry

Although topographically patterned, cells interact with nano-scale wavy patterns as a 2D surface. Recently, the cell biology community has placed increasing focus on the more relevant 3D world in which cells normally inhabit. We now know that cells will look and behave very differently in 3D than when cultured on a flat surface [87]. Additionally, the 3D environment may be much softer than rigid PDMS patterns previously addressed. 3D cell environments may consist of a hydrogel containing ECM proteins, fibrils, and other cells, all contributing to the mechanical cues experienced by the cells. In this section an unusual observation of cell behavior spawns a series of experiments, which are analyzed using tools from mechanics.

3.2.1 Mammary Epithelial Cells

One outstanding mystery related to cell mechanics in a 3D environment is the observation that epithelial cells appear to behave differently near edges of small culture containers when grown on a soft hydrogel. Specifically, when culturing mammary epithelial cells, such as MCF10a, on top of a layer of Matrigel, cells will tend to form ductal structures in a region in the shape of an annulus near, but not quite at the edge of the container [88]. This is in contrast to the acinar morphology observed elsewhere in the culture, including the center area as well as the region high on the meniscus, very close to the walls of the container. There is no intentional biochemical cue to drive this behavior, so a mechanical explanation is sought instead. Better understanding of this behavior may be of interest to biologists studying epithelial cells wondering why cells form tubes in their culture, but we might also gain more general insight into how cells organize into these ductal formations.
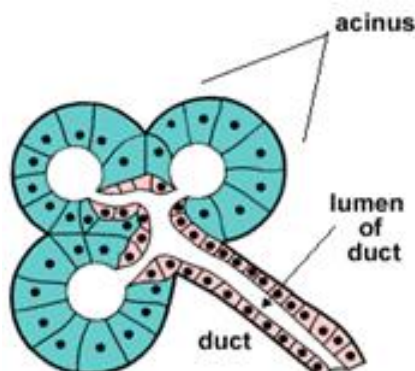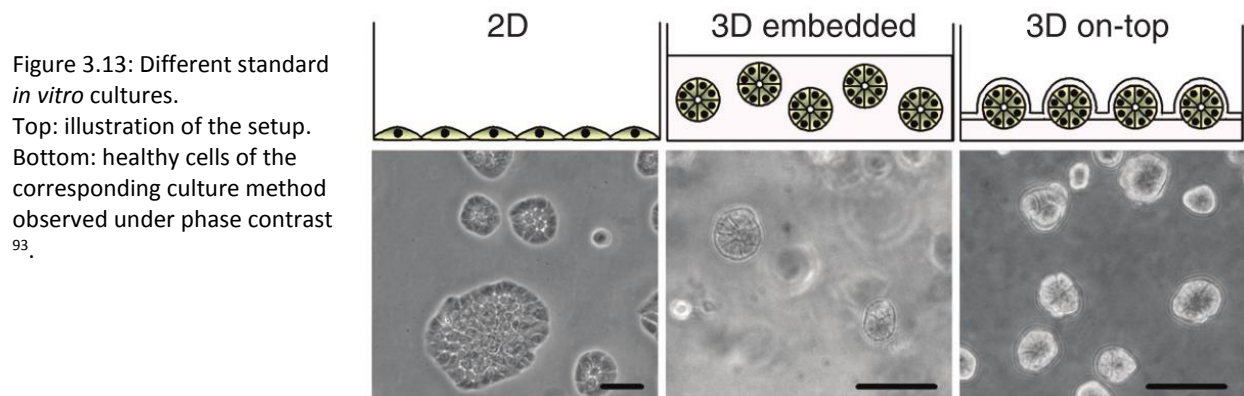

Figure 3.12: Structure of epithelial cell formations in breast tissue [88].

The epithelial cells studied here include MCF10a, an immortalized cell line derived from human breast epithelium as well as HME496, which are a line of primary mammary epithelial cells provided by Dr. Susan Clare at Indiana University. In vivo, these cells take on a branched tubular structure terminating in round acini [89]. The acini are hollow spheroids formed by a single-layered shell of cells, and both the acini and ducts have a distinct lumen in healthy tissue. Figure 3.12 shows a simplified graphic of the structure. The environment surrounding these cells in vivo is primarily composed of collagen I, which has a fibrous structure. The cells grow on sheets of basement membrane primarily composed of collagen IV and laminin, which forms a mesh-like morphology. The elastic modulus of this environment is on the order of 150Pa-200Pa in healthy tissue, although it is well known to be stiffer in cancerous tissue [90]. Such tissue is often simplified as isotropic and linear elastic for simulation [91], but it should be remembered that the material is actually viscoelastic and very anisotropic as cells reorganize the ECM around them. Most breast cancers originate from the ductal structures in the breast [92], so understanding the nature of duct formation in this environment is particularly important for cancer research as well as developmental biology.

Figure 3.13: Different standard *in vitro* cultures.
Top: illustration of the setup.
Bottom: healthy cells of the corresponding culture method observed under phase contrast [93].

In vitro, these same acini and ducts may self-assemble from a uniform seeding of individual cells in an environment similar to that described above. All of the experiments described in this section are based on the so-called "3D on-top" protocol, where a layer of gel is deposited and solidified before adding cells, and additional gel is included in the media during culture [93]. Cells will tend to migrate into the gel to some degree creating an effective 3D environment with most of the cells in the same plane for easy viewing with phase contrast optics. The gel suggested for this protocol is Matrigel (BD Biosciences,

growth-factor-reduced, phenol-red-free), which is a liquid at 4°C but solidifies rapidly at room temperature. To use this gel to make a reproducible 3D construct, the gel, pipet tips, and container for the gel need to be chilled on ice prior to and during dispensing the gel. The gel composition is not explicitly specified – it is extracted from Engelbreth-Holm-Swarm mouse sarcoma cells and varies from lot to lot. Results are best compared using the same batch of gel when possible. Matrigel is a mimic for the basement membrane in vivo and consists mostly of collagen IV and laminin as well as entactin.

The Matrigel may be modified by changing the concentration or adding additional factors. One addition common to several experiments is type I collagen (BD Biosciences – rat tail), which provides a fibrous element that the cells may organize, making it more like native ECM. Collagen I for gel formation should come qualified for this purpose by the manufacturer. Whether used alone or added to Matrigel, it must be neutralized to 7-8pH for it to solidify, which is done with concentrated NaOH. Collagen I is also chilled before use and allowed to gel for at least an hour in an incubator to ensure reproducible structure.

3.2.2 Gel Meniscus

Samples for meniscus measurement were generously prepared and donated by Yvonne Ziegler from Professor Anne Nardulli's lab at the University of Illinois. These samples were produced following a variant of the 3D-on-top procedure where a fixed amount of Matrigel was deposited in a standardized manner. Importantly, the culture container is square in shape with a side length of 11mm. Samples were either plated with MCF10a cells or MCF10a cells co-cultured with reduction mammoplasty fibroblasts (RMF). The addition of fibroblasts greatly enhances the formation of tubular constructs, although these structures form in the same region whether or not fibroblasts are present [88]. Figure 3.14 shows a well-developed culture prepared with fibroblasts to highlight the common features of these cultures and the problem at hand. This image and the following images were taken at 6 days after seeding and 5 days after seeding, respectively, using differential interference contrast (DIC) on an Olympus IX-81 upright microscope.
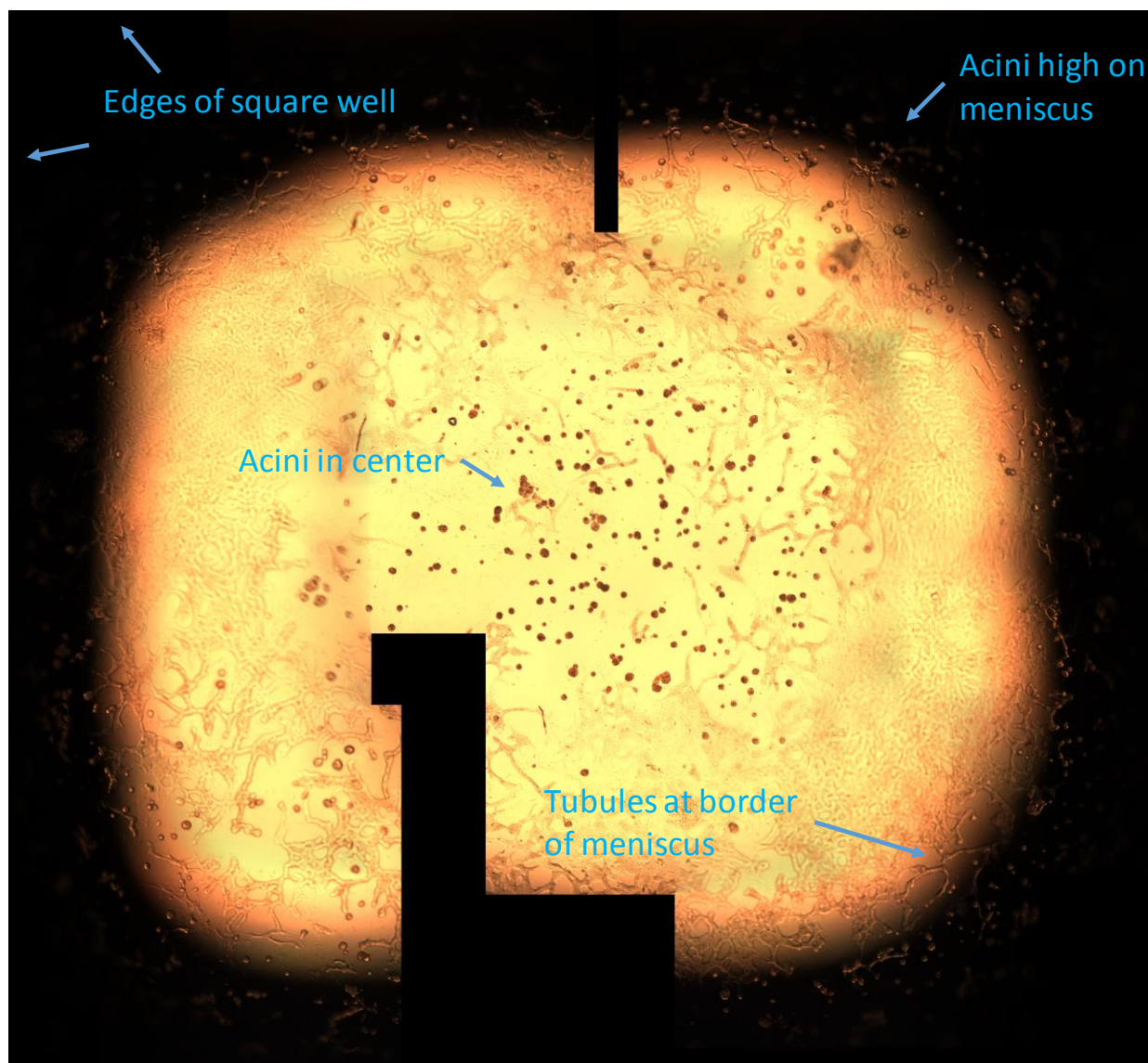
Figure 3.14: Co-culture of RMF and MCF10a displaying typical response to the meniscus. The entire image is 11mm by 11mm comprising the entire square culture well. Day 6 after plating.

We are interested in quantifying the locations of tube formations in relation to the surface geometry. The highly branched sample in Figure 3.14 is quite difficult to analyze, so a less-developed sample without fibroblasts was used for measuring the topography, Figure 3.15. The method used to measure the topography was a 'best-in-focus' technique where a microscope with a motorized stage having 1μm resolution in the X- and Y-axes, and 0.1μm resolution in the Z direction was moved to bring points on the surface into focus. The sample was clamped to the stage and drained of media to minimize optical distortion at the liquid-air interface. The stage was then maneuvered to focus on points at the center of the field of view, and the location of the stage at each focused point was recorded. The gel surface itself

is generally transparent, so the points were recorded where acini were present at the location where the topmost portion of the spheroid was in focus. The uncertainty in the best-focused location was typically ~10μm while the total variation in the surface height was ~1mm. We are interested in height relative to the bottom of the well, and the acini form very near the surface. Thus, this measurement was a reasonable estimate of the geometry the cells interact with. Note that this best-focus optical method requires an object that can be brought into focus, so the bare, curved regions very close to the walls of the square well were not measurable.
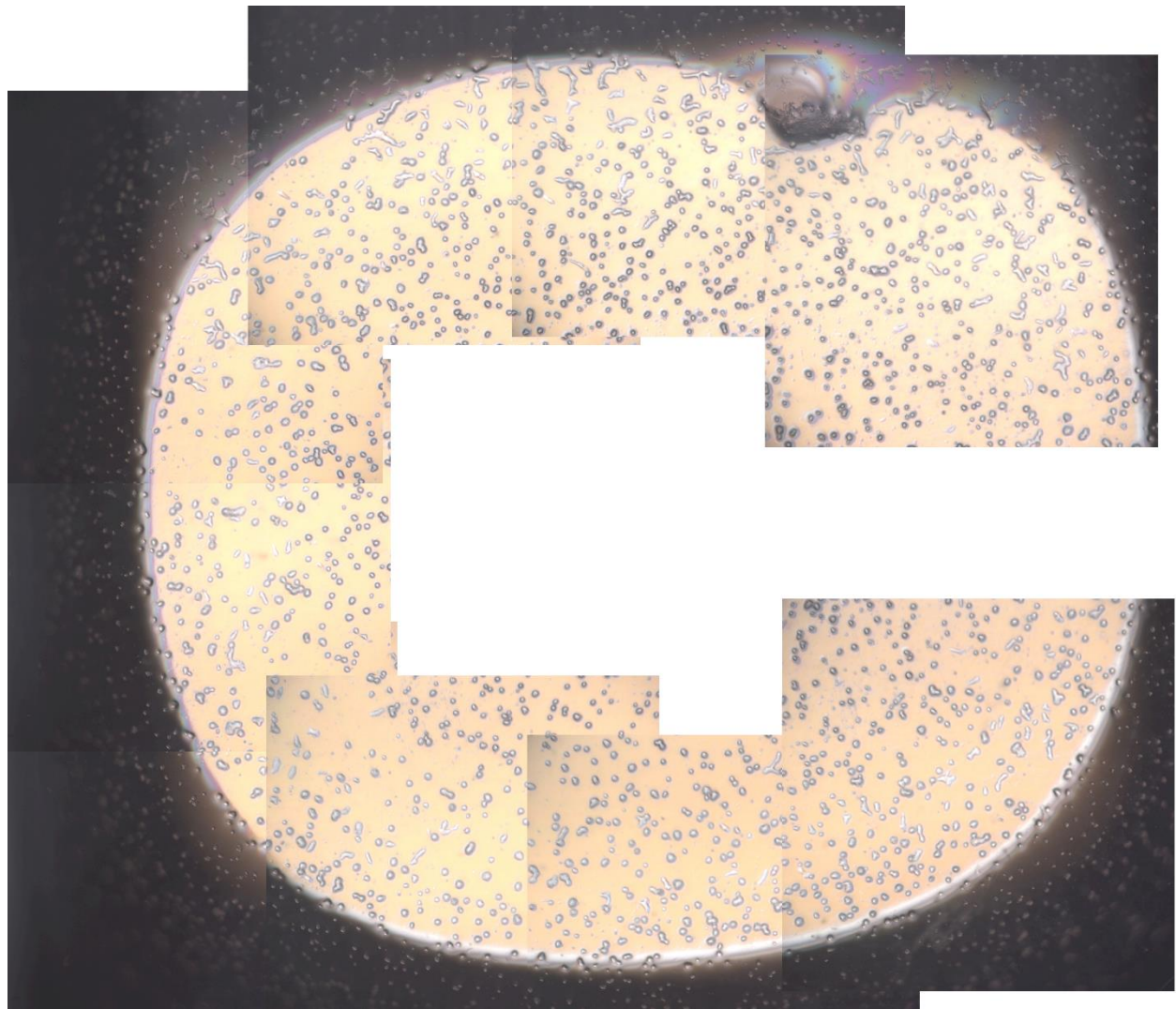
Figure 3.15: MCF10a cell culture used for surface measurements. Day 5 after plating.

Several hundred points were recorded from each gel sample, and the surface was plotted using the "ListPointPlot3D" function in Mathematica with the option of visibly smoothing the overlaid mesh applied. The actual data points are also plotted as small black dots to show the sampled locations on

the surface. An example of the surface that is generated by this method – from the same sample as in Figure 3.15 – is given in Figure 3.16. The surface as plotted has the lowest point at the surface of the gel set to 0 height. After measuring points on the surface, the gel was removed from the well so the bottom of the plate could be imaged – this gave the depth of the gel which was ~200µm at its thinnest point in the center of this particular sample.
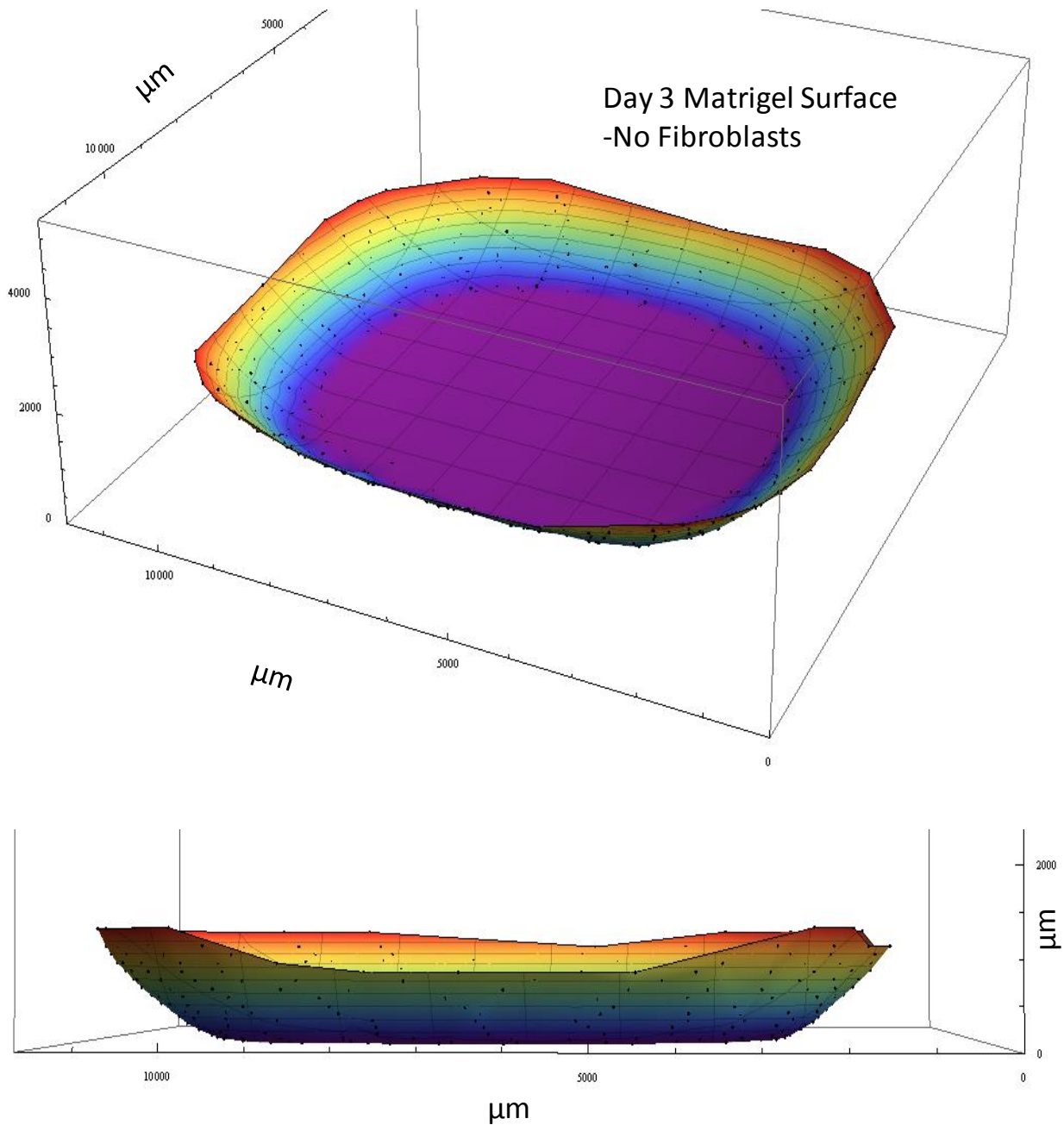
Figure 3.16: Surface plot of Matrigel surface in Figure 3.15. Bottom image is the same surface viewed from the side. The black dots are the measurement points.

Using the patched-together image in Figure 3.15, the locations of the budding ductal structures can be identified and related to the topographical plot of the surface. This has been done in Figure 3.16 where the center of each ductal structure is marked with a black dot. The sample is the same as in the previous figures, and the same color scale is used to indicate depth for the planar projection in Figure 3.16. Surprisingly, most of the ductal structures were found near the outskirts of the relatively flat center area and not higher up on the surface where the meniscus induced more significant curvature. Our own samples also seem to show a similar trend upon close inspection, which is not obvious from the shading in the microscopy images alone. The significance of this occurrence is discussed in the following sections.
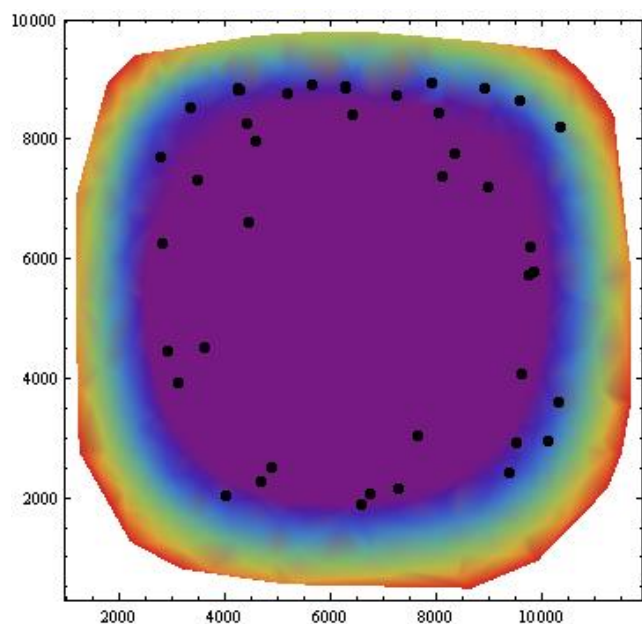

Figure 3.17: Locations of duct formations from Figures 3.14 and 3.15. Same coloring to indicate surface height as Figure 3.15. The large black dots are the centers of small ducts (elongated connections between several cells).
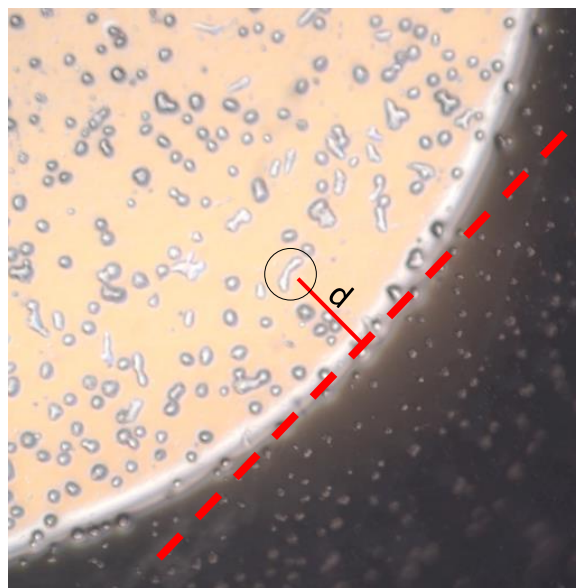
Figure 3.18: Example measurement of duct distance from apparent meniscus boundary.

To further understand the distribution of duct structures the position of the cells relative to the 'beginning' of the region affected by the meniscus was also investigated. As seen in Figure 3.18, the distance from the meniscus is measured from the prominent shaded band visible in the DIC microscopy images. This band is approximately the same as the blue area in the surface plots, where curvature and the change of gel depth become significant. This measurement can be taken as approximate, but it helps quantify the observations. The result of this analysis combining data from the above sample and

an additional sample that was plated at the same time (not shown) is given as a histogram in Figure 3.19 where 0 is the location of the band and positive distances are gives to structures closer to the center of the well. This histogram is weighted by the length of the duct, which relates to the number of cells in the structure.
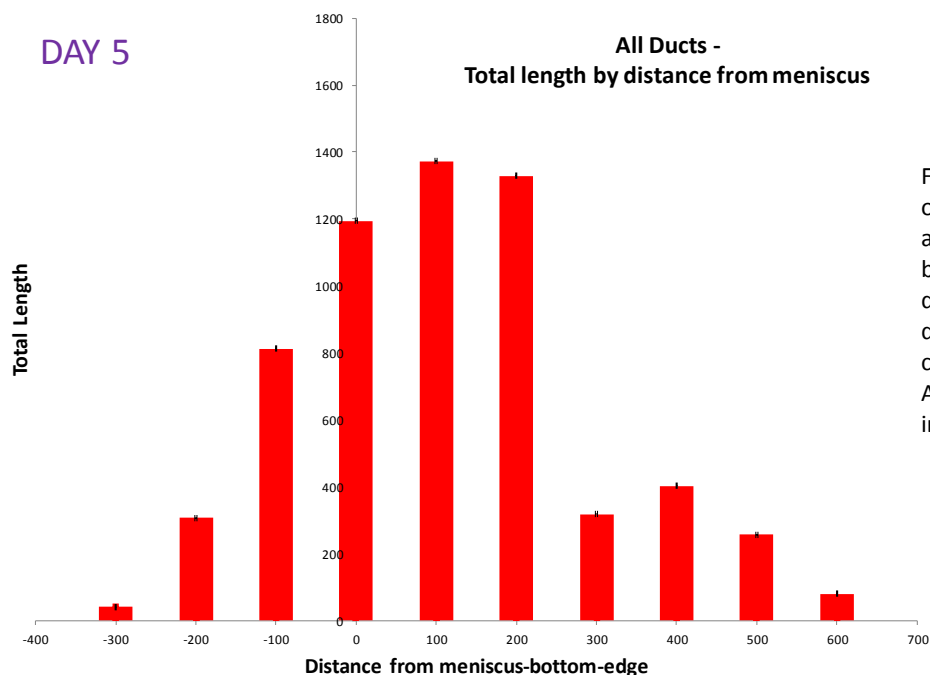
Figure 3.19: Histogram of duct distances from apparent meniscus boundary weighted by duct length. Positive distances are toward the center of the well. Apparent meniscus is indicated in Figure 3.17

3.2.3 Curvature

A first impression might be to consider the curvature of the gel surface as a factor affecting the location of the ductal structures. Indeed, the ducts seem to extend parallel to the boundary of the well along the direction of minimum curvature, so we wonder if the cells may have also aggregated at a position of maximal curvature perpendicular to the edges. To look into this possibility, the curvature can be extracted from the surface data. This is done by using Delaunay triangulation to interpolate between the irregularly scattered surface measurements and then resampling the surface on a structured grid at equal intervals. The structured sampling is then filtered with a Gaussian function, giving a smooth and continuous data set. From this point, we could calculate the maximum and minimum principal curvatures throughout the domain, although this has been simplified by taking a few section cuts perpendicular to the well walls at some well-behaved areas of the surface. The data is still rougher than the surface appears, demonstrating the noise in the best-focus measurement, so a third degree B-spline

function was fit to the section cut, which can then be differentiated to obtain the curvature. The result is in Figure 3.20 with one cut in X (blue) and another in Y (red) in the locations marked in the same figure. The two sections are quite similar, hinting that the surface should be fairly consistent throughout the culture, as expected.
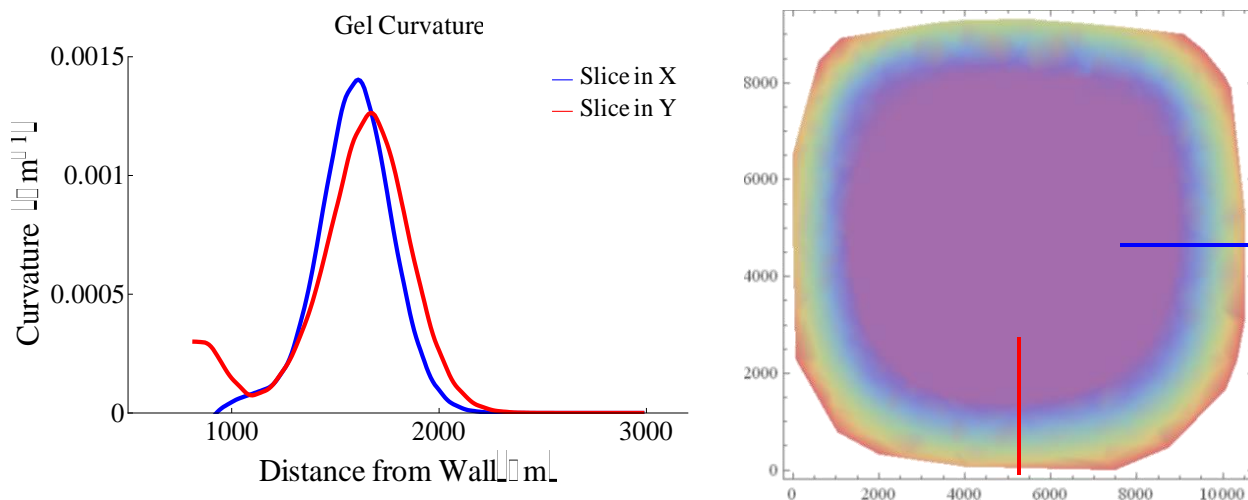
Figure 3.20: Curvature along two representative slices in the gel surface. Image on the right shows location of the cuts. There is an unusual spike to the curvature with the peak 1500-1700µm from the walls.

It can be first noted that there does appear to be a distinct region of maximum curvature. However, the peak seems to lie closer to the walls of the culture dish than where most of the ducts began forming. This could potentially be due to the smoothing required to obtain a continuous curve, so it might be worth repeating the procedure to further investigate the results. It is also interesting to note that this surface and measured curvature do not follow the behavior we expect from fluid mechanics [94] – the curvature should steadily increase moving further up the meniscus towards the wall. It is not clear if this is a result of the measurement technique, or due to the nature of the hydrogel culture. Shrinking or swelling of the gel could occur from the liquid flux with the media, the high protein content might affect the surface differently than a pure liquid, or the cells themselves might reorganize the gel and change the shape of the surface. Optical observation of the surface also becomes more difficult on the severely curved surface close to the walls, which degrades the accuracy away from the flat center region in the culture.

Gel formed into
cylindrical shell

Mold to force
curvature and
thickness

Bottom half also serves
as the culture dish
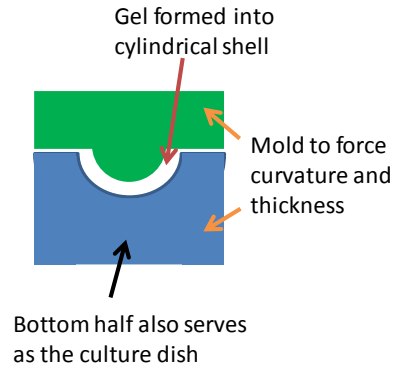
Figure 3.21: Molding gel into cylindrical
shell shape. The top of the mold (green) is
fluorosilanized to prevent the gel from
sticking. Both halves are PDMS

As discussed in the following sections, the gel geometry produced by the meniscus effect also introduces other mechanical cues, such a change in gel depth resulting in a stiffness gradient. To isolate the stiffness effect, the gel geometry can be designed to present a constant curvature in one direction and a constant gel thickness. This is simply achieved by producing a cylindrical annulus of gel using a mold with a defined radius as illustrated in Figure 3.21. The depicted molds are produced by curing PDMS around cylinders of slightly different radii where the gel thickness is defined by the difference in thickness of the two radii. PDMS is used so it may be fluoro-silanized as described in the previous section, leaving it non-stick so the gel is not disturbed when removing the mold. Several radii were examined in the range of about 2-30mm. The lower end of this range is comparable to the magnitude of the curvature at the gel meniscus, although limitations are introduced by the difficulty of viewing such highly curved surfaces and maintaining the gel in such a shape.

If the theory that cells form ducts at a point of maximum curvature and that the ducts grow parallel to the direction of minimum curvature holds, the result from growing cells on cylindrical surfaces should be for cells to form ducts throughout the culture, elongating along the axis of the cylinder. This is not the case. A representative image of the typical cell response to the cylindrical geometry is given in Figure 3.22. This picture is of cells on a 15mm radius sample after 6 days of culture, similar to the level of development of the cells in the figures above. The axis of the cylinder is horizontal in the image. The nascent ductal structures clearly lack a preferred direction for growth. Although the curvature is an order of magnitude less than on the meniscus, the experiments with smaller radii showed similar trends (individual pictures of small radii gels are highly distorted). Between these experiments and the measurements of the meniscus, it seems unlikely that curvature alone is producing these results.
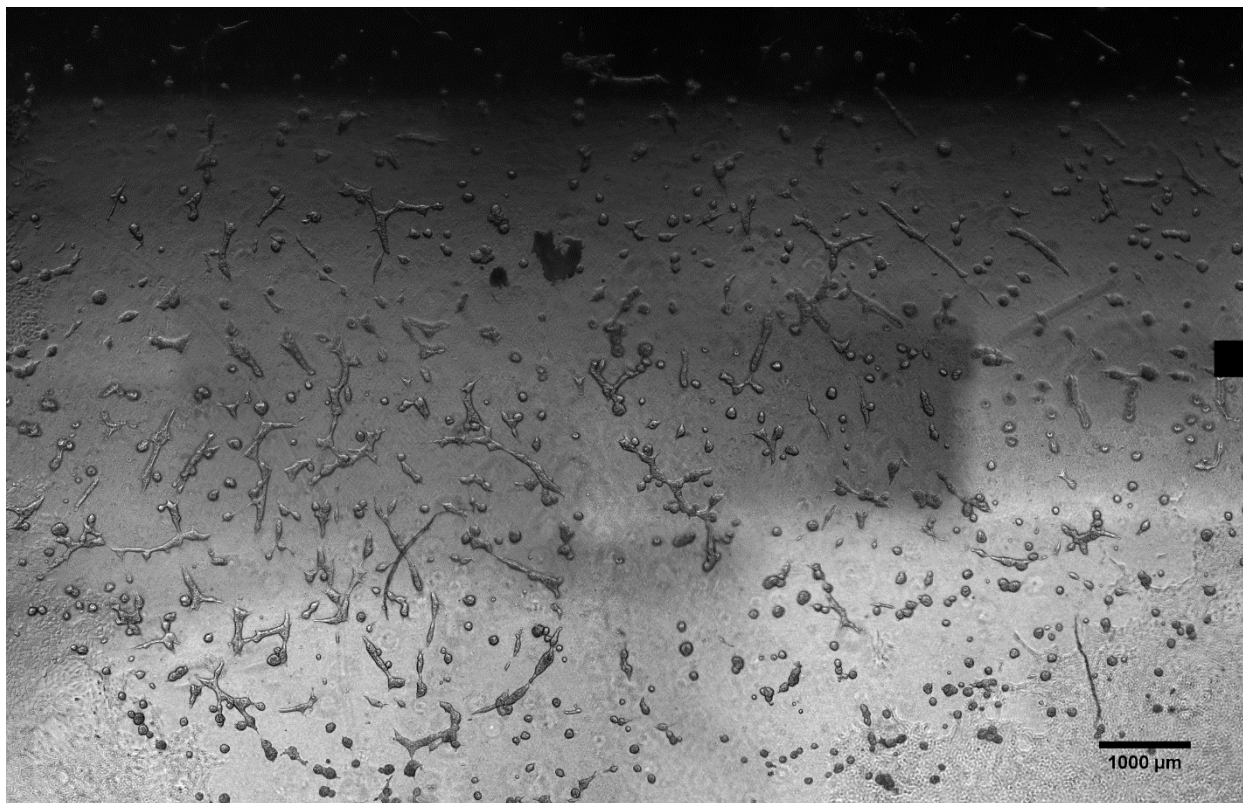
Figure 3.22: Cells growing on constant thickness gel in a cylindrical annulus shape. The axis of the cylinder is horizontal in the image and the radius is 15mm. Image is a composite of 14 individual images, tiled and at different focal planes.

3.2.4 Thickness and Stiffness

Stiffness is a well-known regulator of epithelial cell behavior. It has been observed previously that acini and ducts only form in gels soft enough that cells can deform the gel [95]. It has also been shown that culturing epithelial cells in a soft ECM can partially revert some cancerous phenotypes to normal [96]. Of interest here is whether stiffness might be playing a role in the behavior of the epithelial cells near the meniscus. The obvious question is: can the cells sense the underlying hard substrate from atop the gel? Several studies have been done looking at how far cells can sense below the surface of a gel. Although a region of stiffness gradient has been suggested as low as a few micrometers [97], other studies observe effects at distances up to 50µm and changes in the stress profile up to 200µm for gels of 450Pa modulus [98]. A related observation is that cell-cell interaction may occur at distances up to 600µm for hydrogels containing collagen I [99]. The fact that this distance is much greater than would be expected from

isotropic mechanics alone suggests that the story may be more complex, and cells may sense the boundaries of their container at a much greater distance than predicted.

This longer interaction distance more closely matches our observations from experiments than the shorter estimates. To test if stiffness variation induced by the thickness of the gel was affecting the development of cells seeded atop 3D gels, cultures of MCF10a cells were grown on gels of different thicknesses and compared. The 3D on-top protocol was again followed using a 1:1 mixture of Matrigel and 1 mg/mL collagen I deposited in 96-well polystyrene plates. The amount of gel added to each well was chosen to give nominal thicknesses of 0, 100, 200, 400, 800, 1600, and 3200μm where 0μm is the control without any gel layer. It should be noted that we expect a meniscus to form, thus the center of the well is thinner than the nominal thickness while the edges might be significantly thicker, especially because the wells are relatively small (33mm² area). In each case, including the control, the media contained 2% Matrigel in addition to the standard growth media, which seems to affect the behavior of cells grown on bare polystyrene.
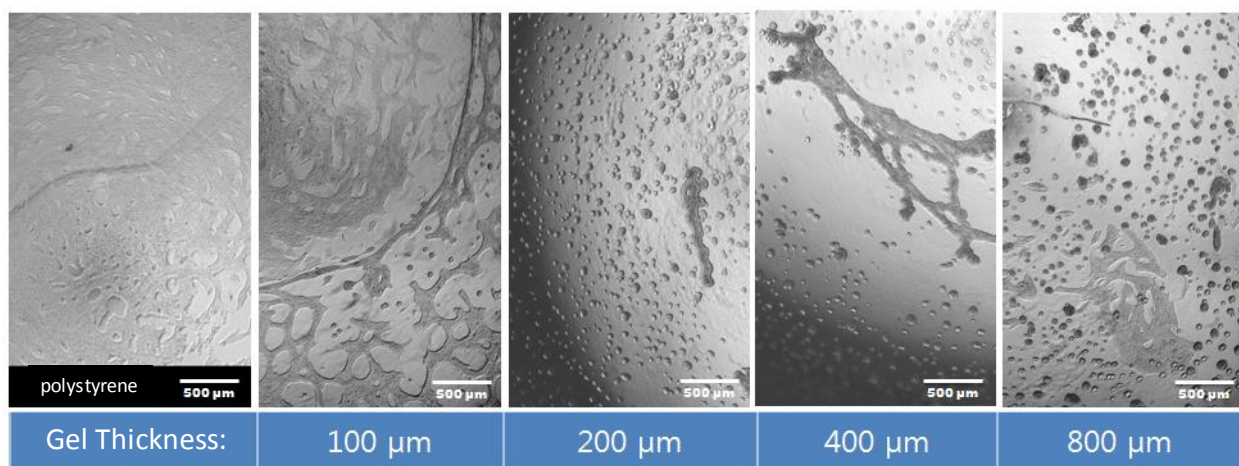
Figure 3.23: Experimental results for MCF10a on different nominal thicknesses of Matrigel. There seems to be a threshold below which cells do not interact and form 3D structures and a threshold above which cells only form acini.

The results of the experiment are displayed in Figure 3.23. We do indeed observe differences between the different thicknesses of gel. There are three types of behavior that summarize the observations. For thin or no gel, cells behave similarly to 2D cultures where they spread and perhaps aggregate, but they remain mostly as a monolayer and do not form 3D structures. For slightly thicker gels in the nominal range of 200-400μm, cells form a mixture of acini and tubules, where the tubules tend to preferentially elongate parallel to the boundary of the well, similar to the observations in the samples provided by

Yvonne. For gels of 800µm and thicker, the culture contains almost exclusively acini that are of similar shape and size throughout the culture. These results support the hypothesis that thickness and/or stiffness are affecting the duct formation.

3.2.5 Wavy Patterns

Thickness and stiffness can also be studied in a more controlled manner by patterning the thickness in a well-defined shape. The wavy patterns discussed in section 2 provide one such method of controlling the shape of a gel, and most applicable is the PDMS-on-PDMS buckling method, which can be used to produce a pattern with wavelength in the range of 150µm to several millimeters. For this explanation, the desired form of the usable pattern is that displayed in Figure 3.24 where a large section of pattern is printed on the bottom of a 35mm culture dish. The procedure for producing such a pattern is the stamping method detailed extensively in section 2.2.5. A section cut through the wavy pattern after applying gel and culturing is given in Figure 3.25. The thickness and shape of the gel, and the locations of the epithelial structures that formed are visible in this side view.
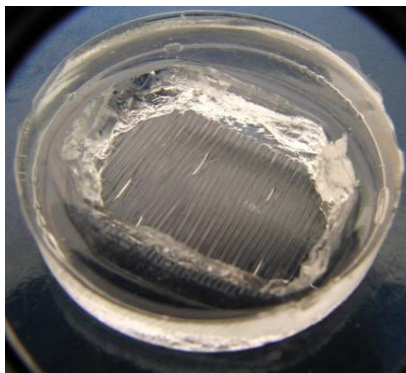
Figure 3.24: Sample with a wavy pattern (850µm pitch, 200µm depth) imprinted in PDMS. Gel can be overlaid on top of the pattern to form a periodic thickness gradient.
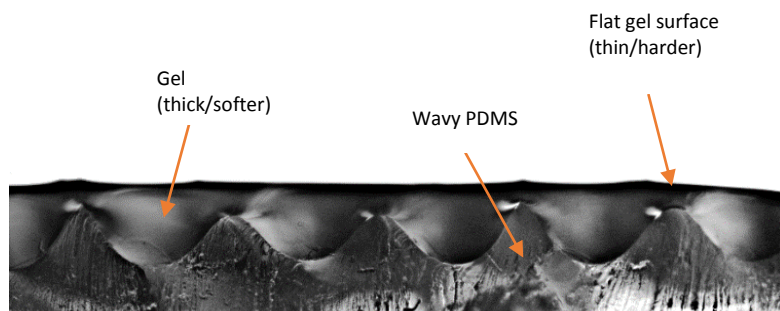
Figure 3.25: Section cut of PDMS-Matrigel interface on a wavy pattern after fixing with 10% formalin (Sigma) and cutting through the culture area with a razor. The surface has no curvature, but the waves affect the stiffness, making the surface effectively stiffer near the peaks.

Cells were cultured using the same technique described for the thickness and curvature experiments. Microscopy images from this experiment are given in Figure 3.25. The first image is of cells grown on the pattern from Figure 3.23 and represents the most interesting result of growing cells on wavy

patterns. For patterns with sufficiently large wavelength where the overlaid gel has thickness similar to the amplitude of the waves, cells will respond dramatically to the pattern. In this case, cells tend to aggregate into long strips over the highest point of the wave and thinnest portion of the gel, and cells form small acini between the strips where the gel is thickest. When the gel is thicker, or the waves are relatively small, such as the 240μm pitch and 50μm depth in the right image of Figure 3.26, cells do not respond to the pattern and only form acini uniformly throughout the culture.
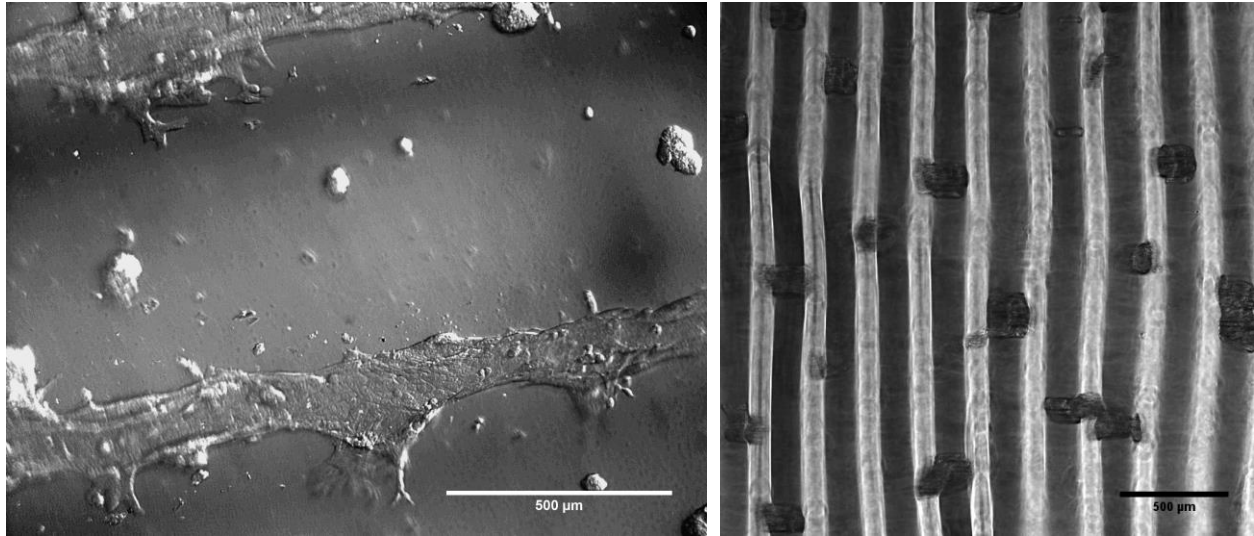
Figure 3.26: MCF10a cells on Matrigel over wavy patterns. Left: 850μm pitch, 200μm depth. Cells tend to aggregate and elongate over the peaks where the gel is thin and form acini over the troughs where the gel is thicker. Right: 240μm pitch, 50μm depth. Cells do not respond to the waves and only form acini throughout the culture.

These results are strong evidence supporting stiffness being the dominant driving force in the formation of duct-like structures. Because the surface of the gel is relatively flat due to the even coating of gel, curvature should not have a significant influence in this case. Moreover, these duct-like structures are much more defined on the wavy patterns than in the meniscus samples, which might correspond to the more significant stiffness gradient present in the wavy samples. Work to quantify the effect of stiffness on epithelial cell movement and aggregation using other dimensions of wavy patterns is currently ongoing. It would seem that the same stiffness effect could explain the formations observed on the meniscus, but a finite element model of both systems would be required to quantitatively compare the two.

3.2.6 Seeding Density

In addition to the previous findings, it is also worth mentioning that seeding density has a significant effect on the formation of ducts and acini. While a low seeding density leads to almost entirely acini, high seeding densities are much more likely to yield networks of tubes. In extreme cases of very high seeding densities, HME496 cells are observed to coalesce into a single cluster consisting of almost every cell plated within the culture container. Several images demonstrating this behavior are presented in Figure 3.27. For observing the formation of ducts in vitro with epithelial cells, more interesting and complex interactions occur when cells are seeded at 5E4 – 1E5 cells/cm² compared to the 2.5E4 cells/cm² suggested in popular protocols [100]. Epithelial cells plated at 2.5E4 cells/cm² tend to form small acini, which will not interact with one another over any reasonable period of time for nonmalignant cells. MCF10a cells will behavior similarly to the HME496 cells in that their interaction
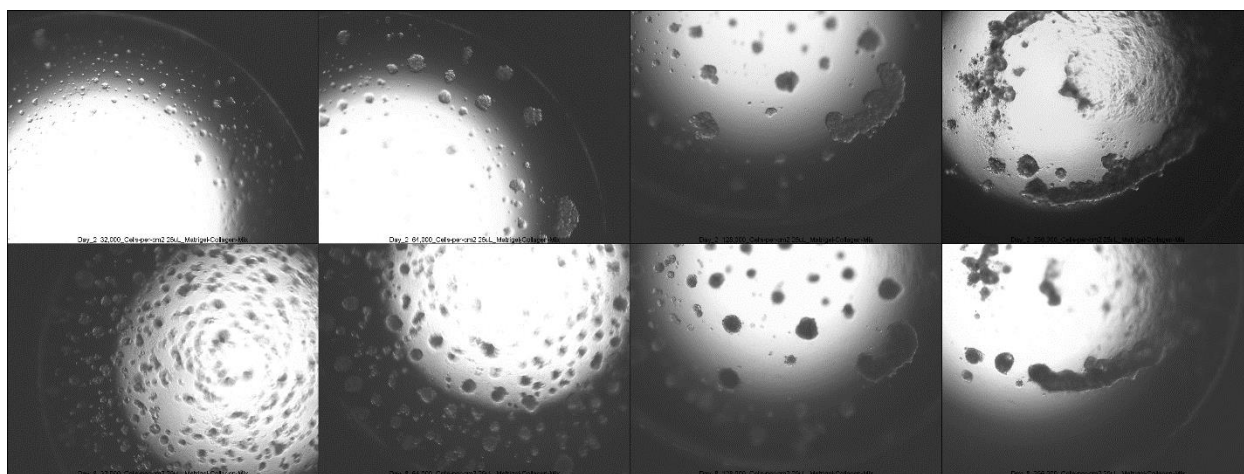
Figure 3.27: HME496 primary epithelial cells seeded at increasing density. From left to right: 32, 64, 128, 256 x 1000 cells/cm² seeding density. Top row is day 2, bottom is day 8. Higher seeding density yields fewer, larger clusters of cells that also aggregate more quickly than in the sparsely seeded specimens.

3.2.7 Future Work

The work remaining to be done on this topic is to definitively link the observations with mechanics and biological processes. The preponderance of evidence presented here indicates a strong link between the mechanical properties of the substrate and the morphology of the structures cells form, but a full explanation including quantifiable effects and a biological mechanism is lacking. Additionally, a useful application of understanding these underlying mechanisms could be demonstrated. One application of

the mechanics would be to control the alignment of muscle cells in the same manner that the formation of epithelial tubes has been directed. Muscle alignment on a 2D pattern as addressed in the previous section is only useful for 2D muscle strip applications. Alignment in 3D could be much more impactful. The wavy patterns coated in gel used to study epithelial alignment could be applied to C2C12 myoblasts to form functional myotubes in 3D. Forming muscle in the hydrogel would also allow other components to be introduced around the muscle such as neurons or blood vessels. This technique offers a good platform for further investigating cell mechanics in 3D cultures.

4. Microscopy Tools

4.1   Automated Stage and Time lapse System

One of the most significant hindrances when studying the development of cells over time is limited throughput. This is especially true when if one wants to obtain a complete and continuous record of the development using time lapse microscopy. In this case, a microscope may be unusable for several days or more while one experiment is conducted examining cells in a limited field of view. Worse, it can be difficult to exactly replicate experimental conditions repeatedly if multiple time lapse sequences are to be compared. This project aimed to address these issues by creating new tools for imaging more samples over larger areas in parallel.

The obvious solution to the problem would be to simply buy several microscopes and replicate the imaging system. However, this is a very expensive and inefficient solution that would also require additional lab space for housing more microscopes. An alternative approach would be to obtain a single system capable of automated imaging of multiple samples. Such systems are commercially available, but again very costly and unrealistic for dedicated, single-purpose use. The implemented solution is instead a custom-designed automated imaging system, taking advantage of the resources already available from the time lapse system in place. The system was designed to be simple and very low cost while maintaining the functionality of a high-end commercial package.

4.1.1 System Overview

Several of the tools and techniques built into the system are individually adaptable to other microscopy systems or individual images, but the complete package of the design is implemented in a single microscope. The system consists of both hardware and software. The hardware includes a 3-axis stage, electronics, motors, environmental controls, and periphery devices. The software includes a program to control the stage and camera from a computer as well as image processing utilities integrated with the stage and camera control that can also be run independently. The entire setup is shown in Figure 4.1.
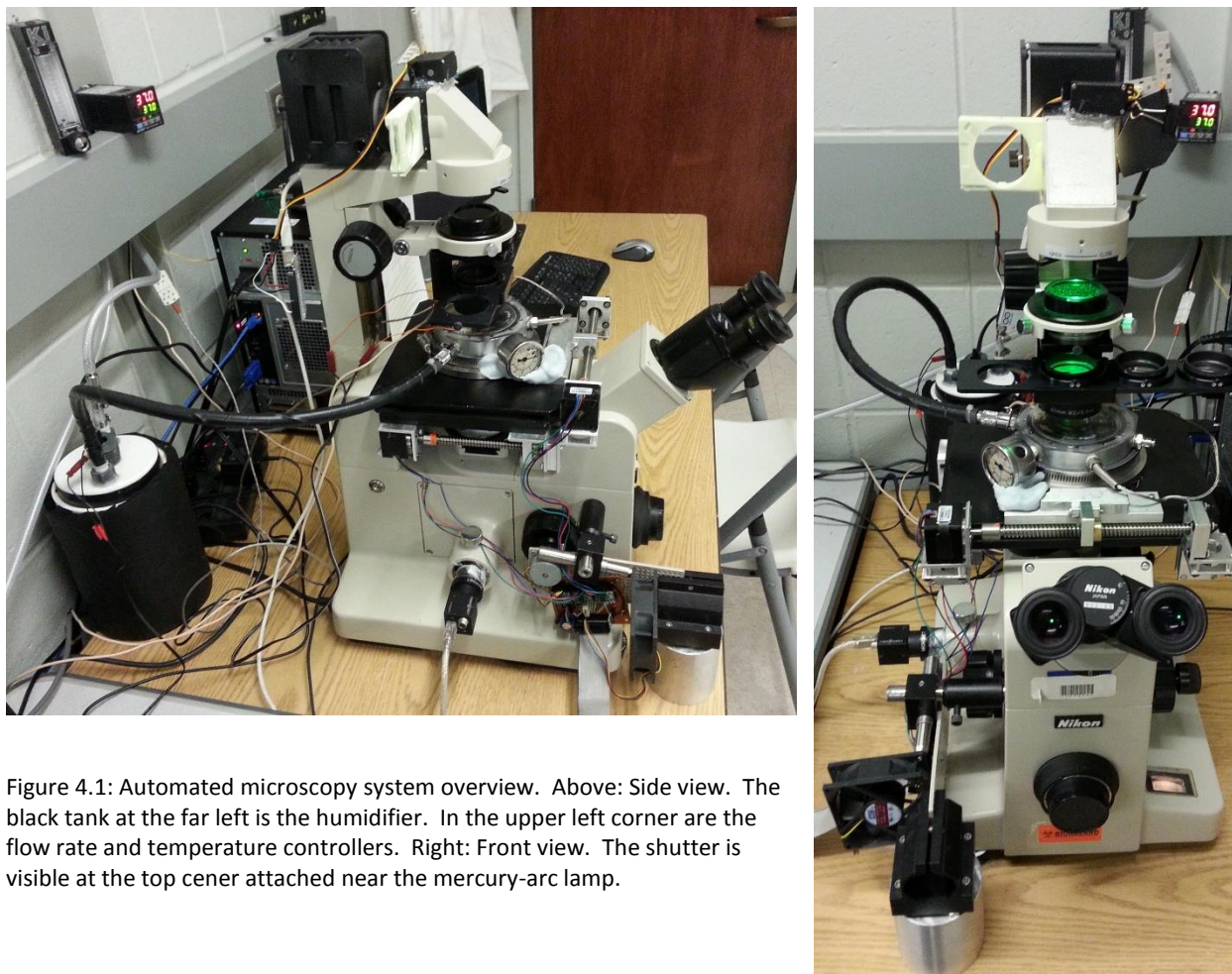
Figure 4.1: Automated microscopy system overview. Above: Side view. The black tank at the far left is the humidifier. In the upper left corner are the flow rate and temperature controllers. Right: Front view. The shutter is visible at the top cener attached near the mercury-arc lamp.

Several scenarios requiring this type of imaging system were in mind when the system was developed. The first is the multi-well or multi-specimen time lapse, where several wells in a standard multi-well plate or several small petri dishes are simultaneously imaged over multiple days. A variation of this would be to record several locations from the same specimen and then merge the data into a single image/video. For 3D cultures and gel specimens, these several locations may be at different depths in the gel as well as different points within the same focal plane. These acquisition and data-condensing techniques are also useful for single exposure (non-time lapse) images where an extended field of focus or larger viewing window can reveal information not possible from a single image. Each of these situations should be possible to handle using this custom system.

4.1.2 Microscope and Camera

The microscope used for the system is a Nikon Diaphot-TMD that was generously donated by Professor Ann Narduli. This is a relatively old microscope that uses Hoffman modulation contrast optics, which requires a unique set of objective lenses and corresponding polarized filters. It should be noted that these items are no longer in production, so upgrading the optics would necessitate replacing all the optics.

Several cameras have been used with this system and microscope, but the current model is a Point Grey Research Flea 3.0, which offers a low-cost, small package design with 2.0MP resolution monochrome output. The current software accesses the camera directly through the manufacturer's API for a high degree of control over the camera's setting. Earlier versions of the software contain code using Microsoft's DirectShow to interface with the camera at a low level, which has the benefit of being compatible with most commercial cameras.

4.1.3 3-Axis Stage and Motion

To transform the stock stage for 3-axis automated control, a set of custom-made brackets and linear actuation assemblies were fabricated to attach to the stage. An image of the CAD model used to design and manufacture the parts are given in Figure 4.2. The mechanics work similarly to the hand-held straining devices described in earlier sections where the manual knobs are replaced by stepper motors. Care was taken to build in the capability of fine-tuning the alignment of components to allow for reasonable tolerances in the measurement and fabrication. Adjusting the tightness of bolts connecting the brackets can help smooth operation of the actuators and ensure repeatable positioning without slip.

The stage movement is accomplished using bipolar stepper motors (Pololu part #1208). These motors have a finite set of stable positions they can settle in called *detents*. The precision of the motor is determined by the number of detents per revolution, which is 200 for these motors. The motors are directly connected to a threaded rod without any additional gearing to generate linear motion. The rod has a 1/8" pitch (moving the attached threaded nut 1/8" per revolution), so the base positioning resolution of the system is 15.9µm.
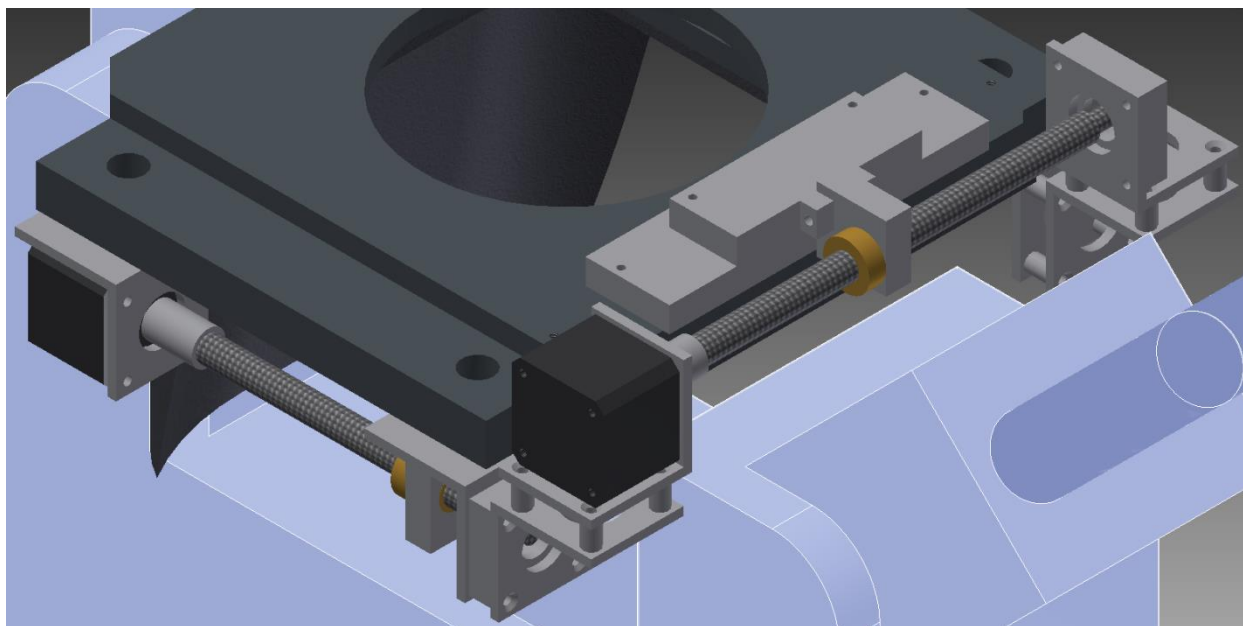
Figure 4.2: CAD model of attachments to Nikon TMD microscope and stage to automated control in the X-Y directions. The blue-gray region is the microscope itself, which was not altered.

If desired, the resolution can be improved by taking fractional steps between each detent – this is performed by the electronic controller by adjusting the current sent to each electromagnetic coil so the motor holds a position partway between two detents. The fractional step size can be set to one of several values down to $1/16^{th}$ (giving approximate 1μm linear resolution) depending on the state of three pins on the controller. For simplicity, only the $1/16^{th}$ step mode is available, which can be toggled with full steps from the software by pressing the letter "m".

Although the precision of these motors can be quite good, it is important to understand the limitations of hobby-grade stepper motors. Unlike a servo motor, the stepper motor has no built-in feedback system to record the state and position of the motor. Thus, the position of the stage is only known relative to its position when powered on, and the relative position is only known by counting the exact number of steps taken in each direction. As long as the motor doesn't slip or get stuck, the position is quite exact and very repeatable. However, if an external force prevents the motor from moving when it is commanded to take a step, the recorded stage position is no longer accurate and will never recover the offset. Consequently, the motors were chosen to be significantly overpowered in an effort to prevent missed steps, and in practice, missed steps do not occur often.

4.1.4 Motor Controller

The motor controller is the portion of the electrical system that allows the computer to control the movement of the motors. To keep the system low cost, the motor is controlled at a low level using off the shelf electronics components. In the present implementation, the computer outputs a digital signal via its parallel port (the ability to output via a microcontroller or data acquisition system is built into the source code), which is connected to a circuit board containing components that send the appropriate current to the motors. The digital signal from the computer is translated to the stepper motors via three stepper driver carriers (Pololu part #1182). The driver carrier chips provide an accessible interface to the A4988 chip, which handles the logic of driving current to the motors. A picture of the actual part is given in Figure 4.3 along with the camera and cooling fan. More detailed information about how the electronics work, troubleshooting, and a circuit diagram are available in the Appendix, Figure 6.6.
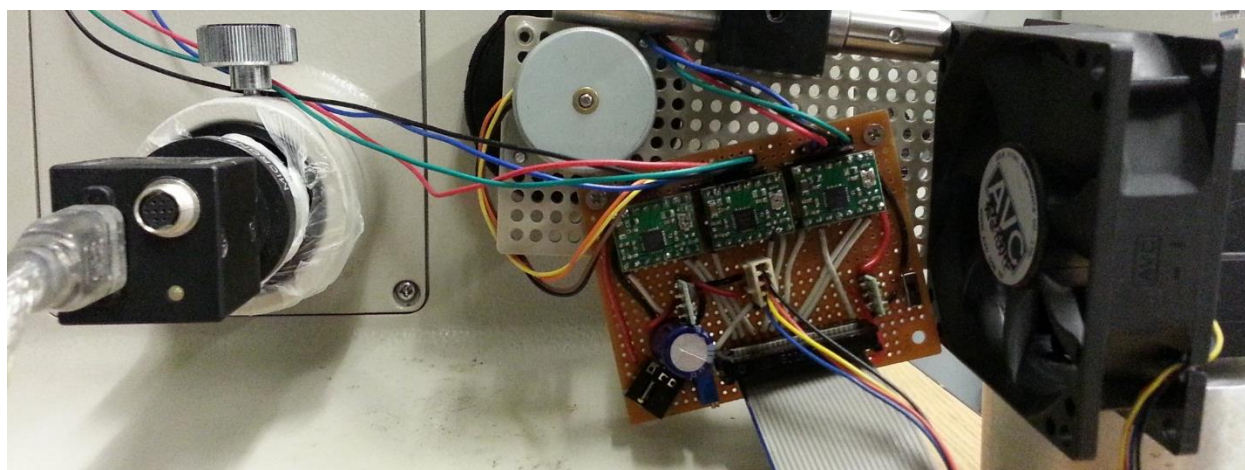
Figure 4.3: Electronics controlling the system. On the left is the Point Grey Flea 3 camera, the center is the motor controller receiving parallel port input via the gray ribbon cable, and on the right is a fan to keep the camera and controller circuitry cool.

4.1.5 Environmental Control

The environmental control hardware, although not strictly part of the automated microscope system, is meant to be used in conjunction with the microscope. Most of the control system was based off the previous system designed by Casey Dyck. Briefly, a heated, cylindrical chamber with an embedded RTD temperature sensor is used to house a culture dish with cells while under observation on the microscope. The chamber is maintained at 37°C with high humidity and 5% CO_2 by means of a PID temperature controller (McMaster # 38615K71) linked to the chamber and a flow meter (McMaster #

4112K93) which regulates the flow of humidified, pre-mixed 5% CO_2. Inlet CO2 is warmed and humidified in a PVC water tank heated with a 25 watt aquarium heater (Top Fin). Additionally, a heated wrap was added around the gas inlet tube, and the chamber lid was replaced by a lid with an encapsulated heating coil to improve environment stability. Components are visible in the picture of the whole system, Figure 4.1.

4.1.6 Peripherals

A couple extra peripheral devices were also installed that may be useful in some situations. First, a shutter was added for the condenser light on the microscope, which is controlled by a servo motor connected to an Arduino communicating with the computer via the USB. The shutter is automatically open/shut during time lapse imaging via the software. There is some concern that cells may be sensitive to continuous exposure to intense light during time lapse imaging, so blocking unnecessary light should attenuate the problem. The other peripheral device available for use is a thermocouple array connected to a DAQ (Measurement Computing, USB-TC). If a DAQ is detected with thermocouples attached, the temperature is automatically logged during time lapse. The framework for the interface with the DAQ and the Arduino is in place so that the functionality may be expanded to include further integration with either of these devices as needed.

4.1.7 Software

A custom software package was developed to integrate the hardware components and allow for operation of the microscope system. The user interfaces with the system mostly through a number of hotkeys and text input. Motion control of the stage is accomplished with 'wasdqe' and the arrow keys, while common tasks like capturing an image, changing camera exposure, and building image sequences are done with one key stroke. The basic operation of the software is simply to maneuver the microscope stage and capture single images via the camera; however, there is significantly more utility available as discussed below. Additional functionality includes capturing real-time and time lapse video, capturing multi-image photos, and changing the variable parameters of the attached components.

4.1.8 Time Lapse Imaging

The primary purpose of this system is to capture complex time lapse video. The automated stage allows various improvements over the standard time lapse sequence. The user can save a series locations that the stage will automatically and repeatedly move to and image with the designated timing. The locations can be further divided into groups that will be imaged and saved together. These locations can be selected by moving the stage to the desired location using the software/motors and then saving the spot, or the location can be manually entered as a tuple of coordinates. Predefined grids can also be added to the moving sequence to form a mosaic image (as described in the next section) that can be captured as part of a time lapse sequence. A preview mode allows the user to cycle through all the saved locations and adjust them for focus and content before starting a time lapse.

Once started, a time lapse may be paused and resumed or canceled without disrupting the timing. Sequences are saved to disk once defined and can be edited with a text editor and loaded at the next start-up. Individual images are immediately accessible to view after capture and may be saved directly online to view remotely. Additionally, the shutter and thermocouple array, if attached, are integrated with the time lapse so that the shutter closes when images are not being captured, and thermocouple readings are taken at the end of each frame.

There are several intended applications for this functionality. One might image multiple locations within a single sample, which may be at different focal planes. Similarly, such multiple locations can be saved as a mosaic, which may be combined together as a single image. A series of mosaics may can be registered (aligned and corrected for shifting over time) and converted into a single video to conveniently view a large area over time. One might also collect several different specimens together in several culture dishes or a multi-well plate and image all the specimens in parallel using time lapse.

4.1.9 Integrated Mosaic Stitching

In addition to the capability of capturing video of multiple wells, the microscope system has the ability to take several images over a large area and merge them into a single image. This utility can be used as a stand-alone program to merge previously captured images, but it is also integrated with the main system control such that a grid of images can be automatically acquired and merged by pressing a single

88

hotkey (the numbers 2-0, indicating the side length of the grid in images – 0 would be 10x10, 100 images). Similar functionality is available to capture such mosaic images in a time lapse sequence.

Although several implementations of the algorithm used to stitch the images together are freely available, such as a popular plugin for ImageJ, Microsoft's ICE, and the stitching module in OpenCV, these sources tend to be prohibitively slow. This may be due in part to the generality of these implementations since they do not account for the *a priori* knowledge of the grid layout. More importantly, any packaged implementation is inherently separated from the live acquisition, requiring a complete set of image files before the processing can begin. When imaging live cells, it is not reasonable to keep cells at room temperature for several minutes while each image is being composited. Saving hundreds of individual images and post-processing is invariably tedious and time-consuming.

The custom, integrated algorithm solves these problems – there is no additional processing time after all the images are captured, only the time needed to write the data to file. This is accomplished by taking full advantage of all the known parameters of the acquisition as described below. The algorithm uses normalized phase correlation in pyramids to calculate the overlap between adjacent images; however, only the region expected to overlap is used in the correlation to greatly speed up the correlation. The correlation is carried out in the frequency space using fast Fourier transformations (FFT), which is equivalent to the spatial cross-correlation but much more efficient for large matrices [101]. The frequency space implementation also allows low frequency components of the correlation (due to differences in lighting and shading) to be readily disregarded by zeroing a few elements of the matrix. Ideally, a single, sharp maxima occurs in the correlation, indicating the offset for the overlap, but in practice there are several maxima. Knowledge about the expected layout is also used to narrow the search area for matches and disregard extraneous maxima corresponding to unlikely displacements.

To ensure robustness and account for noise, the 3 best matches in each phase correlation are saved, similar to the implementation in [102]. There is often significant noise and uncertainty in the correlations, so the locations of all the images in the composite are iteratively searched until a global consensus is reached. This process compares the 3 best correlation matches from each image pair with the consideration that the separation between any two images must be the same no matter what path of overlaps is traversed between the images, i.e.:

$$\overline{AB} + \overline{BD} = \overline{AC} + \overline{CD} = \overline{AD}$$

Where the vectors indicate the offset between any pair of images (similar to Kirchhoff's current law applied to the offset between images, a closed loop must yield 0 offset for consistency). When a consensus cannot be reached for some images, the search area is expanded and different weighting schemes on the FFT are applied to try and find a consistent overlap. If even this fails, the specimen likely slipped or shifted too much during acquisition – the stitching is abandoned and the individual images are saved instead. An example of a 6x6 tiled image showing the wide field of view is given in Figure 4.4.
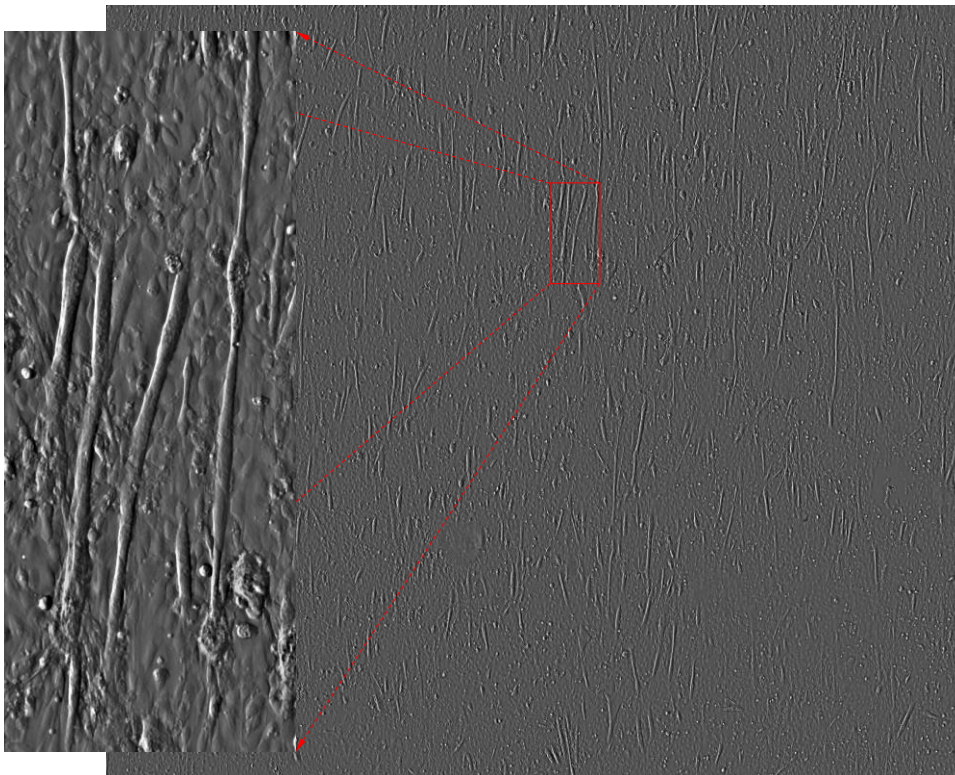
Figure 4.4: Demonstration of stitching algorithm. A raw 6x6 tiled image of myotubes growing on a wavy pattern is presented as captured. Large-scale shading effects can be eliminated during processing. There are no visible seams or glitches in the output image.

By integrating the algorithm into the acquisition procedure, all of the heavy computation can be performed while the stage is moving between images. No matter how many pictures are in the composite, only the overlaps from the last image need to be calculated after all the images are acquired. With images already processed and in memory, the result need only be written to file. However, the time to capture a composite image is still quite significant: generally ~2sec per image to allow the sample to settle after accelerating the stage between imaging location. This can add up to several minutes for a very large image, although it's quite a bit faster than manually saving images to view the same area.

4.1.10 Extended Depth of Field

A method was also developed to merge images from a single location at multiple focal depths. Non-proprietary implementations of this function tend to be geared towards merging dozens of high detail photos (a "z-stack") of an object with complex depth profile to create an aesthetically pleasing image [103]. A high quality output may be produced, but it requires individual attention to each image and non-trivial processing time. For the present implementation, the usage case is generally a large number of z-stacks acquired during a time lapse sequence where the focused region is not quite planar. Each frame is similar to the others in the sequence, and topography of the specimen is a smooth, continuous surface. While this case is relatively simple, a fast and automated method of consistently processing hundreds of similar images is necessary for practical use. This particular functionality is not well satisfied by existing work.

Given a set of images of a scene, it is assumed that portions of the scene are best focused in only one image in the set, and portions of each image that are not in focus are blurry. The area in focus is expected to smoothly vary so that small changes in position lead to small changes in the quality of focus. The algorithm borrows an idea from [104] by decomposing the image into a Gaussian 'contrast pyramid', storing the difference between each level of the Gaussian pyramid. This quickly separates the features at different length scales in the image and allows efficiently blending features at each level of resolution. The separation also aids in determining the level of focus where the highest layers of the pyramid correspond to the highest-frequency details, and increased detail corresponds to high focus.

After decomposing into a pyramid, each image is processed to calculate a value for the focus as a function of space. Focus is calculated in a simple manner similar to [105] which has been implemented in ImageJ, where the local variance in the intensity level is taken as a measure of sharpness. High variance indicates the presence of sharp, high-contrast features, while blurry regions have lower variance. Similar to the statistical measure, variance is defined as:

$$Var = \frac{\sum_i^N (X_i - \bar{X})^2}{N} = \frac{\sum_i^N (X_i{}^2) - (\sum_i^N X_i)^2}{N}$$

Note that $\bar{X}$ is the average value of X. However, for an image we wish to calculate this value locally, for a region centered about each pixel. This can be calculated efficiently for an image as the mean of the square minus the square of the mean, where the local "mean" is calculated with a Gaussian blur to

91

prevent edge effects from a square averaging matrix. Element-wise squaring and subtraction are fast, so this method is significantly more efficient than popular wavelet-based methods [106].

Because the topography is typically smooth, focused regions should be continuous. To enforce this, variance is calculated at each level of the pyramid and then resampled to a coarse level where it is added to the cumulative variance for the image. Contributions from each pyramid level are weighted, with a larger weighting given to high-resolution portions of the pyramid, as these contain the features we wish to preserve. The coarse focus measure is then blurred to further smooth local variations in focus and ensure that maximally focused regions are continuous. Averaging over larger areas helps maintain continuity over regions devoid of features where focus is ambiguous. This procedure gives a measure of sharpness matching well with the perceived sharpness for microscopy images without having to tune the parameters in most cases.

The maximum focus is then chosen for each pixel across all images. To prevent ghosting effects from blending images where individual features may look different (common in phase contrast microscopy), a single image is designated as the most-focused for each point. Blending is only performed at the interfaces between patches from the z-stack images. For this, a novel method of blending is employed such that the low-resolution component is blended over a larger scale than the high resolution components. This is accomplished naturally with the pyramid approach as a constant blending kernel applied at each level of the pyramid blends coarser levels over a larger region. The individual levels are thus blended alone, then each level is up-sampled to the final resolution and added to produce a single image. The output is also slightly enhanced by weighting the low-resolution contribution less than the high resolution contribution, and also by increasing the weight on the high resolution component based on the focus measurement such that low-focus areas have a higher weight on the high resolution component. An example z-stack and result is given in Figure 4.5.

This algorithm is not currently integrated with the stage control software, although it would not be difficult if needed - the program is implemented in standard C++ as a single class. As a standalone application, it will automatically process all the image in a time lapse set at nearly the rate at which the files can be opened and saved. Additional possibilities include using the focus metering as a quasi-quantitative measure of topography for a gel. Presently, the algorithm outputs a height map based on the focus, to which the user may ascribe physical values of height based on the known stage position

where each image was captured, see Figure 4.5. Combined with the multi-image stitching algorithm, this would quickly map the contour of a gel surface, at least approximately.
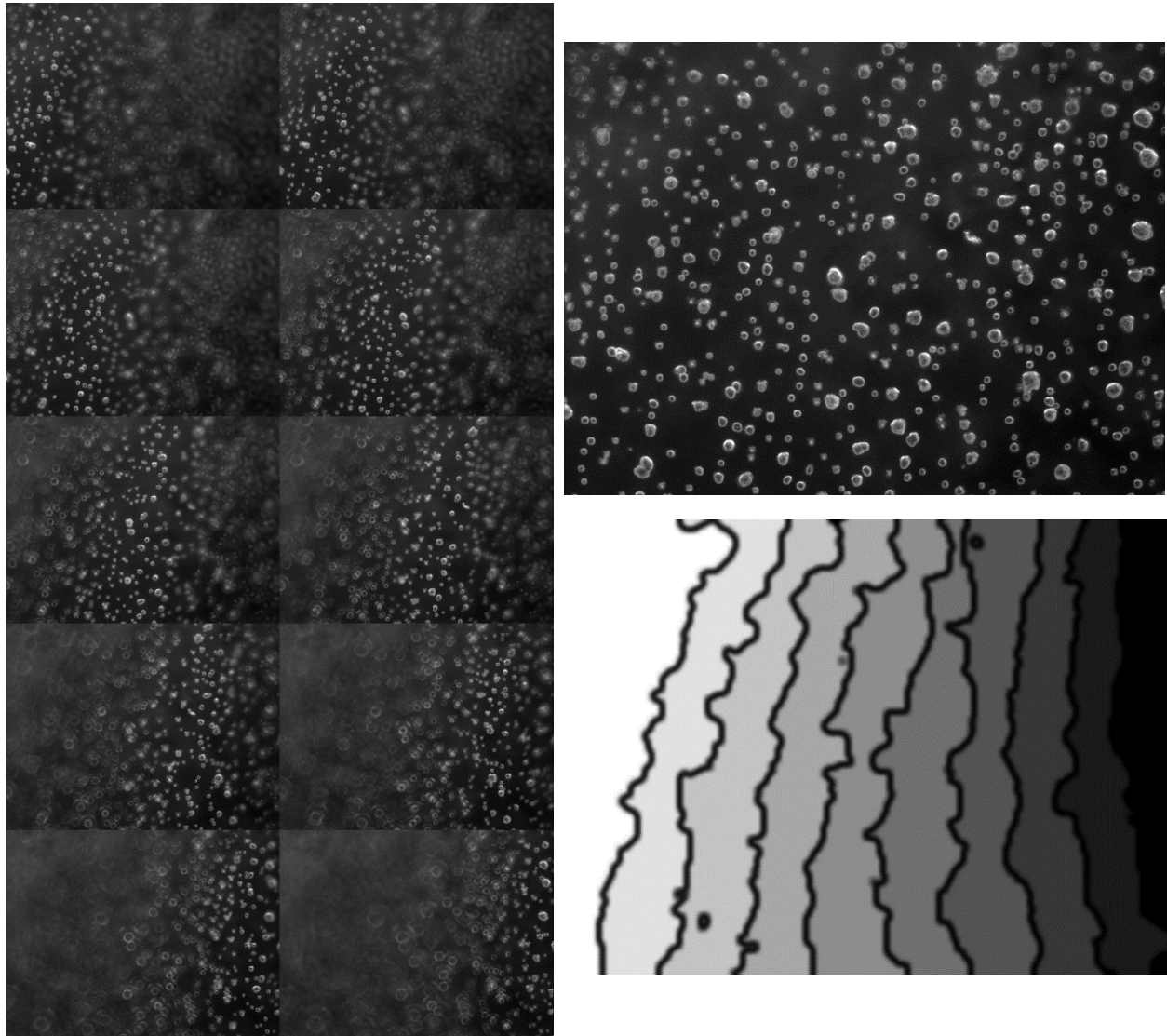
Figure 4.5: Example of an extended depth of field image for typical cells. Right: The 10 original images. Top: The combined and focused image. Bottom: The height map produced by the algorithm - roughly the depth of the cells within the gel.

4.1.11 Adaptation to other Microscopes

The hardware and especially the software from the imaging system can be easily integrated for other microscopes. This has been done with an Olympus IX-51 microscope without an automated stage using the same software. A motor was attached to the focus wheel to automate the z-axis of the stage

without modifying the microscope itself. The software allows time lapse imaging to be combined with extended field of depth and temperature recording without support from the Olympus control software. Images can be post-processed with the stand-alone version of the extended field of depth algorithm as described above. The schematics and instructions in the Appendix would also allow duplicating the electronics and wiring for another microscope stage or any multi-axis movement device. The simple one-axis design can be duplicated in a couple hours with < $40 in parts.

4.1.12 Future and Ongoing Work

The full capability of the system has yet to be exploited. Some potential experiments that would highly benefit from time lapse recording with extended depth of field or mosaic stitching might include imaging the development of mammary tube structures around the meniscus of a small culture well, observing the differentiation and growth of myotubes from a population of myoblasts, imaging (neuro-) muscular development in 3D matrix, or capturing large data sets of cells grown on a gel on top of a large wavy pattern. In practice, it can be difficult to successfully set up such experiments, prevent the sample from shifting or changing, and to keep important areas consistently in focus. Increased usage and familiarity with the system might mitigate those issues.

One of the key developments that will make the system easier to use would be completion of the environmental chamber specifically designed for the stage. Earlier versions of the design using low quality parts were not reliable enough to improve ease of use. A reliable chamber with a large, clear, and nonslip viewing area and with proper mounting to stage via the exposed threaded holes would make some of the aforementioned experiments doable.

4.2 Optogenetics System

Optogenetics is a recently popularized technique used to selectively stimulate cells using light [107]. It has been predominantly used in the study of neural networks, where it allows for stimulation of individual neurons to probe their function [108]. This technique has the advantages of high spatial and temporal resolution while being noninvasive and noncontact. Recently, the field of optogenetics has expanded to include other types of cells, such as muscle cells [109], and allowed for the control of movement in small invertebrates with light [110]. In this study the technique is utilized in an effort to improve upon a previously designed 'biobot' [111] to allow for more precise control rather than the spontaneous contraction in the original design. A stimulation system was created to generate patterned illumination sequences that would allow a light-sensitive biobot to move in a controlled manner.

4.2.1 Cells

To sensitize cells to light, they are first genetically altered to express ion channels that activate when exposed to a particular wavelength. Cells are transduced with two proteins forming light-activated ion channels, one to activate the cell, and another to inactivate it. The first protein, channelrhodopsin-2, is the cation channel that opens when exposed to blue light near 470nm wavelength [112], which stimulates the cell causing it to contract. The second protein is halorhodopsin, which drives a chloride pump causing the cell to hyperpolarize and thus preventing contraction. The halorhodopsin pump is triggered with orange light near 588nm [113]. Between the two proteins, cells be induced to contract with blue light or inhibited with red light. The response occurs at a time scale on the order of a millisecond, offering excellent temporal control.

Two different cell types have been tested with the system. The first cell type was a primary cardiomyocyte harvested from rat heart tissue. This is an extension of the previous biobot design, which also used a rat cardiomyocytes to drive actuation. In this case, a secondary cell line with the necessary transfections is co-cultured with the myocytes to provide the light-activated stimulus (the cardiomyocytes are not active, but are stimulated when the secondary cells fire) due to the difficulty of genetically altering the primary cells. This has the disadvantage of lower yield due to the presence of non-contracting cells and potential difficulty inhibiting contraction. The eventual goal is to use

95

transfected C2C12 cells that will directly respond to light. As of the time this was written, the available population of C2C12 is too weakly responsive to the light to achieve noticeable movement.

4.2.2 Design

The stimulation system is designed for relatively large biobots that may have lengths on the order of 1 – 10mm, which also need to move around freely. Thus, a typical inverted microscope would not provide the necessary field of view, and a custom design was used instead. Figure 4.6 shows the physical setup. The apparatus consists of a 2-axis stage elevated above the focusing optics and the projector used to generate the light stimulation. Above the stage is a USB microscope-camera (Adafruit, 2.0 Megapixel USB Microscope) with adjustable zoom from 25x to 400x with internal optics. The camera is fitted with 550nm dichroic filter to block light at the stimulation wavelengths similar to a fluorescent filter system. The camera and the projector are both connected to a laptop, which controls the system.

Figure 4.6: Overview of the optogenetics system. The stage at the right holds the specimen. The jack allows adjusting the alignment of the projector with the optical train.
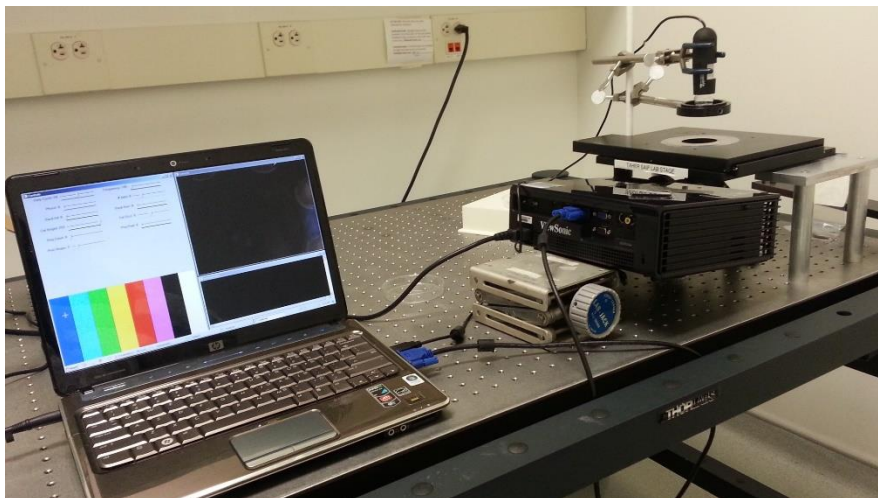
4.2.3 Optics

A commercial projector (ViewSonic PJD5533w) is used for the stimulation light source. This projector uses digital light processing (DLP) technology with a 6 section color wheel to output of 3000 lumens with a resolution of 1280 x 800 pixels. The original optics on the projector are left intact to make fine adjustments to focus and magnification, but several plano-convex lenses were added near the projector outlet to focus light down to the viewing area. The optical components are shown in Figure 4.7.

The spectrum produced by the projector was analyzed with a HR4000 spectrometer (Ocean Optics) using SpectraSuite software. It was found that the optimal output colors were pure blue and pure red (RGB [0, 0,255] and RGB [255, 0, 0]) for activating the channelrhodopsin and halorhodopsin, respectively. Despite the absorption spectrum not quite matching these pure colors, it was found that, due to the nature of the DLP and color wheel, any deviation from pure color adds significant noise over the entire visible spectrum, though it is not detectable with the naked eye. The pure colors do give sharp peaks near their respective wavelengths, so the excitation should be reliable and specific.
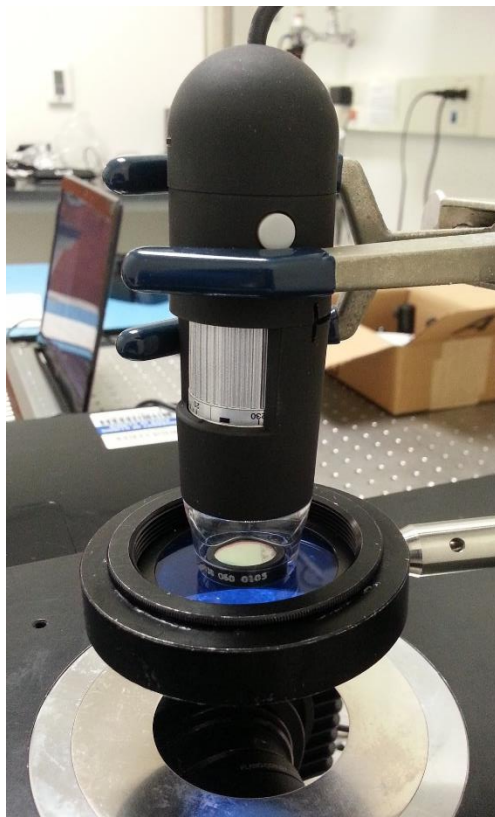
Figure 4.7: Optical components to the optogenetics system. Left: Above the stage, the camera and filters. Top: Below the stage. 4 plano-convex lenses are sandwiched into the housing at the left side of the image. A mirror (center) redirects the light from the projector (far left) upwards toward the stage and camera. Projector light is focused at the plane of the stage top.

4.2.4 Software

Custom software to control the light stimulation system was designed using C++ and the open-source computer vision library, OpenCV. The main functionality provided by the software is to be able to view the specimen and quickly select regions on the image of the specimen for illumination with a desired wavelength of light. There is also the option to produce time-sequenced illumination patterns and to track and illuminate moving objects over time. There are 4 main panels to the program: *Projector*,

Controls, *Camera*, and the command line. If the computer has the projector connected as an extension of the primary monitor (required for operation), the *Projector* window will automatically move to the projector and encompass the entire 'screen'; it outputs the illumination pattern. The *Camera* window holds the input from the camera, overlaid with information about the illuminated regions when applicable. The Controls window allows access to all the variable parameters in the program such as region and timing parameters. The command line prints information about the status of the program. A picture of the interface is given in Figure 4.8 with a proof-of-concept, flower-shaped biobot being globally stimulated to gauge sensitivity to the light.

Figure 4.8: The control interface of the optogenetics system. The specimen being viewed here is a 'flower' coated with cardiomyocytes being illuminated.
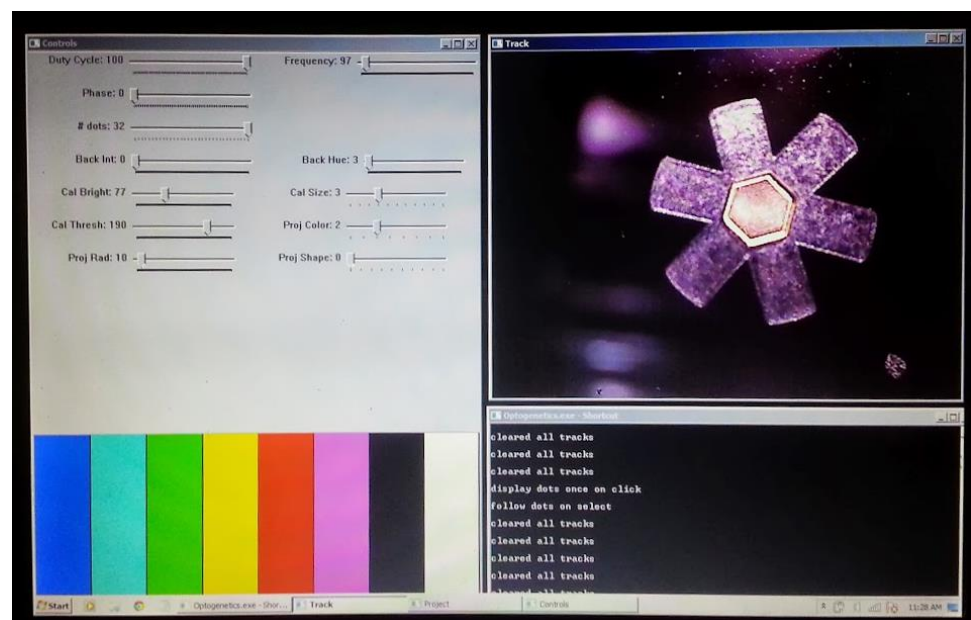
The system allows for the illumination of a number of predefined shapes with adjustable size, color, orientation, timing, and brightness. There are several methods of choosing what areas are illuminated that are toggled using hotkeys (the full user manual is available in the Appendix Figure 6.7):

Point and Click Mode is toggled by pressing "W". When on, an outline of the selection region is visible on the computer screen, and clicking causes the region to be illuminated by the projector while the mouse is depressed. The region can be moved around while remaining illuminated by moving the mouse. When off, the size and location of the shape is chosen by clicking and dragging, in which case the location remains stationary and illuminated until clicking again. If other regions are already saved and being illuminated, they are not affected by this illumination.

98

Save Mode is toggled with the letter "S". When off, locations are only temporarily illuminated as per the *Point and Click Mode* state. When on, user selected regions are saved, which means the regions are continuously illuminated using the pattern specified by the controls panel. The pattern is defined by its frequency, duty cycle, and phase delay between regions. Additional saved regions are added to the end of the sequence. Pressing "C" clears the saved sequence.

Additional options allow for further control over the system. The hue and intensity of the background or baseline projector image can be adjusted to stimulate the specimen or provide general illumination (although even when displaying black, the projector does emit some light, which is usually enough to see the specimen). For example, the background can be set to red to produce generalized inhibition of contraction except in selectively illuminated regions. Similarly, the letter "B" toggles displaying a secondary color for the off state of flashing regions. A recording of the camera feed can be captured by toggling recoding on/off with "V".

Because the projector output and camera input/image processing are separated into their own threads, the system is capable of maintaining very precise timing of the illumination sequencing up to about 30Hz, which is the maximum the projector is capable of outputting (30 on-off cycles is 60Hz frame rate, the maximum for many devices).

4.2.5 Camera-Projector Calibration

One of the key features of the illumination system is the calibration to match the projector output with the camera input. This is necessary so that the exact regions to be illuminated on the specimen can be chosen by selecting the region on the camera image. The task is made nontrivial because any of the camera, projector, or optics may warp the camera's view or the projectors image so that the components are not perfectly aligned along the same optical axis. The system is adjustable for panning, zooming, and rotating, all of which change the correspondence between the camera's view and the projector's image. Also, the camera may only be able to see a small portion of the projector's image, or a small portion may fill the camera's entire field of view. The solution is an automated calibration procedure that calculates the 6 unique components of the affine transformation between camera space and projector space. In practice, the components may be adjusted several times during an experiment to optimize the view, so the procedure must be fast and simple to use in order to maintain workflow.

A prior method of accomplishing this task was a manual approach where the projector displays a 5x5 grid of circles, which the user must click in order on the camera window [110]. This technique is not sufficient in the current setup because some of the grid would typically not be visible on the camera, or it may be rotated 90° or 180° relative to the user. Instead, the system adaptively projects a sequence of randomly located dots, which the program attempts to automatically locate in the camera window. One red, one green, and one blue dot are simultaneously displayed every 50ms because the colors are easily distinguished from the separate channels of the color image, tripling throughput over a monochrome version. Successfully detected dots are saved as a pair of coordinates in projector and camera space. When enough points have been detected to reliably determine the correspondence, a RANSAC algorithm is applied to robustly calculate the transformation.

Because only a small fraction of the projector's image has been visible to the camera at different times during the system's development, the algorithm must adapt the size and location of the displayed dots to match the visible region. To do this robustly, the system chooses points from a Gaussian distribution centered at the current best guess of the center of the view range with decreasing variance as the window becomes more certain. Meanwhile, the set of regions previously illuminated is saved so that a particular spot is not duplicated, which ensures the calibration points are all unique and approximately randomly distributed while improving the convergence rate. Based on the first few detected dots, the brightness and size of the dots is adjusted so they are not oversaturated and fit entirely on the screen, respectively. Dots straddling an edge of the camera window are discarded, but the location is marked as an approximate boundary of the image for use in refining the guess for the window area.

The process is carried out automatically by pressing the hotkey "P" and typically completes in 1-2 seconds. It has been tested successfully when the portion of the projection visible to the camera is as little as 2% as well as when the field of view is larger than the projection area. The transformation matrix is saved to a file and loaded when the program initializes to save time if nothing is changed between experiments. Once calibrated, illuminated shapes are resized and rotated to exactly match what the user selects in the camera feed.

4.2.6 Cell Tracking

The most challenging requirement for the system is being able to follow a moving biobot while still illuminating the proper locations to produces a walking effect. Each cycle of contraction should move the bot slightly, and to produce sustained motion the illumination targets must also move to continue stimulating the same portions of the biobot. Thus, an algorithm is needed to track the motions of the biobot and autonomously update the illuminated regions. This task is somewhat complicated by the fact that a successful, optogenetic biobot has not yet been produced, so there is not a definite template for its form. It is not certain how the biobot will move or change in appearance as it contracts.

Currently, the solution is a generalized tracking algorithm with no built-in assumptions about how shape or texture of the biobot may change over time. The heart of the algorithm is the OpenCV [114] implementation of the optical flow algorithm developed by Lucas and Kanade [115] with improvements to handle sparse feature sets and use image pyramids [116]. The algorithm approximates the local movement of points between two images of a similar scene. Given two images and a set of points in the first image, the output is the set of points in the second image corresponding to the new location of the input points. Thus, objects can be followed by assigning them a set of key points and following the collective motion of the key points in every frame. The key points are identified by another OpenCV function which returns the locations of strong corners and edges.

Some additional work is necessary to make this algorithm useful for tracking. We should first expect some error in the tracked points, and in practice, any individual key point is very likely to be 'lost' (no longer following a point connected to the object) during significant movement of its parent object. To counteract this problem, many key points are identified for each tracked object. Each key point has a weight emphasizing points close to the center of the object, points close to their original orientation relative to the object, and points that are well-matched from previous frames (i.e. confidence that the point is the same point it was in previous frames). The position of an object is determined using the weighted key points with a weighted least squares fit for the translation and rotation of the object between frames. If the weight of a particular point falls below a threshold, indicating the pixel has likely strayed from its original edge/corner, the point is permanently discarded. Over time, an object may lose many of its key points; if the cumulative weight for an object falls below a threshold, the key points are refreshed by using the current location of the object as a selection region.   Figure 4.9 shows an example of the tracking algorithm in use. Without a biobot for testing, these cells are from time lapse culture.
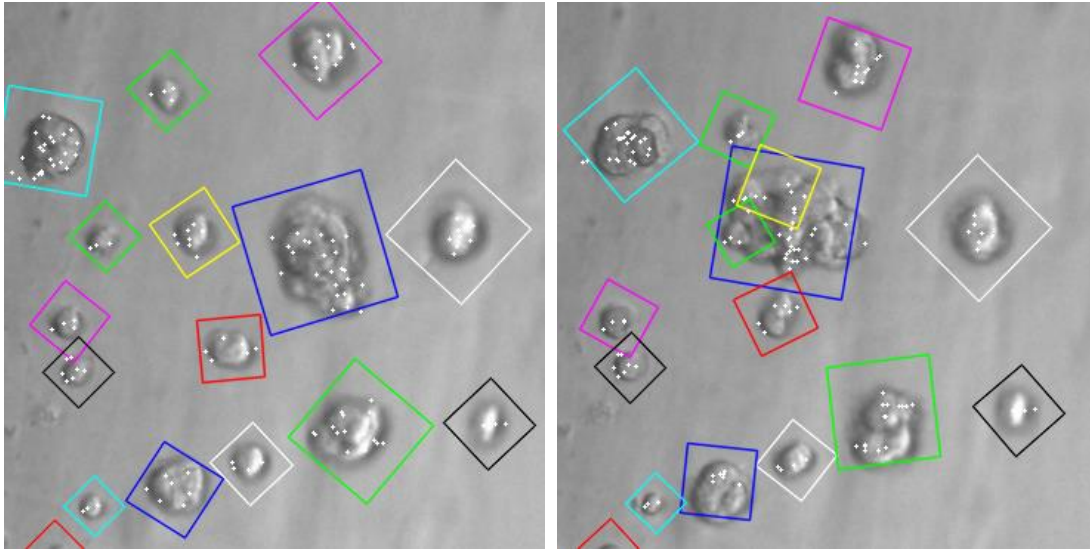
Figure 4.9: Two frames from a time lapse video demonstrating the efficacy of the tracking algorithm for cells similar to what a biobot might look like. The colored squares identify individual cells, their location, and their orientation. Several cells have moved closer to the largest cluster of cells in the center.

One of the advantages of this tracking technique over popular, feature-based tracking is its simplicity and generality. Because cells or biobots may drastically change their shape or move into or out of the focal plane, it can be difficult to identify consistent features of a particular body. This can be partially avoided by not attempting to locate specific features and instead simply looking at the general movement of prominent pixels. In testing with various common objects in several different background settings, the point-based tracking method was generally more robust to large changes than the common SURF and SIFT algorithms. However, if future developers wish to change the implementation of the point tracking, it can be relatively easily done without affecting the downstream logic due to the modular nature of the source code.

The sparse optical flow also has the advantage of being very fast. By aggregating the key points from all the tracked objects into one call to the optical flow function, we eliminate the redundant and costly pre-processing that would occur if the optical flow function were called once for each object. This results in achieving the same performance for almost any number of tracked objects. Even on a relatively old laptop the tracking algorithm is generally limited by the capture rate of the camera. Most cheap USB cameras automatically choose their own frame rate based on the ambient light level, with typical values between 8 and 60 fps. In good light, the actual object update rate is usually in the 50-60 fps range for a

640 x 480 image with multiple objects. This high speed also helps improve the accuracy as the difference between successive frames is typically small, making it easy to match points.

4.2.7 Ongoing Work

There is a great deal of potential work left for this project. So far, the best results were obtained by stimulating the flower in Figure 4.8, where it was not clear if the flower had a significant response due to spontaneous contraction. A major advancement will be improving the responsiveness of cells to light, at which point more interesting results may be obtained. Until then, the function of the stimulation system is in order and ready for manipulating cell cultures.

The ongoing issue is the weak and dilute response from the C2C12 cells upon light stimulation. The original system was built with a single focusing lens for easy testing, but a low portion of the projector output was guided to the target viewing area. A recent, still untested, improvement in the optics has been to add a series of lens to narrow the focus to a much smaller region while still minimizing dispersion. The particular projector was chosen for its relatively high lumen output because the power of smaller projectors was identified as a problem in previous studies, so it is expected that a successfully transfected population of C2C12 should be reactive in the current configuration. After a working C2C12 biobot is demonstrated, the next step will likely be to innervate the muscle strip with neurons and then stimulate the neurons to induce contraction. The stimulation system should be a useful tool in testing the different components of an integrated biobot design in line with the long term goals of the EBICS NSF STC.

References

1.   Cassie, A. B. D. & Baxter, S. Wettability of porous surfaces. *Trans Faraday Soc* **40,** 546–551 (1944).

2.   McHale, G. Cassie and Wenzel: were they really so wrong? *Langmuir* **23,** 8200–5 (2007).

3.   Gao, L. & McCarthy, T. J. How Wenzel and cassie were wrong. *Langmuir* **23,** 3762–5 (2007).

4.   Gao, L. & McCarthy, T. J. An attempt to correct the faulty intuition perpetuated by the Wenzel and Cassie "laws". *Langmuir* **25,** 7249–55 (2009).

5.   Marmur, A. & Bittoun, E. When Wenzel and Cassie are right: reconciling local and global considerations. *Langmuir* **25,** 1277–81 (2009).

6.   Whyman, G., Bormashenko, E. & Stein, T. The rigorous derivation of Young, Cassie–Baxter and Wenzel equations and the analysis of the contact angle hysteresis phenomenon. *Chem Phys Lett* **450,** 355–359 (2008).

7.   Cubaud, T. & Fermigier, M. Advancing contact lines on chemically patterned surfaces. *J Colloid Interface Sci* **269,** 171–177 (2004).

8.   Courbin, L., Bird, J. C., Reyssat, M. & Stone, H. a. Dynamics of wetting: from inertial spreading to viscous imbibition. *J Phys Condens Matter* **21,** 464127 (2009).

9.   Emmer, M. & Brakke, K. a. Surface Evolver. *Exp Math* **25,** 391 (1992).

10.   Emmer, M. & Brakke, K. a. Surface Evolver. *Surf Evolver Doc* **25,** 1 (1999).

11.   Harsh, K. F., Bright, V. M. & Lee, Y. C. Solder self-assembly for three-dimensional microelectromechanical systems. *Sensors Actuators A Phys* **77,** 237–244 (1999).

12.   Brakke, K. A. & Sullivan, J. M. Using Symmetry Features of the Surface Evolver to Study Foams.

13.   Li, W. & Amirfazli, a. Microtextured superhydrophobic surfaces: a thermodynamic analysis. *Adv Colloid Interface Sci* **132,** 51–68 (2007).

14.   Brandon, S., Haimovich, N., Yeger, E. & Marmur, A. Partial wetting of chemically patterned surfaces: The effect of drop size. *J Colloid Interface Sci* **263,** 237–243 (2003).

15.   Chen, Y., He, B., Lee, J. & Patankar, N. a. Anisotropy in the wetting of rough surfaces. *J Colloid Interface Sci* **281,** 458–64 (2005).

16.   Choi, W., Tuteja, A., Mabry, J. M., Cohen, R. E. & McKinley, G. H. A modified Cassie-Baxter relationship to explain contact angle hysteresis and anisotropy on non-wetting textured surfaces. *J Colloid Interface Sci* **339,** 208–16 (2009).

17.   Mognetti, B. M. & Yeomans, J. M. Modeling receding contact lines on superhydrophobic surfaces. *Langmuir* **26,** 18162–8 (2010).

18.   Courbin, L. *et al.* Imbibition by polygonal spreading on microdecorated surfaces. *Nat Mater* **6,** 661–4 (2007).

19.   Cubaud, T. & Fermigier, M. Faceted drops on heterogeneous surfaces. *Europhys Lett* **55,** 239–245 (2001).

20.   Ahuja, a *et al.* Nanonails: a simple geometrical approach to electrically tunable superlyophobic surfaces. *Langmuir* **24,** 9–14 (2008).

21.   Boucher, E., Evans, M. & Jones, T. The computation of interface shapes for capillary systems in a gravitational field. *Adv Colloid Interface Sci* **27,** 43–79 (1987).

22.   Dufour, R. *et al.* Engineering sticky superomniphobic surfaces on transparent and flexible PDMS substrate. *Langmuir* **26,** 17242–7 (2010).

23.   Hao, P., Lv, C., Yao, Z. & He, F. Sliding behavior of water droplet on superhydrophobic surface. *EPL (Europhysics Lett* **90,** 66003 (2010).

24.   Mahadevan, L. & Pomeau, Y. Rolling Droplets. *Phys Fluids* **11,** 2449–2453 (1999).

25.   Quere, D. Drops at Rest on a Tilted Plane. *Langmuir* **14,** 2213–2216 (1998).

26.   Li, H. Solid-Liquid Interactions in Microscale Structures and Devices. 1–137 (2011).

27.   Reyssat, M. & Quéré, D. Contact angle hysteresis generated by strong dilute defects. *J Phys Chem B* **113,** 3906–9 (2009).

28.   Hutchinson, J. W., Thouless, M. D. & Liniger, E. G. Growth and Configurational Stability of Circular Buckling-Driven Film Delaminations. *Acta Met Mater* **40,** 295–308 (1992).

29.   Bowden, N., Brittain, S., Evans, A., Hutchinson, J. & Whitesides, G. Spontaneous formation of ordered structures in thin. *Nature* **393,** 146–148 (1998).

30.   Lam, M. T., Sim, S., Zhu, X. & Takayama, S. The effect of continuous wavy micropatterns on silicone substrates on the alignment of skeletal muscle myoblasts and myotubes. *Biomaterials* **27,** 4340–4347 (2006).

31.   Harrison, C., Stafford, C. M., Zhang, W. & Karim, A. Sinusoidal phase grating created by a tunably buckled surface. *Appl Phys Lett* **85,** 4016 (2004).

32.   Kim, D.-H., Ghaffari, R., Lu, N. & Rogers, J. a. Flexible and stretchable electronics for biointegrated devices. *Annu Rev Biomed Eng* **14,** 113–28 (2012).

33.   Groenewold, J. Wrinkling of plates coupled with soft elastic media. *Phys A Stat Mech its Appl* **298,** 32–45 (2001).

34.   Bowden, N., Huck, W. T. S., Paul, K. E. & Whitesides, G. M. The controlled formation of ordered, sinusoidal structures by plasma oxidation of an elastomeric polymer. *Appl Phys Lett* **75,** 2557 (1999).

35.   Mora, T. & Boudaoud, a. Buckling of swelling gels. *Eur Phys J E Soft Matter* **20,** 119–24 (2006).

36. Volynskii, A. L., Bazhenov, S., Lebedeva, O. V & Bakeev, N. F. Mechanical buckling instability of thin coatings deposited on soft polymer substrates. *J Mater Sci* **5,** 547–554 (2000).

37. Choi, W. M. *et al.* Biaxially stretchable "wavy" silicon nanomembranes. *Nano Lett* **7,** 1655–63 (2007).

38. Jiang, H. *et al.* Finite deformation mechanics in buckled thin films on compliant supports. *Proc Natl Acad Sci U S A* **104,** 15607–15612 (2007).

39. Schneider, F., Draheim, J., Kamberger, R. & Wallrabe, U. Process and material properties of polydimethylsiloxane (PDMS) for Optical MEMS. *Sensors Actuators A Phys* **151,** 95–99 (2009).

40. Schneider, F., Fellner, T., Wilde, J. & Wallrabe, U. Mechanical properties of silicones for MEMS. *J Micromechanics Microengineering* **18,** 065008 (2008).

41. Chua, D. B. H., Ng, H. T. & Li, S. F. Y. Spontaneous formation of complex and ordered structures on oxygen-plasma-treated elastomeric polydimethylsiloxane. *Appl Phys Lett* **76,** 721 (2000).

42. Wu, C.-C., Yuan, C.-Y. & Ding, S.-J. Effect of polydimethylsiloxane surfaces silanized with different nitrogen-containing groups on the adhesion progress of epithelial cells. *Surf Coatings Technol* **205,** 3182–3189 (2011).

43. Béfahy, S. *et al.* Thickness and elastic modulus of plasma treated PDMS silica-like surface layer. *Langmuir* **26,** 3372–5 (2010).

44. Mills, K. L., Zhu, X., Takayama, S. & Thouless, M. D. The mechanical properties of a surface-modified layer on poly(dimethylsiloxane). *J Mater Res* **23,** 37–48 (2008).

45. Hillborg, H., Tomczak, N., Olàh, A., Schönherr, H. & Vancso, G. J. Nanoscale hydrophobic recovery: A chemical force microscopy study of UV/ozone-treated cross-linked poly(dimethylsiloxane). *Langmuir* **20,** 785–94 (2004).

46. Bodas, D., Rauch, J.-Y. & Khan-Malek, C. Surface modification and aging studies of addition-curing silicone rubbers by oxygen plasma. *Eur Polym J* **44,** 2130–2139 (2008).

47. Wang, S., Song, J., Kim, D.-H., Huang, Y. & Rogers, J. a. Local versus global buckling of thin films on elastomeric substrates. *Appl Phys Lett* **93,** 023126 (2008).

48. Wang, S., Kallur, A. & Goshu, A. Fabrication and characterization of PDMS thin film. **7935,** 79350M–79350M–6 (2011).

49. Mata, A., Fleischman, A. J. & Roy, S. Characterization of polydimethylsiloxane (PDMS) properties for biomedical micro/nanosystems. *Biomed Microdevices* **7,** 281–293 (2005).

50. Koschwanez, J. H., Carlson, R. H. & Meldrum, D. R. Thin PDMS films using long spin times or tert-butyl alcohol as a solvent. *PLoS One* **4,** e4572 (2009).

51. Clark, P., Dunn, G. a, Knibbs, A. & Peckham, M. Alignment of myoblasts on ultrafine gratings inhibits fusion in vitro. *Int J Biochem Cell Biol* **34,** 816–825 (2002).

52. Clark, P., Connolly, P., Curtis, a S., Dow, J. a & Wilkinson, C. D. Cell guidance by ultrafine topography in vitro. *J Cell Sci* **99,** 73–77 (1991).

53. Teixeira, A. I., Abrams, G. A., Bertics, P. J., Murphy, C. J. & Nealey, F. Epithelial contact guidance on well-defined micro- and nanostructured substrates. **116,** 1881–1892 (2003).

54. Corning, D. Product Information: Sylgard ® 184 Silicone Elastomer. 1–3

55. Stafford, C. M. *et al.* A buckling-based metrology for measuring the elastic moduli of polymeric thin films. *Nat Mater* **3,** 545–50 (2004).

56. Kemkemer, R., Jungbauer, S., Kaufmann, D. & Gruler, H. Cell orientation by a microgrooved substrate can be predicted by automatic control theory. *Biophys J* **90,** 4701–4711 (2006).

57. Van Delft, F. C. M. J. M. *et al.* Manufacturing substrate nano-grooves for studying cell alignment and adhesion. *Microelectron Eng* **85,** 1362–1366 (2008).

58. Teixeira, A. I., Nealey, P. F. & Murphy, C. J. Responses of human keratocytes to micro- and nanostructured substrates. *J Biomed Mater Res A* **71,** 369–76 (2004).

59. Dunn, G. A. & Heath, J. P. A New Hypothesis of Contact in Tissue Cells. *Exp Cell Res* **101,** 1–14 (1976).

60. Jiang, X. *et al.* Controlling Mammalian Cell Spreading and Cytoskeletal Arrangement with Conveniently Fabricated Continuous Wavy Features on Poly(dimethylsiloxane). *Langmuir* **18,** 3273–3280 (2002).

61. Mathur, A., Moore, S. W., Sheetz, M. P. & Hone, J. The role of feature curvature in contact guidance. *Acta Biomater* **8,** 2595–2601 (2012).

62. James, J., Goluch, E. D., Hu, H., Liu, C. & Mrksich, M. Subcellular curvature at the perimeter of micropatterned cells influences lamellipodial distribution and cell polarity. *Cell Motil Cytoskeleton* **65,** 841–852 (2008).

63. Wang, L., Sun, B., Ziemer, K. S., Barabino, G. a & Carrier, R. L. Chemical and physical modifications to poly(dimethylsiloxane) surfaces affect adhesion of Caco-2 cells. *J Biomed Mater Res A* **93,** 1260–1271 (2009).

64. Chou, L., Firth, J. D., Uitto, V. J. & Brunette, D. M. Substratum surface topography alters cell shape and regulates fibronectin mRNA level, mRNA stability, secretion and assembly in human fibroblasts. *J Cell Sci* **108 (Pt 4,** 1563–73 (1995).

65. Wigmore, P. M., Maleki, F., Evans, D. J. & McErlain, M. After embryonic day 17, distribution of cells on surface of primary muscle fibres in mouse is non-random. *Dev Dyn* **207,** 215–221 (1996).

66. Fujita, S., Ohshima, M. & Iwata, H. Time-lapse observation of cell alignment on nanogrooved patterns. *J R Soc Interface* **6,** S269–S277 (2009).

67. Loesberg, W. a *et al.* The threshold at which substrate nanogroove dimensions may influence fibroblast alignment and adhesion. *Biomaterials* **28,** 3944–3951 (2007).

68.   Aubin, H. *et al.* Directed 3D cell alignment and elongation in microengineered hydrogels. *Biomaterials* **31,** 6941–6951 (2010).

69.   Luna, J. I., Ciriza, J., Ph, D., Garcia-ojeda, M. E. & Kong, M. Multiscale Biomimetic Topography for the Alignment of Neonatal and Embryonic Stem Cell-Derived Heart Cells. *Tissue Eng Part C* **17,** 579–588 (2011).

70.   Magdalena, J. Microtubule involvement in NIH 3T3 Golgi and MTOC polarity establishment. *J Cell Sci* **116,** 743–756 (2003).

71.   Sutherland, J., Denyer, M. & Britland, S. Contact guidance in human dermal fibroblasts is modulated by population pressure. *J Anat* **206,** 581–587 (2005).

72.   Dunn, G. a & Brown, a F. Alignment of Fibroblasts on Grooved Surfaces Described by a Simple Geometric Transformation. *J Cell Sci* **83,** 313–40 (1986).

73.   Peterbauer, T. *et al.* Dynamics of Spreading and Alignment of Cells Cultured In Vitro on a Grooved Polymer Surface. *J Nanomater* **2011,** 1–10 (2011).

74.   Ayres, C. E. *et al.* Measuring fiber alignment in electrospun scaffolds: a user's guide to the 2D fast Fourier transform approach. *J Biomater Sci Polym Ed* **19,** 603–621 (2008).

75.   Bajaj, P. *et al.* Patterning the differentiation of C2C12 skeletal myoblasts. *Integr Biol (Camb)* **3,** 897–909 (2011).

76.   Grote, M. J., Palumberi, V., Wagner, B., Barbero, A. & Martin, I. Dynamic formation of oriented patches in chondrocyte cell cultures. *J Math Biol* **63,** 757–777 (2011).

77.   Biela, S. a, Su, Y., Spatz, J. P. & Kemkemer, R. Different sensitivity of human endothelial cells, smooth muscle cells and fibroblasts to topography in the nano-micro range. *Acta Biomater* **5,** 2460–2466 (2009).

78.   Vogel, V. & Sheetz, M. Local force and geometry sensing regulate cell functions. *Nat Rev Mol Cell Biol* **7,** 265–275 (2006).

79.   Erickson, C. A. Analysis of the Formation of Parallel Arrays by BHK Cells In Vitro. *Exp Cell Res* **115,** 303–315 (1978).

80.   Kang, K., Perthame, B., Stevens, A. & Velázquez, J. J. L. An integro-differential equation model for alignment and orientational aggregation. *J Differ Equ* **246,** 1387–1421 (2009).

81.   Mogilner, A. & Edelstein-keshet, L. Spatio-angular order in populations of self-aligning objects: formation of oriented patches. *Phys D* **89,** 346–367 (1996).

82.   Wang, P.-Y., Yu, H.-T. & Tsai, W.-B. Modulation of alignment and differentiation of skeletal myoblasts by submicron ridges/grooves surface structure. *Biotechnol Bioeng* **106,** 285–294 (2010).

83.   Clark, P., Connolly, P., Curtis, a S., Dow, J. a & Wilkinson, C. D. Topographical control of cell behaviour: II. Multiple grooved substrata. *Development* **108,** 635–44 (1990).

84.   Gingras, J. *et al.* Controlling the orientation and synaptic differentiation of myotubes with micropatterned substrates. *Biophys J* **97,** 2771–2779 (2009).

85.   Wakelam, M. J. The fusion of myoblasts. *Biochem J* **228,** 1–12 (1985).

86.   Kamm R.D., R. Nerem, K. J. H. Cells into Systems: A new research center will work with the basics of life to build complex biological machines. *Mech Eng Mag* **132,** 30–34 (2010).

87.   Pedersen, J. a & Swartz, M. a. Mechanobiology in the third dimension. *Ann Biomed Eng* **33,** 1469–90 (2005).

88.   Dhimolea, E., Maffini, M. V, Soto, A. M. & Sonnenschein, C. The role of collagen reorganization on mammary epithelial morphogenesis in a 3D culture model. *Biomaterials* **31,** 3622–30 (2010).

89.   Debnath, J., Muthuswamy, S. K. & Brugge, J. S. Morphogenesis and oncogenesis of MCF-10A mammary epithelial acini grown in three-dimensional basement membrane cultures. *Methods* **30,** 256–268 (2003).

90.   Paszek, M. J. *et al.* Tensional homeostasis and the malignant phenotype. *Cancer Cell* **8,** 241–54 (2005).

91.   Rao, S. S. *et al.* Inherent Interfacial Mechanical Gradients in 3D Hydrogels Influence Tumor Cell Behaviors. *PLoS One* **7,** e35852 (2012).

92.   Silberstein, G. B. Tumour-stromal interactions. Role of the stroma in mammary development. *Breast Cancer Res* **3,** 218–23 (2001).

93.   Lee, G. Y., Kenny, P. A., Lee, E. H. & Bissell, M. J. Three-dimensional culture models of normal and malignant breast epithelial cells. **4,** 359–365 (2007).

94.   Deserno, M. The shape of a straight fluid meniscus. (2004).

95.   Wozniak, M. a, Desai, R., Solski, P. a, Der, C. J. & Keely, P. J. ROCK-generated contractility regulates breast epithelial cell differentiation in response to the physical properties of a three-dimensional collagen matrix. *J Cell Biol* **163,** 583–95 (2003).

96.   Krause, S., Maffini, M. V, Soto, A. M. & Sonnenschein, C. The microenvironment determines the breast cancer cells' phenotype : organization of MCF7 cells in 3D cultures. (2010).

97.   Buxboim, A., Rajagopal, K., Brown, A. E. X. & Discher, D. E. How deeply cells feel: methods for thin gels. *J Phys Condens matter* **22,** 1–10 (2010).

98.   Rao, S. S. *et al.* Inherent Interfacial Mechanical Gradients in 3D Hydrogels Influence Tumor Cell Behaviors. *PLoS One* **7,** e35852 (2012).

99.   Guo, C. *et al.* Long-range mechanical force enables self-assembly of epithelial tubular patterns. (2012). doi:10.1073/pnas.1114781109/-/DCSupplemental.www.pnas.org/cgi/doi/10.1073/pnas.1114781109

100.   Lee, G. Y., Kenny, P. A., Lee, E. H. & Bissell, M. J. Three-dimensional culture models of normal and malignant breast epithelial cells. **4,** 359–365 (2007).

101.   Szeliski, R. Image Alignment and Stitching: A Tutorial. *Found Trends Comput Graph Vis* **2,** 1–104 (2006).

102.   Preibisch, S., Saalfeld, S. & Tomancak, P. Globally optimal stitching of tiled 3D microscopic image acquisitions. *Bioinformatics* **25,** 1463–5 (2009).

103. Hovden, R., Xin, H. L. & Muller, D. a. Extended depth of field for high-resolution scanning transmission electron microscopy. *Microsc Microanal* **17,** 75–80 (2011).

104. Toet, A. & Ruyven, V. Merging thermal and visual images by a contrast pyramid. **28,** 789–792 (1989).

105. Aguet, F., Member, S., Ville, D. Van De & Unser, M. Model-Based 2.5D Deconvolution for Extended Depth of Field in Brightfield Microscopy. *IEEE Trans image Process* **17,** 1144–1153 (2008).

106. Forster, B., Van De Ville, D., Berent, J., Sage, D. & Unser, M. Complex wavelets for extended depth-of-field: a new method for the fusion of multichannel microscopy images. *Microsc Res Tech* **65,** 33–42 (2004).

107. Zemelman, B. V, Lee, G. A., Ng, M. & Miesenbo, G. Selective Photostimulation of Genetically ChARGed Neurons. *Neuron* **33,** 15–22 (2002).

108. Deisseroth, K. *et al.* Next-Generation Optical Technologies for Illuminating Genetically Targeted Brain Circuits. *J Neurosci* **26,** 10380–10386 (2006).

109. Arrenberg, A. B., Stainier, D. Y. R., Baier, H. & Huisken, J. Optogenetic control of cardiac function. *Science* **330,** 971–4 (2010).

110. Stirman, J. N., Crane, M. M., Husson, S. J., Gottschalk, A. & Lu, H. A multispectral optical illumination system with precise spatiotemporal control for the manipulation of optogenetic reagents. *Nat Protoc* **7,** 207–20 (2012).

111. Chan, V. *et al.* Development of miniaturized walking biological machines. *Sci Rep* **2,** 857 (2012).

112. Neal, D., Sakar, M. S. & Asada, H. H. Optogenetic Control of Live Skeletal Muscles : Non-Invasive , Wireless , and Precise Activation of Muscle Tissues *. 1513–1518 (2013).

113. Schobert, B. & Lanyi, J. Halorhodopsin is a light-driven chloride pump. *Annu Rev Biophys Biophys Chem* **257,** 11–28 (1982).

114. The OpenCV Reference Manual. (2012).

115. Lucas, B. & Kanade, T. An interative Image Registration Technique with an Application to Stereo Vision. *Proc DARPA Image Underst* 674–679 (1981).

116. Bouguet, J. Pyramidal Implementation of the Lucas Kanade Feature Tracker Description of the algorithm. **1,** 1–9

Appendix
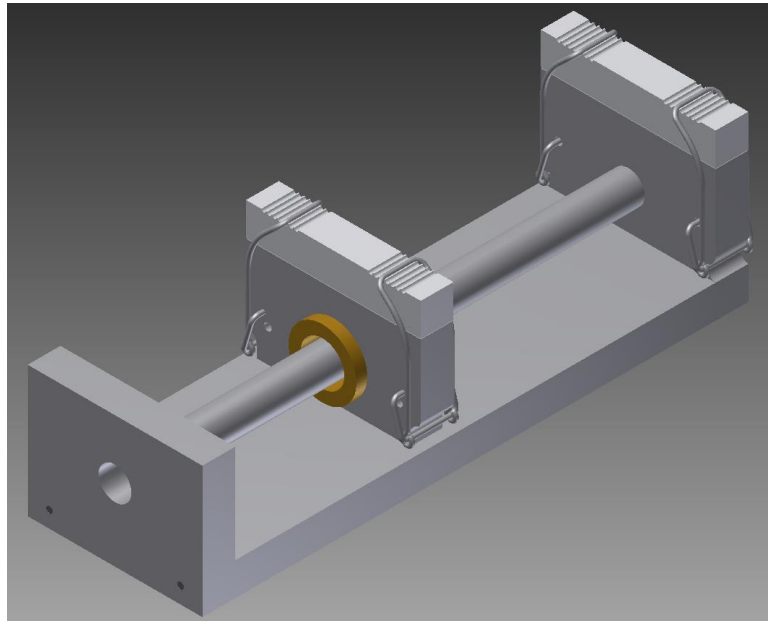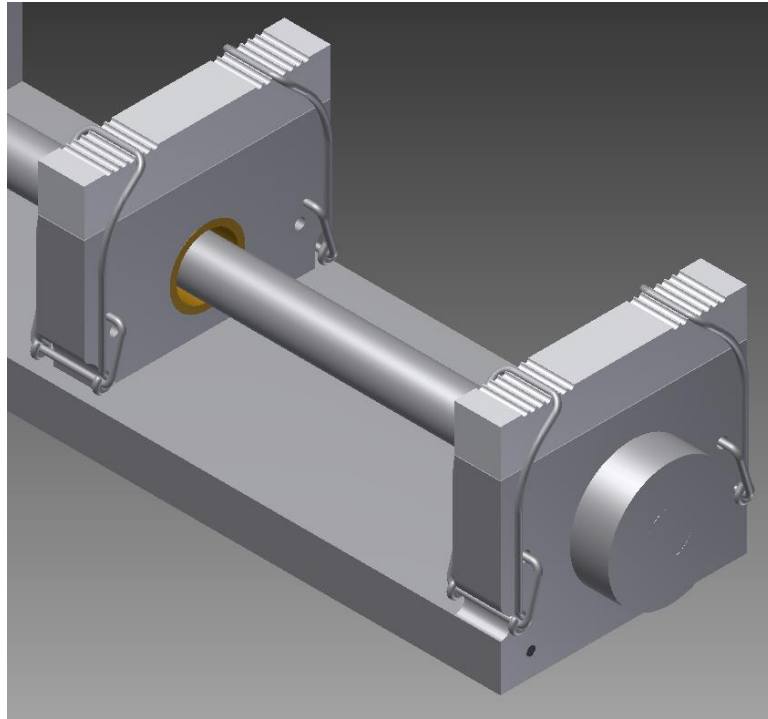
Figure A.1: CAD model of straining device

Figure A.2: Matlab script to extract wavelength and amplitude from AFM data

```matlab
close all
scrnSz = get(0,'ScreenSize');

saveType = '.png'; % or '.emf', or '.eps'

if ~exist('dirName', 'var')
    dirName = uigetdir;
end

dirFiles = dir(dirName);


for ii=1:length(dirFiles)
    %% Import data

    fName = [dirName,'\',dirFiles(ii).name];

    if ~exist(fName, 'file') || (strcmpi(fName(end-3:end), '.dat')~=1 &&
strcmpi(fName(end-3:end), '.txt')~=1)
        continue;
    end

    afmDat = importdata(fName);
    img    = afmDat.data;
    ptDim  = size(img,2);
    img    = 10^9*img(1:ptDim,:);

    %% Extract sample info

    sampInfo = strsplit(dirFiles(ii).name, {'_', '.'});
    if length(sampInfo) == 5;
        sampLbl = sampInfo{1};
        sampNo  = sampInfo{2};
        trueDim = sscanf(sampInfo{3}, '%d');
        scanNo  = sscanf(sampInfo{4}, '%d');
    else
        disp('Incorrect name, use format: <sample label>_<sample number>_<dimension in
um>u_<scan number>.txt');
        sampLbl = dirFiles(ii).name;
        sampNo  = '1';
        trueDim = 1000;
        scanNo  = 1;
    end


    %% Get approximate rotation angle

    ft  = abs(fft2(img));
    ft2 = ft(1:floor(ptDim/8),1:floor(ptDim/8));

    [~,ftMaxLoc] = max(ft2(:));
    [maxY,maxX]  = ind2sub([floor(ptDim/8),floor(ptDim/8)], ftMaxLoc);

    ft2 = padarray(ft2, [1 1], 'replicate');
    ft2NearMax = ft2(maxY:maxY+2, maxX:maxX+2).^2;
```

```matlab
wgtY = [-1 -1 -1; 0 0 0; 1 1 1]+maxY-1;
wgtX = [-1 0 1; -1 0 1; -1 0 1]+maxX-1;


maxY2 = sum(sum(wgtY.*ft2NearMax))/sum(ft2NearMax(:));
maxX2 = sum(sum(wgtX.*ft2NearMax))/sum(ft2NearMax(:));


turnAng = 180*atan(maxX2/maxY2)/pi;



%% Check if rotation is CW or CCW

temp    = abs(fft2(imrotate(img, turnAng, 'bilinear')));
rotMax  = max(temp(:,1));
temp    = abs(fft2(imrotate(img,-turnAng, 'bilinear')));
tempMax = max(temp(:,1));
if tempMax > rotMax
    turnAng = -turnAng;
    rotMax  = tempMax;
end



%% Get ideal rotation by rotating image slightly and finding fft peak

bestAngChange = 0;
for dAng = -1.7 : .2 : 1.7
    temp = abs(fft2(imrotate(img, turnAng+dAng, 'bilinear')));
    tempMax = max(temp(:,1));
    if tempMax > rotMax
        bestAngChange = dAng;
        rotMax = tempMax;
    end
end

turnAng = turnAng + bestAngChange;

for dAng = -.15 : .02 : .15
    temp = abs(fft2(imrotate(img, turnAng+dAng, 'bilinear')));
    tempMax = max(temp(:,1));
    if tempMax > rotMax
        bestAngChange = dAng;
        rotMax = tempMax;
    end
end

turnAng = turnAng + bestAngChange;



%% Crop off blank stuff introduced by the rotation

img     = imrotate(img, turnAng, 'bilinear');
newSize = floor(ptDim/(abs(cos(pi*turnAng/180))+abs(sin(pi*turnAng/180))));
offset  = round((length(img)-newSize)/2);
img     = img(offset+1:offset+newSize , offset+1:offset+newSize);



%% Remove outliers for measurement and side view
```

113

Figure A.2 (continued): Matlab script to extract wavelength and amplitude from AFM data

```matlab
outlierFt   = fft2(img);
    outlierFt([1:round(maxY2-3),round(maxY2+3):end-round(maxY2+3),end-round(maxY2-
3):end] , 4:end-3) = 0;
    outlierImg = ifft2(outlierFt, 'symmetric');
    outlierDif1 = img - outlierImg;
    outlierDif = abs(outlierDif1);

    img2 = img;
    img2(outlierDif > mean(outlierDif(:)) + 2*std(outlierDif(:))) = NaN;


    %% Analysis

    waveLength = trueDim/sqrt(maxX2^2+maxY2^2)*cos(pi*turnAng/180);
    meanAmp = pi*nanmean(abs(img2(:)));
    rmsAmp = 2^1.5*nanmean(img2(:).^2)^.5;
    waveAmp = (meanAmp+rmsAmp)/2;
    ampQual = 1-4*abs(meanAmp-rmsAmp)/waveAmp;
    surfPts = linspace( trueDim*(ptDim-newSize)/ptDim/2 ,
trueDim*(ptDim+newSize)/ptDim/2 , newSize);

    [xx, yy] = meshgrid(surfPts, surfPts);
    xxx = xx(~(outlierDif > mean(outlierDif(:)) + 2*std(outlierDif(:))));
    yyy = yy(~(outlierDif > mean(outlierDif(:)) + 2*std(outlierDif(:))));
    imz = img(~(outlierDif > mean(outlierDif(:)) + 2*std(outlierDif(:))));

    sin2d = fittype('a*sin(2*pi*x*b + 2*pi*y*c + d)',
'dependent',{'z'},'independent',{'x', 'y'}, 'coefficients',{'a', 'b', 'c', 'd'});
    [pFit, rsq] = fit( [xxx(:), yyy(:)], imz(:), sin2d, 'startpoint', [waveAmp/2, 0,
1/waveLength, 0] );

    sp2 = linspace(min(surfPts), max(surfPts), 768);
    [x2, y2] = meshgrid(sp2, sp2);


    %% Display and Save

    titleText = ['\lambda: ',num2str(1/sqrt(pFit.b^2 + pFit.c^2) , 3),'\mum
d: ',num2str(2*pFit.a, 3),'nm                    R^{2}: ',num2str(rsq.rsquare,
3)];

    close all;
    mdf = mean(outlierDif(:));
    sdf = 1.5*std(outlierDif(:));
    img(outlierDif > mdf + sdf) = img(outlierDif > mdf+sdf) -
.5*outlierDif1(outlierDif > mdf+sdf);
    hFig = figure('Position',scrnSz, 'Visible', 'off');
    surf(surfPts , surfPts, img ,'LineStyle','none', 'FaceLighting','phong');
    shading interp;
    view(110,65);
    colormap jet;
    xlims = get(gca, 'Xlim');
    ylims = get(gca, 'ylim');
    if floor(xlims(2)/5) - ceil(xlims(1)/5) > 3
        xstep = 10;
    else
        xstep = 5;
    end
```

Figure A.2 (continued): Matlab script to extract wavelength and amplitude from AFM data

```matlab
    set(gca, 'fontsize', 26);
    set(gca, 'Xtick', ceil(xlims(1)/xstep)*xstep:xstep:floor(xlims(2)/xstep)*xstep);
    set(gca, 'Ytick', ceil(xlims(1)/xstep)*xstep:xstep:floor(xlims(2)/xstep)*xstep);
    zavg = (max(img(:))-min(img(:)))/2;
    fltz = 10^(floor(log10(zavg)));
    set(gca, 'Ztick', [-fltz*floor(zavg/fltz), fltz*floor(zavg/fltz)]);
    set(gca, 'Zlim', [-1.85*max(max(img(:)),-min(img(:))) , 1.85*max(max(img(:)),-
min(img(:)))]);

    title( titleText , 'FontWeight' , 'bold' , 'FontSize' , 20 );
    saveas(hFig, [fName(1:end-4), '_a', saveType]);
    close;

    hFig = figure('Position',scrnSz, 'Visible', 'off');
    surf(surfPts , surfPts, img,'LineStyle','-', 'FaceLighting','phong');
    shading interp;
    view(90,0);

    title( titleText , 'FontWeight' , 'bold' , 'FontSize' , 20 );
    xlims = get(gca, 'Xlim');
    set(gca, 'fontsize', 26);
    set(gca, 'Xtick', ceil(xlims(1)/xstep)*xstep:xstep:floor(xlims(2)/xstep)*xstep);
    set(gca, 'Ytick', ceil(xlims(1)/xstep)*xstep:xstep:floor(xlims(2)/xstep)*xstep);
    set(gca, 'Ztick', [-fltz*floor(zavg/fltz), fltz*floor(zavg/fltz)]);
    set(gca, 'Zlim', [-1.1*max(max(img(:)),-min(img(:))) , 5*max(max(img(:)),-
min(img(:)))]);
    saveas(hFig, [fName(1:end-4), '_b', saveType]);
    close;

    imwrite( 10*(img-min(img(:)))/65535 , [fName(1:end-4),'.png'], 'png', 'BitDepth',
16);

end
```

Table A.1: Summary of plasma oxidation experiments. Wavelengths and amplitudes for various process conditions

Base Ratio	Strain (%)	Power (W)	Oxidation Time (min)	Wavelength (nm)	Depth (nm)
18	10	100	10	830	180
18	8	200	5	830	145
18	6	200	2	670	115
21	8	100	5	860	150
21	8	100	10	1720	150
21	5	100	10	1690	200
21	10	100	10	1980	200
8	10	100	4	480	60
8	10	100	3	420	20
8	10	100	3	420	12
8	10	100	3	410	24
8	10	100	4	550	65
20	10	100	7	1160	145
20	10	100	3	750	70
20	10	100	5	910	63
20	10	100	1	460	36
15	10	200	3	1150	80
15	10	200	7	1600	110
15	10	200	5	1450	90
15	10	200	9	2200	210
20	10	200	3	1150	120
8	10	200	5	750	55
8	10	200	7	1200	75
10	10	200	3	800	50
10	10	200	5	1150	90
10	10	200	7	1250	115
10	10	200	9	1600	135
10	10	200	7	1200	140
10	10	200	5	1070	30

Figure A.3: Matlab script to measure alignment and confluence of C2C12 cells on wavy patterns. Requires the matlabPyrTools library to be installed, available at http://www.cns.nyu.edu/~lcv/software.php.

```matlab
noLevels = 2; % 2 is best
noOrientations = 8; % I like 8  if ~mod(360, noOrientations) good else bad

if noOrientations == 4,
    filts = 'sp3Filters';
elseif noOrientations == 6,
    filts = 'sp5Filters';
else
    filts = [];
end

threshd=15;
c =.02;
m = ones(threshd,threshd);
n = threshd^2;
input_directory = uigetdir;
flist = getfiles2(input_directory, 999, {'.png', '.jpg', '.tif'}, 'AG4');


name_num = length(input_directory);
FOfid = fopen([input_directory '/RESULTS.txt'], 'w');
fid = fopen([input_directory '/DETAILS.txt'], 'w');


hhh=waitbar(0);
for ii=1:length(flist)
    waitbar(ii/length(flist),hhh);
    file_name=flist{ii};

    if strcmp(file_name, 'xxxxxx');
        fprintf(FOfid, '\r\n');
        fprintf(fid, '\r\n');
        continue
    end

    img = single(imread(flist{ii}));
    if length(size(img)) == 3   ,   img = rgb2gray(img);   end

%     img = imresize(img, .5);

    im2 = bpf(img,1.5,256);
    im2 = z2oim(im2);

    if ~isempty(filts)
        [pyr,pind] = buildSpyr(im2, noLevels, filts);
    else
        [pyr,pind] = buildSFpyr(im2, noLevels , noOrientations-1);
    end

    % Get the histogram
    h = zeros( spyrNumBands(pind) , min(4,spyrHt(pind)));

    % For each band, look at all scales
    for b = 1:spyrNumBands(pind)
        for s = 1:min(4,spyrHt(pind))
            band = spyrBand(pyr,pind,s,b);
            h(b,s) = norm(band(:));
```

117

Figure A.3 (continued): Matlab script to measure alignment and confluence of C2C12 cells on wavy patterns. Requires the matlabPyrTools library to be installed, available at http://www.cns.nyu.edu/~lcv/software.php.

```matlab
        end
    end


    % Sum the energy in all scales
    % We can also use maximum or something similar
    htotal = sum( h, 2); % energy in each diretion (#_directions x 1 array)
    hs_sum = htotal./sum(htotal); %normalize htotal so total energy in all directions
is 1
    max_ratio = max(hs_sum(:)) / min(hs_sum(:)); % scalar ratio of energy between
highest and lowest directions, arbitrary units, usually ~4 is perfect alignment for
C2C12 images

    fprintf(fid, '%s\t', file_name(name_num+2:end-4));
    for jj=1:noOrientations,
        fprintf(fid, '%5.3f\t',hs_sum(jj)); % include the normalized individual
directions, might want to check on them later
    end
    fprintf(fid, '\r\n');


    img = conv2(im2, m, 'same');
    im2 = im2bw(im2 - 1.2*img/n - c, 0);
    im2 = imclose(im2,strel('disk',7));
    im2 = imopen(im2,strel('disk',2));
    im2 = imdilate(im2,strel('disk',2));
    im2 = imclose(im2,strel('disk',5));

    fprintf(FOfid, '%s\t%5.3f\t%5.3f\r\n', file_name(name_num+2:end-4),
min(1.02*sum(im2(:))/numel(im2),1), max_ratio); % print results to file, first two
columns are name and 'alignment value'
end

close(hhh);

fclose(FOfid);
fclose(fid);
```

Figure A.4: Images of C2C12 cells from time lapse experiment on pitch = 1.67µm, depth = 410nm pattern. Images are evenly spaced over 42 hours.

200 µm

φ = 6.8E-4
γ = .04
ρ = .32

φ = 6.8E-4
γ = .00
ρ = .99

φ = 1.8E-3
γ = .07
ρ = .31

φ = 1.8E-3
γ = .64
ρ = .98

φ = 2.2E-3
γ = .10
ρ = .13

φ = 2.2E-3
γ = .89
ρ = .99

φ = 3.9E-3
γ = .45
ρ = .14

φ = 3.9E-3
γ = .87
ρ = .93

φ = 1.2E-2
γ = .99
ρ = .28

φ = 1.2E-2
γ = .95
ρ = .99
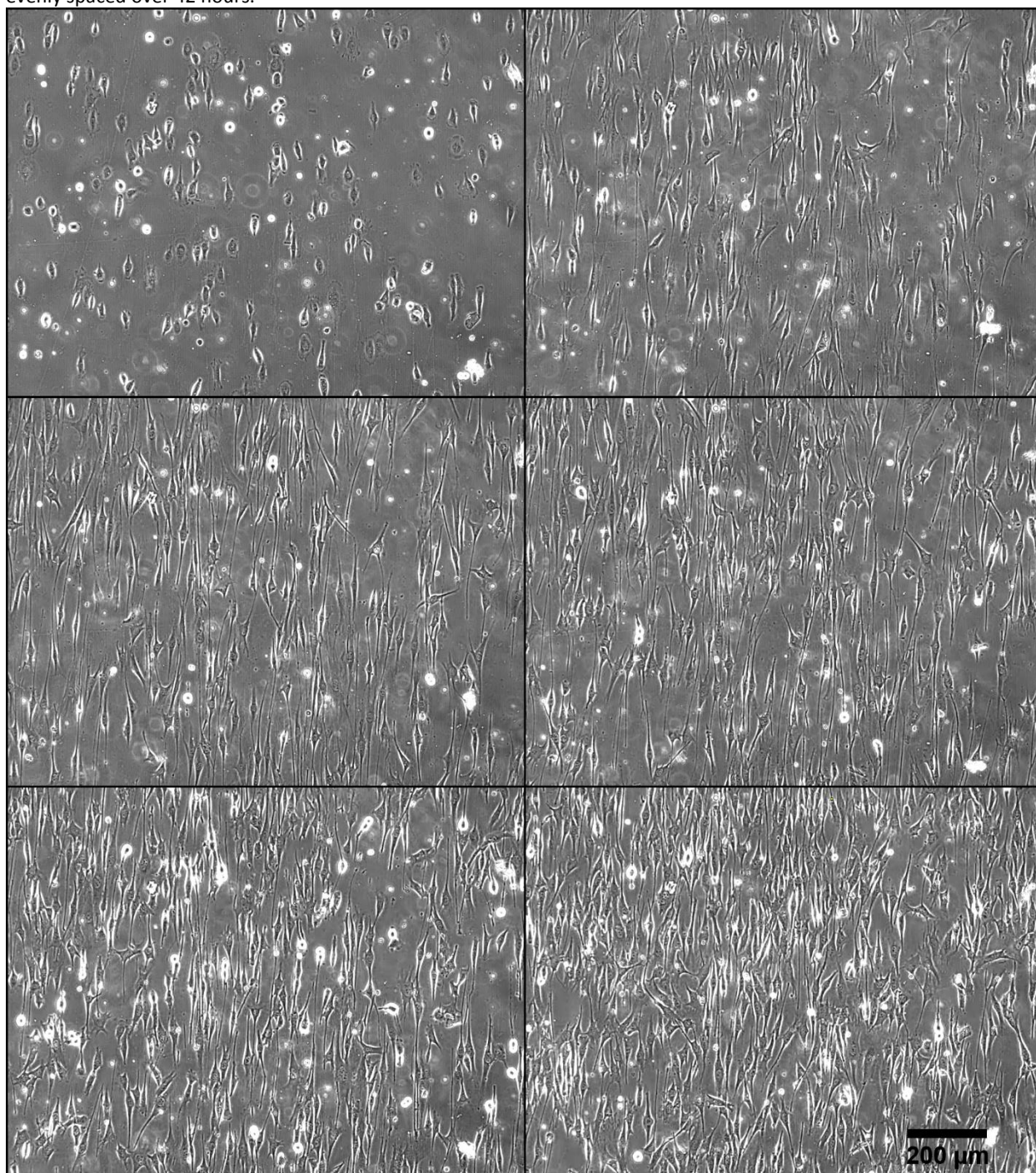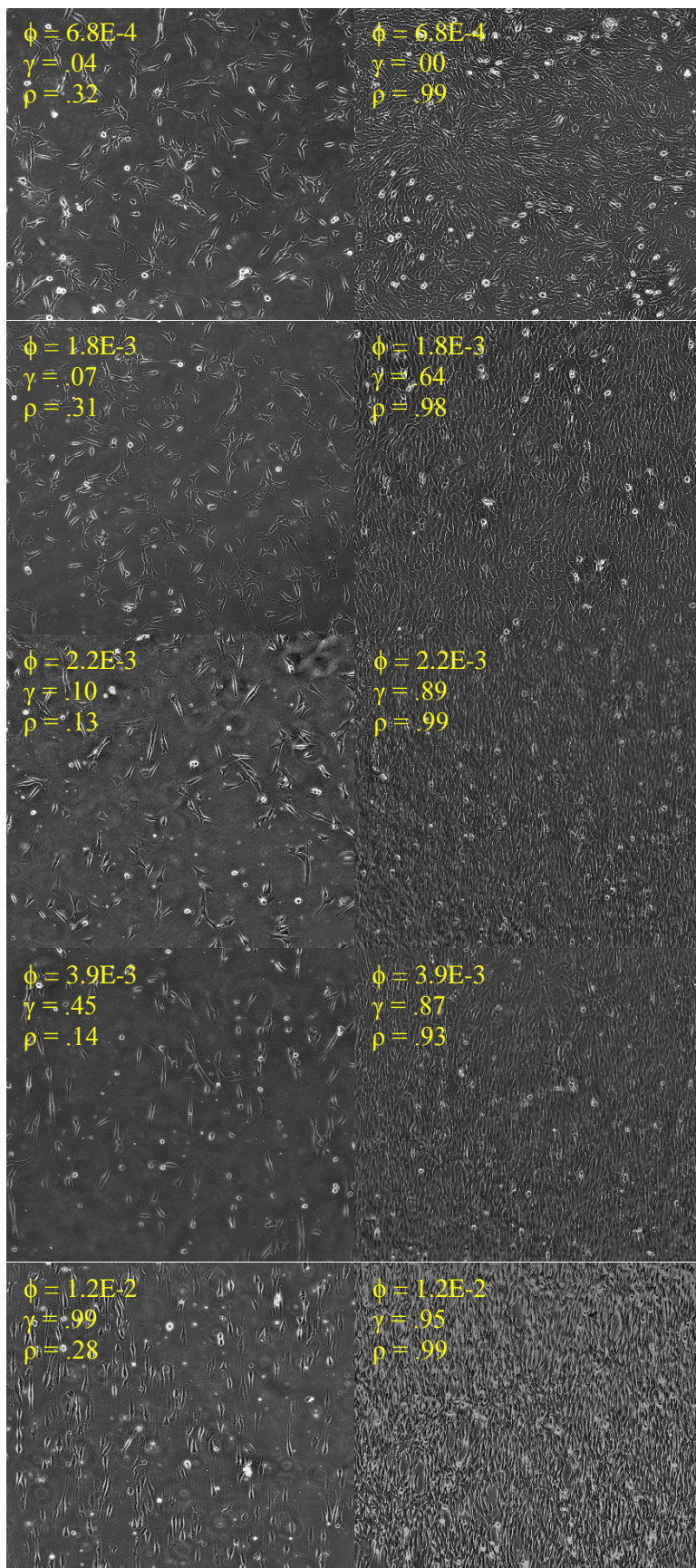
Figure A.5: Additional examples of alignment and confluence metrics

Red = +5V Logic Power
Black = GND Logic
Green = Stepper Ctrl Connections
Blue = Internal Connecitons (Solder)
Pink = +12-30V Motor Power
Gray = GND Motor
White = Stepper Microstep Ctrl
Brown = Misc.

On the actual perf board, wire colors
are white for input/logic, red for
+power (Vdd+ and Vm+) and black
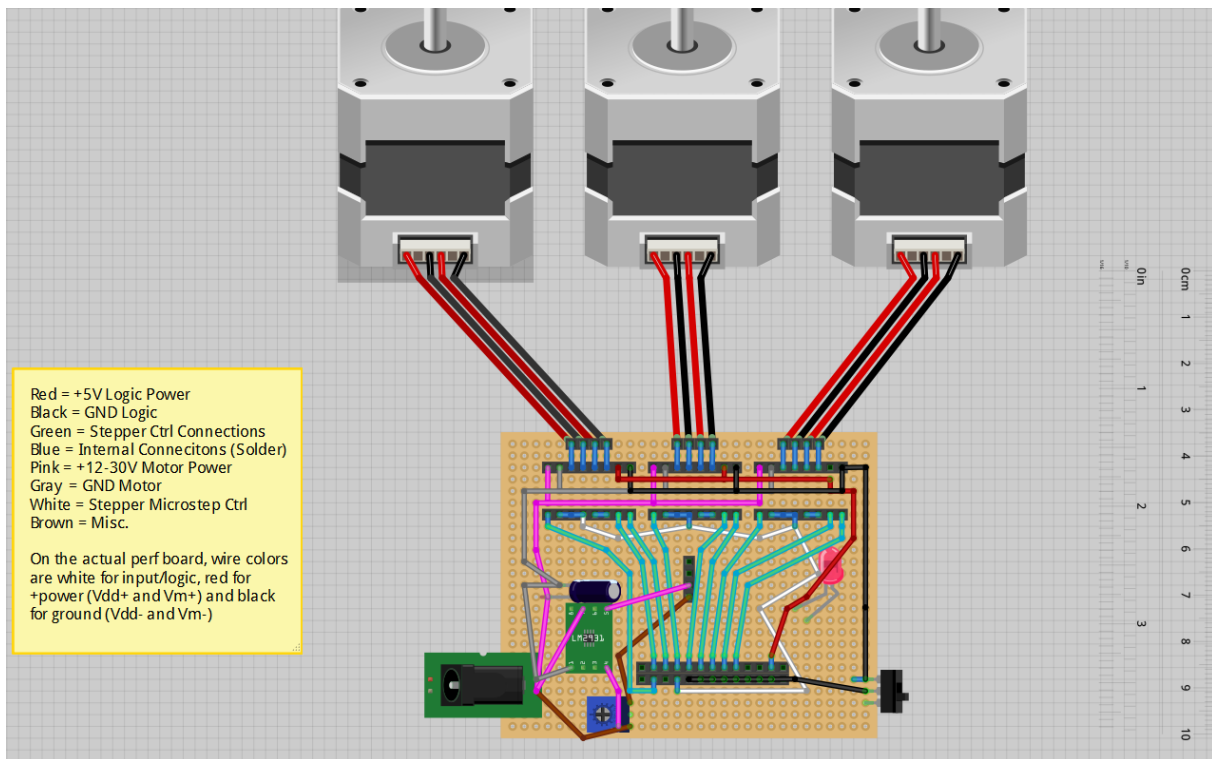for ground (Vdd- and Vm-)

Figure A.6: Wire diagram for automatic stage motor controller

Figure A.7: Optogenetics software usage instructions

Hot Keys - **Select the Camera window and press any of these buttons**

Type	Key	Description
Press Once	C	Clear: Gets rid of all the illuminated spots
Press Once	Esc	Exit: Exits the program
Press Once	P	Calibrate: Starts the auto-calibrations sequence
Toggle	W	Point and Click: Toggles between clicking a spot to illuminate a predefined shape once and selecting a shape of arbitrary size to illuminate
Toggle	T	Tracking: Toggles between tracking and stationary illumination, illuminated areas will either move to follow their selection or stay at the selected location
Toggle	S	Saving: Toggles between saving selections for repeated illumination (blinking) or just illuminating the selection once
Toggle	B	Black When Off: switches between projecting black regions between illuminations while blinking and not. Effective when background is not black.
Toggle	R	Projection Plane/Rotation: switches between projecting spots to the plane imaged by the camera, or the plane/rotation the projector naturally projects to
Toggle	V	Video: Press once to start video and again to stop video. Records each frame of the Camera window at the frame rate being displayed (see X)
Toggle	F	Frequency: Now: prints the refresh rate of the projector window. Later: the actual measured frequency of repeated illumination averaged over a few cycles
Toggle	X	Time: prints the time between successive frames displayed. For testing how fast/slow the program is running (usually depends on camera exposure time)
Toggle	D	Debug: toggles printing information about calculations (like projection plane calculation)
Increment/ Decrement	- +	Size: increase/decrease size of predefined shape
Increment/ Decrement	[ ]	Color: Cycle through the predefined illumination colors
Increment/ Decrement	< >	Shape: Cycle through the predefined illumination shapes

Controls/Sliders - *Slide these bars on the* Controls *window to change values*

Label	Description
Duty Cycle	The percentage of time illuminated spots will be on (when they are blinking)
Frequency	The frequency at which the illuminated spots blink, in Hertz/100
Phase	As a percentage of one period… the time delay between the illumination of successive spots
# of Dots	Maximum number of tracked spots - Ex: set to less than total spots temporarily turn off some spots or overwrite earlier spots
Back Int	Brightness of the background projected by the projector, 0 is black/no background. (the projector will show the background where there are no spots)
Back Hue	Color/hue of the background projected by the projector, 0 is black/no background. (the projector will show the background where there are no spots)
Cal Bright	Initial brightness (0-255) of calibration dots. Adapts during calibration (for calibrating, i.e. determining the camera plane -> projector plane matrix transformation)
Cal Size	Initial size of calibration dots. Size adapts during calibration (for calibrating, i.e. determining the camera plane -> projector plane matrix transformation)
Proj Color	Cycle through the predefined illumination colors Same as < [> and <] > hotkeys
Proj Rad	increase/decrease size of predefined shape Same as < - > and < + > hotkeys
Proj Shape	Cycle through the predefined illumination shapes Same as < , > and < . > hotkeys
Colors at the bottom	If it fits on the screen… lets you select the "Proj Color". Also shows the color order for "Proj Color"

Usage - *How to operate the system (roughly chronological order)*

Run *Optogenetics.exe*	There should be a shortcut to the executable on the desktop. If not, you can run the program directly by finding: ?\Optogenetics\Release\Optogenetics.exe
Setup Hardware	Connect the projector and the camera to the computer and turn the projector on… Make sure the camera has the proper field of view and focus by placing your specimen or equivalent on the stage. Adjust the height of the camera above the stage to change the field of view, then adjust the focus on the camera with the plastic cog in its midsection. Set your focus before calibrating.
Calibrate Projector **Start with "P"**	If the program has been run before, the previous calibration is automatically loaded. To make a new calibration the projector will project random points on the projector and try to find them with the camera. You will need to place a piece of computer paper on the stage where the specimen will go so there is a surface on which the projector can form an image. Press "P" and the program will attempt to threshold/binarize the camera's view of the dots. You'll see the result in the *Camera* window while it's working. If successful, you should see the transform matrix printed in the command window when it's done. Once successfully calibrated, remove the computer paper and replace with your specimen.
Debugging Auto-Calibration	The calibration is not particularly robust, so you might not be successful on the first attempt (regions won't project where they should). No problem, change the calibration options and repeat the previous step. On the *Controls* window (see *Slider Bars* chart) you can adjust the options. Here's how to go about making it work: If dots stop blinking on screen or you get "RNG failed": lower *Cal Rad* (try 5) If dots are circled with the wrong color: lower *Cal Bright* (try 70) If dots aren't detected at all: increase *Cal Bright* or *Cal Rad* Test the calibration: try selecting a shape on *Camera*, it should be exactly illuminated on the screen
Point and Click Mode **Toggle with "W"**	When ON, the outline of a shape is visible in the *Camera* window, and it will follow your mouse when it's over the window. Click, and the projector projects the filled shape until you release. Use the *Controls* to adjust shape/size/color of the shape. When OFF, click and drag to make a selection, then release to have it illuminate. Click anywhere again to clear the selection. The Point and Click behavior continues while other spots are blinking or being tracked.

Figure A.7 (continued): Optogenetics software usage instructions

Save Move **Toggle with "S"**	When Save mode is ON, regions you illuminate are 'saved' and will remain illuminated/blinking until cleared. On mouse-up after a selection, the selected area should start blinking. Depending on the Tracking setting, the region will either stay in place or start moving about. If you toggle Save mode OFF the selected regions remain, and you can continue illuminating on click/selection independently of the saved regions (which continue to blink). Press "C" to clear all the selected regions. *Hotkeys require one of the windows to be active*
Tracking Mode **Toggle with "T"**	When Tracking mode is OFF, selected regions endlessly blink at their current location. When tracking mode is turned ON, current and new selected regions will be 'tracked' – this means a bunch of key points will be identified within the region, and the program tries to follow them from one frame to the next. Keep in mind it is contrast/edge-based (and ignores color), so the target area should ideally have some distinct contrast/texture.
Using The Repetition and Timing Controls	By default, every selected region will blink with the same, constant frequency, measured in Hertz/100 (i.e. frequency = 100 means 1.00 Hz). Use the slider bar on the *Controls* window to adjust the frequency – it should snap to reasonable values. Changing the frequency will affect existing regions. To see the exact frequency the system is actually outputting, press "F", and the average frequency is periodically printed in the command window. The phase is the percentage of a full cycle (slider needs integer…) delay between successive regions being illuminated. Setting this to 0 will sync up all the regions. Every time a new region is added, the cycle restarts with the first region to ensure proper timing. Duty cycle is the percentage of time the dot is illuminated. To get constant illumination, set *Duty Cycle* to 100. At the moment, regions will actually project the same shape in black when they are blinking and 'off', which could cause some confusion if regions overlap – the order of selection might change behavior. A toggle will be available soon.
Recording Video **Start/stop: "V"**	Pressing "V" will start recording the contents of the *Camera* window exactly as it appears on the computer. The file should have some name like <date>_<time>.avi The file is saved in the same folder as the executable (and "config.dat"), which is something like ?\Optogenetics\Release\ If you're using a shortcut, right-click the shortcut and select "Open File Location"
Saving/Loading Settings	When you exit the program, all your settings should be saved in a file called "config.dat". If available, the settings are loaded when the program starts. The "config.dat" file will be created and loaded from the same folder as the executable, so you can load/transfer a saved configuration by putting "config.dat" in this folder. See *Recording Video* for finding the folder.
Exiting / Freezing	The preferred way to exit the program is to select any window and press Esc. If the program freezes, it's usually best to just use End Task and restart. It won't hurt anything.